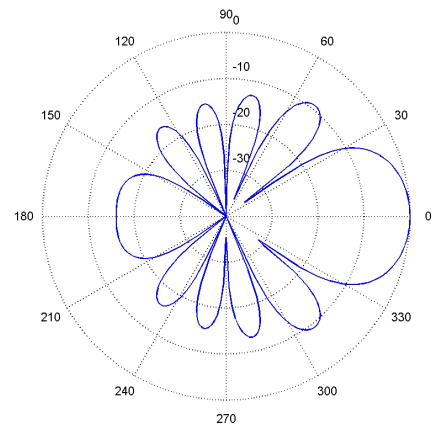
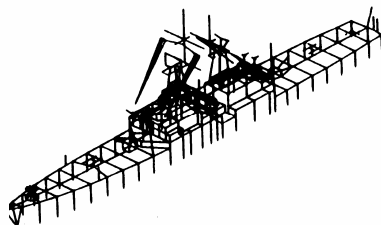
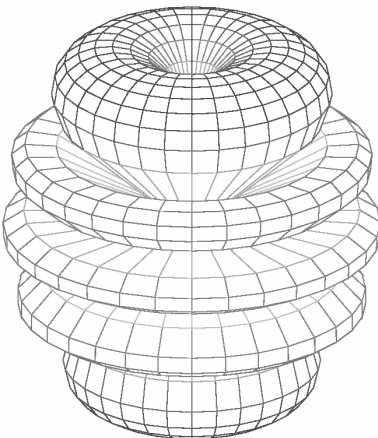
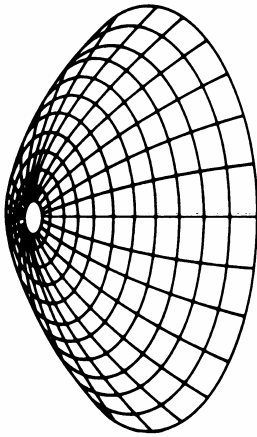
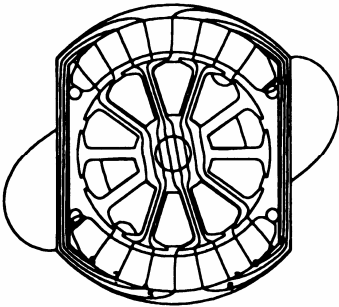
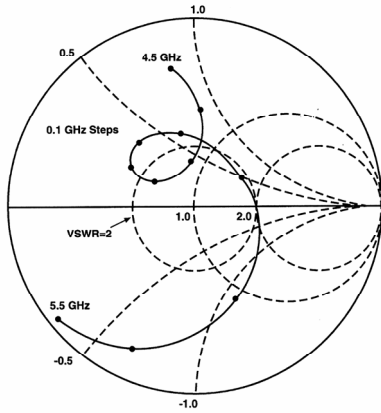


Applied Computational Electromagnetics Society Journal

Editor-in-Chief
Atef Z. Elsherbeni

July 2006
Vol. 21 No. 2
ISSN 1054-4887



GENERAL PURPOSE AND SCOPE: The Applied Computational Electromagnetics Society (*ACES*) Journal hereinafter known as the *ACES Journal* is devoted to the exchange of information in computational electromagnetics, to the advancement of the state-of-the art, and the promotion of related technical activities. A primary objective of the information exchange is the elimination of the need to “re-invent the wheel” to solve a previously-solved computational problem in electrical engineering, physics, or related fields of study. The technical activities promoted by this publication include code validation, performance analysis, and input/output standardization; code or technique optimization and error minimization; innovations in solution technique or in data input/output; identification of new applications for electromagnetics modeling codes and techniques; integration of computational electromagnetics techniques with new computer architectures; and correlation of computational parameters with physical mechanisms.

SUBMISSIONS: The *ACES Journal* welcomes original, previously unpublished papers, relating to applied computational electromagnetics. Typical papers will represent the computational electromagnetics aspects of research in electrical engineering, physics, or related disciplines. However, papers which represent research in applied computational electromagnetics itself are equally acceptable.

Manuscripts are to be submitted through the upload system of *ACES* web site <http://aces.ee.olemiss.edu> See “Information for Authors” on inside of back cover and at *ACES* web site. For additional information contact the Editor-in-Chief:

Dr. Atef Elsherbeni

Department of Electrical Engineering
The University of Mississippi
University, MS 386377 USA
Phone: 662-915-5382 Fax: 662-915-7231
Email: atef@olemiss.edu

SUBSCRIPTIONS: All members of the Applied Computational Electromagnetics Society who have paid their subscription fees are entitled to receive the *ACES Journal* with a minimum of three issues per calendar year and are entitled to download any published journal article available at <http://aces.ee.olemiss.edu>.

Back issues, when available, are \$15 each. Subscriptions to *ACES* are through the web site. Orders for back issues of the *ACES Journal* and changes of addresses should be sent directly to *ACES* Executive Officer:

Dr. Richard W. Adler

ECE Department, Code ECAB
Naval Postgraduate School
833 Dyer Road, Room 437
Monterey, CA 93943-5121 USA
Fax: 831-649-0300
Email: rwa@att.biz

Allow four week’s advance notice for change of address. Claims for missing issues will not be honored because of insufficient notice or address change or loss in mail unless the Executive Officer is notified within 60 days for USA and Canadian subscribers or 90 days for subscribers in other countries, from the last day of the month of publication. For information regarding reprints of individual papers or other materials, see “Information for Authors”.

LIABILITY. Neither *ACES*, nor the *ACES Journal* editors, are responsible for any consequence of misinformation or claims, express or implied, in any published material in an *ACES Journal* issue. This also applies to advertising, for which only camera-ready copies are accepted. Authors are responsible for information contained in their papers. If any material submitted for publication includes material that has already been published elsewhere, it is the author’s responsibility to obtain written permission to reproduce such material.

APPLIED COMPUTATIONAL ELECTROMAGNETICS SOCIETY JOURNAL

Editor-in-Chief
Atef Z. Elsherbeni

July 2006
Vol. 21 No. 2

ISSN 1054-4887

The ACES Journal is abstracted in INSPEC, in Engineering Index, and in DTIC.

The first, fourth, and sixth illustrations on the front cover have been obtained from the Department of Electrical Engineering at the University of Mississippi.

The third and fifth illustrations on the front cover have been obtained from Lawrence Livermore National Laboratory.

The second illustration on the front cover has been obtained from FLUX2D software, CEDRAT S.S. France, MAGSOFT Corporation, New York.

THE APPLIED COMPUTATIONAL ELECTROMAGNETICS SOCIETY

<http://aces.ee.olemiss.edu>

ACES JOURNAL EDITORS

EDITOR-IN-CHIEF/ACES/JOURNAL

Atef Elsherbeni

University of Mississippi, EE Dept.
University, MS 38677, USA

EDITORIAL ASSISTANT

Matthew J. Inman

University of Mississippi, EE Dept.
University, MS 38677, USA

EDITOR-IN-CHIEF, EMERITUS

David E. Stein

USAF Scientific Advisory Board
Washington, DC 20330, USA

ASSOCIATE EDITOR-IN-CHIEF

Alexander Yakovlev

University of Mississippi, EE Dept.
University, MS 38677, USA

EDITOR-IN-CHIEF, EMERITUS

Ducan C. Baker

EE Dept. U. of Pretoria
0002 Pretoria, South Africa

EDITOR-IN-CHIEF, EMERITUS

Allen Glisson

University of Mississippi, EE Dept.
University, MS 38677, USA

MANAGING EDITOR

Richard W. Adler

833 Dyer Rd, Rm 437 EC/AB
NPS, Monterey, CA 93943-5121, USA

EDITOR-IN-CHIEF, EMERITUS

Robert M. Bevensee

Box 812
Alamo, CA 94507-0516, USA

EDITOR-IN-CHIEF, EMERITUS

Ahmed Kishk

University of Mississippi, EE Dept.
University, MS 38677, USA

ACES JOURNAL ASSOCIATE EDITORS

Giandomenico Amendola

Universita' della Calabria
Rende , Italy

John Beggs

NASA Langley Research Center
Hampton, VA, USA

Malcolm Bibby

Gullwings
Weston, MA , US

John Brauer

Ansoft Corporation
Milwaukee, WI, USA

Magda El-Shenawee

University of Arkansas
Fayetteville AR, USA

Pat Foster

Microwave & Antenna Systems
Gt. Malvern, Worc. UK

Cynthia M. Furse

Utah State University
Logan UT, USA

Christian Hafner

Swiss Federal Inst. of Technology
Zurich, Switzerland

Michael Hamid

University of South Alabama,
Mobile, AL, USA

Andy Harrison

Radiance Technologies, Inc.
Huntsville, AL

Chun-Wen Paul Huang

Anadigics, Inc.
Warren, NJ, USA

Todd H. Hubing

University of Missouri-Rolla
Rolla, MO, USA

Nathan Ida

The University of Akron
Akron, OH, USA

Yasushi Kanai

Niigata Institute of Technology
Kashiwazaki, Japan

Leo C. Kempel

Michigan State University
East Lansing MI, USA

Andrzej Krawczyk

Institute of Electrical Engineering
Warszawa, Poland

Stanley Kubina

Concordia University
Montreal, Quebec, Canada

Samir F. Mahmoud

Kuwait University
Safat, Kuwait

Ronald Marhefka

Ohio State University
Columbus, OH, USA

Edmund K. Miller

LASL
Santa Fe, NM, USA

Krishna Naishadham

Wright State University
Dayton, OH, USA

Giuseppe Pelosi

University of Florence
Florence, Italy

Vicente Rodriguez

ETS-Lindgren
Cedar Park, TX, USA

Harold A. Sabbagh

Sabbagh Associates
Bloomington, IN, USA

John B. Schneider

Washington State University
Pullman, WA, USA

Amr M. Sharawee

American University
Cairo, Egypt

Norio Takahashi

Okayama University
Tsushima, Japan

THE APPLIED COMPUTATIONAL ELECTROMAGNETICS SOCIETY
JOURNAL

Vol. 21 No. 2

July 2006

TABLE OF CONTENTS

"The Spherical Harmonic Interface Procedure for MM and UTD Codes" J. Rockway, E. Newman and R. Marhefka.....	105
"Mutual Coupling between Monopoles on F-4 Aircraft at Transition Frequencies: A Comparison between MoM and MoM/UTD Hybrid Method at UHF Band" A. Dagdeviren, O. Cerezci, F. Ustuner, and B. Turetken.....	111
"A New Iterative Method to Compute the Higher Order Contributions to the Scattered Field by Complex Structures" F. Saez de Adana, O. Gutiérrez, L. Lozano, and M. Cátedra.....	115
"The Use of Multiquadric Radial Basis Functions in Open Region Problems" R. Gordon and W. Hutchcraft.....	127
"A Novel Dual-band Small Size Microstrip Antenna" A. Sheta, H. Boghdady, A. Mohra, and S. Mahmoud.....	135
"An Efficient Broadband Analysis of an Antenna via 3D FEM and Pade Approximation in the Frequency Domain" B. Essakhi and L. Pichon.....	143
"EBG Design using FSS Elements in Rectangular Waveguide" R. Kshetrimayum and L. Zhu.....	149
"Electromagnetic Modeling and Design of Dual-Band Septum Polarizers" A. Kirilenko, D. Kulik, L. Rud, V. Tkachenko, and N. Herscovici.....	155
"The Influence of Data Density on the Consistency of Performance of the Feature Selective Validation (FSV) Technique" A. Duffy and A. Orlandi.....	164
"To-Average or Not-to-Average in FDTD Modeling of Dielectric Interfaces" C. Furse, C. Waterman, and L. Griffiths.....	173

The Spherical Harmonic Interface Procedure for MM and UTD Codes

J. T. Rockway, E. H. Newman and R. J. Marhefka
 The Ohio State University
 ElectroScience Laboratory
 1320 Kinnear Road
 Columbus, OH 43212-1191

Abstract – This paper describes the use of a spherical harmonic expansion as an efficient interface between a low frequency method of moments (MM) code and a high frequency uniform geometrical theory of diffraction (UTD) code. It is shown that the method can save significant CPU time in the UTD code provided that the number of MM current filaments per cubic wavelength is large.

I. INTRODUCTION

In computational electromagnetics, when a problem involves both an electrically small part and an electrically large part, the standard approach is a hybrid solution [7, 12, 5, 11]. For example, consider the problem of an antenna radiating in the presence of an electrically large structure such as a ship or a building at X band. Typically, a low frequency method of moments (MM) code is used to find the currents on the antenna in free space, or in the presence of a small part of the structure closest to the antenna. These antenna currents are then input to a high frequency uniform geometrical theory of diffraction (UTD) code which determines their fields in the presence of the electrically large support structure.

The purpose of this paper is to describe the spherical harmonic interface procedure (SHIP) [9] in which a spherical harmonic expansion [10] of the free space antenna fields is used as an interface to the UTD code, rather than the MM antenna currents. The primary advantage of the SHIP is a result of the fact that in UTD ray tracing codes, the CPU time is proportional to the number of ray origins from which rays must be traced. Since for a complex antenna or large array, there could be thousands of MM currents, the UTD code would have to trace rays from thousands of origins. By contrast, a spherical harmonic expansion of the antenna fields has a single origin, and thus the UTD code need only trace rays from a single point. The CPU time for the SHIP is proportional to the number of spherical harmonics needed to accurately represent the antenna

fields, which in turn is proportional to the electrical size of the antenna.

A secondary advantage of the SHIP is that the UTD code can be written independent of the details of the low frequency code. The low frequency code can be based upon the MM, FEM, FDTD, etc., and can employ any basis functions. Providing that the UTD code is given the coefficients in the spherical harmonic expansion of the antenna fields, these details are not relevant to the UTD code.

Section II will begin with a description of the basic single origin or cell SHIP. It is then pointed out that there are two instances when it is either necessary or desirable to employ a multiple origin or multiple cell SHIP. First, the use of the spherical harmonic expansion requires the SHIP cells to be in the far zone of points of diffraction on the scattering structure. If an electrically large SHIP cell is in the near zone of the scatterer, then it must be split into smaller cells so that the points of diffraction on the scattering body are in the far zone of each cell. Second, it will be shown that it is possible to reduce the CPU time of the UTD code by employing a multiple cell SHIP. The paper will conclude with examples illustrating the reduced CPU time for the SHIP versus the standard MM current approach. For all examples, the MM code will be *The Electromagnetic Surface Patch Code: Version V* (ESP5) [8], and the UTD code will be the *NEC Basic Scattering Code* (NEC-BSC) [6]. All UTD code CPU times will be for a far zone pattern at 360 angles. All CPU times are for a PC with a 1.7 GHz Intel(T) Pentium M processor.

II. DESCRIPTION OF THE SHIP

II. A. Single Cell SHIP

A hybrid MM/UTD solution for an antenna radiating in the presence of a large structure begins with the MM code determining the current on the antenna,

and then the UTD code finds the fields produced by these currents in the presence of the large structure. Rather than have the UTD code trace rays from each MM current segment or current filament, one can construct a spherical wave expansion of the fields of the free space fields of the MM currents. In the far zone of a sphere of radius r_1 enclosing the currents, the spherical wave expansion for each component of the electric field is of the form

$$E(r, \theta, \varphi) = A \sum_{m=0}^{N_{\max 1}} \sum_{n=m}^{N_{\max 1}} [a_{mn} Y_{mn}^e + b_{mn} Y_{mn}^o] \frac{e^{-jkr}}{r}. \quad (1)$$

For simplicity we have assumed the enclosing sphere is centered at the coordinate origin, the subscript 1 emphasizes that this is for a single origin expansion, and the reader is referred to [1] for a detailed description of the various terms. To obtain reasonable accuracy from equation (1), the number of terms which must be kept in the summations is approximately [2-4]

$$N_{\max 1} = kr_1 + 3 \ln(kr_1 + \pi). \quad (2)$$

In the SHIP, the MM code provides the UTD code with the a_{mn} and b_{mn} coefficients of equation (1), and thus the UTD code need only trace rays from a single coordinate origin. It is also completely divorced from the details of the MM (or other) solution. The CPU time of the UTD code will be dependent upon the number of harmonics which must be summed in equation(1),

$$N_{H1} = N_{\max 1}^2 \approx (kr_1)^2 \quad \text{if } kr_1 \gg 1. \quad (3)$$

For the NEC-BSC code, Figure 1 shows a log-log plot of the CPU time versus N_{H1} for the scattering body being free space (i.e., no scatterer) and for the wedge of Figure 2. Free space and the wedge represent extremes in terms of the complexity of the ray trace. Noting that for large N_{H1} , these two extremes produce straight lines with essentially the same slope, the single cell CPU time must be of the form

$$T_1 = CN_{H1}^\beta = C(kr_1)^{2\beta} \quad (4)$$

where from the slope of the lines $\beta \approx 1.45$. C is a constant dependent upon the complexity of the ray trace, and a reasonable fit to the data of Figure 1 is

$$C_{FSp} \approx 6.82 \mu\text{sec}, \quad C_{Wedge} \approx 85.5 \mu\text{sec}. \quad (5)$$

Note that one should always choose the coordinate origin for the spherical wave expansion near the center of the MM currents, since this will minimize r_1 and thus the number of required harmonics, N_{H1} .

II. B. Multiple Cell SHIP

By a P cell SHIP it is meant that the single cell of radius r_1 is segmented into P smaller cells, and the

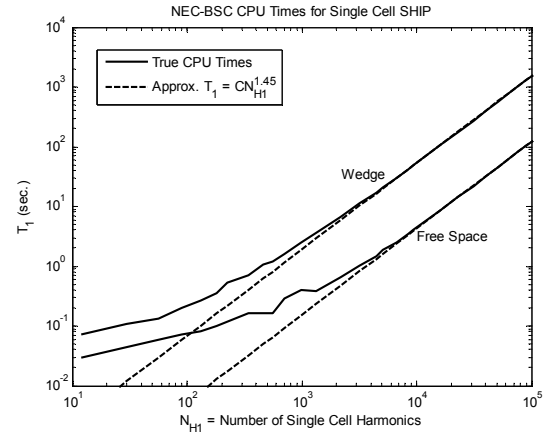


Fig. 1. CPU times for the single cell SHIP in free space and for the wedge.

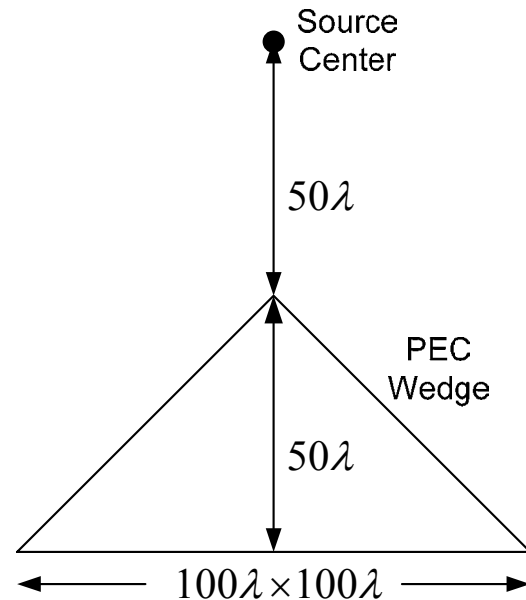


Fig. 2. Geometry for a PEC square base wedge.

total fields are expressed as the sum of the spherical wave expansions for the fields of the currents located in each of the P cells. If the single cell of radius r_1 is not in the far zone of a point of diffraction on the scatterer, then it must be segmented into smaller cells which are in the far zone. The cells may be in the near zone of a point of reflection since the NEC-BSC (and we assume most UTD codes) treat this via image theory. The P cell SHIP tends to increase the CPU time since the UTD code must trace rays from P origins, however, each ray trace is faster since the cells are smaller and thus require fewer harmonics. As shown below, it is possible to

reduce the overall UTD code CPU time by employing a multiple cell SHIP.

Referring to Figure 3, for simplicity we will assume that the radiating body can be classified, based upon its overall dimensions, as one of the following:

- 1D Body: 1 large and 2 small dimensions (linear array),
- 2D Body: 2 large and 1 small dimensions (square array),
- 3D Body: 3 large dimensions (cubic array).

In this case, the cell radius for P cells is simply related to that for the single cell by

$$r_p = \frac{r_1}{P^\alpha} \quad (6)$$

where $\alpha_{1D} = 1$, $\alpha_{2D} = 1/2$, and $\alpha_{3D} = 1/3$ for the three cases.

-The number of harmonics in each of the P cells is

$$N_{HP} = N_{\max P}^2 = (kr_p)^2 = \left(k \frac{r_1}{P^\alpha}\right)^2 = \frac{N_{H1}}{P^{2\alpha}}. \quad (7)$$

Since the UTD code must trace rays from each of the P origins, the total CPU time for the P cell SHIP is

$$T_p = P[CN_{HP}^\beta] = PC \left(\frac{N_{H1}}{P^{2\alpha}}\right)^\beta = P^{1-2\alpha\beta} T_1 = F_p T_1 \quad (8)$$

where

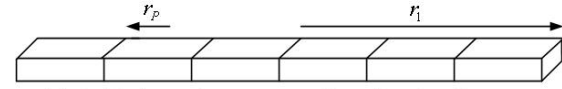
$$F_p = P^{1-2\alpha\beta} \quad (9)$$

is the factor to convert the single cell to the P cell CPU time. For the three cases above

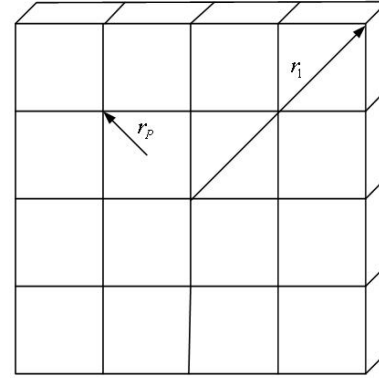
- 1D Body: $F_p = P^{1-2(1)(1.45)} = P^{-1.9}$,
- 2D Body: $F_p = P^{1-2(1/2)(1.45)} = P^{-0.45}$,
- 3D Body: $F_p = P^{1-2(1/3)(1.45)} = P^{+0.033}$.

It follows that for 1D and 2D bodies, one should use as many cells as possible, while for 3D bodies there is always a slight disadvantage to segmentation.

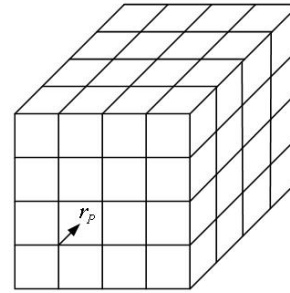
There are three important caveats to the above statement. First, one must always segment so that the SHIP cells are small enough that they are in the far zone of the points of diffraction on the scattering body. Second, equation (8) will accurately predict T_p only if $N_{HP} = N_{H1} / P^{2\alpha}$ is large enough to be on the linear portion of Figure 1. For smaller values of N_{HP} , equation (8) should be considered as qualitative only. This problem could be removed by making the slope, β a function of the number of the number of harmonics in a single cell; however, for simplicity it was not done here. Finally, it is assumed that as the radiating body is segmented, each smaller cell contains at least 1 MM current, so that rays must be traced from each SHIP cell.



(a) A 1D shape is segmented into $P = 6$ cells.



(b) A 2D shape is segmented into $P = 16$ cells.



(c) A 3D shape is segmented into $P = 64$ cells.

Fig. 2. A 1D, 2D, and 3D source is segmented in P cells.

For a 1D body radiating in the presence of the wedge, Figure 4 shows NEC-BSC CPU times for a $P = 1, 2,$ and 4 cell SHIP versus N_{H1} = the number of single cell harmonics. According to equation (7), the number

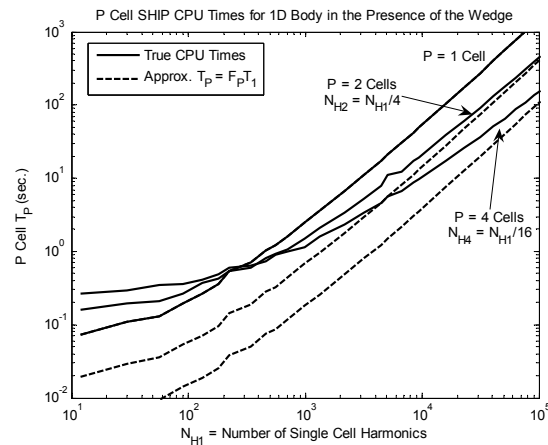


Fig. 3. CPU times for the 1D P cell SHIP in the presence of the wedge.

of harmonics *in each cell* of the P cell SHIP is $N_{H2} = N_{H1}/4$ and $N_{H4} = N_{H1}/16$. The solid lines are the actual NEC-BSC times, while the dashed lines are obtained by applying the F_p factor of equation (9). The reason that the approximation for the $P = 2$ curve is better than that for $P = 4$, is that $N_{H2} = 4N_{H4}$, and thus is more on the linear portion of the curves in Figure 1.

II. C. SHIP vs. Standard MM Current CPU Times

The CPU time for the standard approach, in which the UTD code superimposes the field of each MM current filament, is $T_{MMF} = DN_F$, where N_F is the number of MM filaments, and D is a constant dependent upon the complexity of the ray trace. For the NEC-BSC code, and the wedge of Figure 2,

$$D_{Wedge} \approx 87.8 \text{ msec.} \quad (10)$$

For the wedge, the ratio of the CPU time for the standard MM filament approach to that for the P cell SHIP is

$$R = \frac{T_{MMF}}{T_P} = \frac{D_{Wedge} N_F}{F_P (C_{Wedge} N_{H1}^\beta)} \approx \frac{5}{F_P} \frac{N_F}{(r_1/\lambda)^{2.9}}. \quad (11)$$

This indicates that the P cell SHIP will be faster than the standard filament approach if

$$\frac{N_F}{F_P (r_1/\lambda)^{2.9}} \approx \frac{N_F}{F_P (r_1/\lambda)^3} > 0.2, \quad (12)$$

i.e., if the number of MM filaments per cubic wavelength is large.

II. D. SHIP Examples

This section will present two examples illustrating the benefits of the SHIP. The first example will be a $50\lambda \times 50\lambda$ square array of dipoles over the PEC wedge of Figure 2. By making a series of runs with increasing density of dipoles within the fixed $50\lambda \times 50\lambda$ square, Figure 5 shows the UTD code CPU time versus the number of MM filaments. Since the electrical size of the source is fixed, the CPU times for the SHIP are independent of the number of MM filaments. Note that the $P = 1$ or 4 cell SHIP is faster than the standard filament approach when $N_f > 6500$ or 4200 filaments, respectively. Using $r_1 = 25\sqrt{2}\lambda$, equation (12) predicts that the $P = 1$ or 4 cell 2D SHIP will be faster than the standard filament approach when $N_f > 6200$ or 3300 filaments, respectively. The decrease in accuracy for the $P = 4$ cell SHIP is a result of not being on the linear portion of Figure 1.

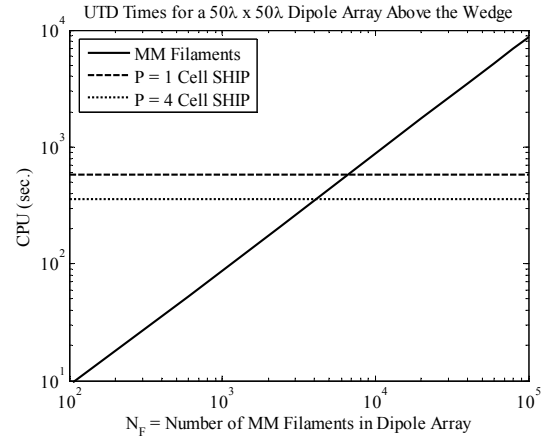


Fig. 4. UTD CPU times for a dipole array above the wedge.

Figure 6 shows a UTD plate model of a ship with a 30×30 array of $\lambda/2$ dipoles in a $15\lambda \times 15\lambda$ square. Using the standard filament approach, the UTD CPU time to compute an azimuth pattern was 351 min., but required only 261 sec. for a $P = 16$ cell 2D SHIP. This represents a reduction in CPU time by a factor of about 80. The CPU time to compute the a_{mn} and b_{mn} coefficients of equation (1) was only 61 sec.

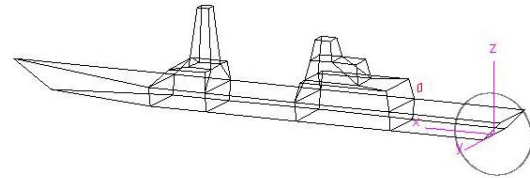


Fig. 5. A UTD model of a ship with a 30×30 array of dipoles in a $15\lambda \times 15\lambda$ square.

III. SUMMARY

This paper has described the use of a spherical harmonic expansion to reduce the UTD code CPU times in a hybrid MM/UTD solution. The advantage of the SHIP is that it reduces the number of origins from which the UTD code must trace rays. The SHIP is shown to be effective in reducing the UTD code CPU time when the number of MM filaments per cubic wavelength is large.

REFERENCES

- [1] Chen, Y., and T. Simpson, "Radiation pattern analysis of arbitrary wire antennas using

- Spherical mode expansions with vector coefficients,” *IEEE Trans. Antenna and Propagat.*, vol. 39, no. 12, pp. 1716-1721, 1991.
- [2] Chew, W., J. Jin, E. Michielssen, and J. Song, *Fast and Efficient Algorithms in Computational Electromagnetics*, Artech House, 2001.
- [3] Coifman, R., V. Roklin, and S. Wandzura, “The fast multiple method for the wave equation: A pedestrian prescription,” *IEEE Trans. Antenna and Propagat.*, vol. 35, no. 6, pp. 7-12, 1993.
- [4] Dembart, B., and E. Yup, “The accuracy of fast multipole method for maxwell’s equation,” *IEEE Computational Science Engineering*, July-Sept., pp. 48-56, 1998.
- [5] Ekelman, E. P., and G. A. Thiele (1980), “A hybrid technique for combining the moment method treatment of wires with the GTD for curved surfaces,” *IEEE Trans. Antenna and Prop.*, vol. 28, no. 11, pp. 831-839, 1980.
- [6] Marhefka, R. J., “Numerical Electromagnetic Code – Basic Scattering Code (NEC-BSC Version 4.2), Preliminary User’s Manual,” Technical Report, The Ohio State University, ElectroScience Laboratory, Columbus, Ohio, October, 2000.
- [7] Medgyesi-Mitschang, L. N., and D. S. Wang, “Hybrid methods for analysis of complex scatterers,” *Proc. IEEE*, vol. 77, no. 5, pp. 770-779, 1989
- [8] Newman, E. H., “A User’s Manual for the Electromagnetic Surface Patch Code: Version V,” The Ohio State University, ElectroScience Laboratory, Columbus, Ohio, 2005.
- [9] Rockway, J. T., “Electromagnetic Field Determination of Antenna Systems in Complex Structural Environments by the Spherical Harmonic Interface Procedure,” Ph.D. dissertation, The Ohio State University, Dept. of Elec. and Computer Engr., Columbus, Ohio, March, 2005.
- [10] Stratton, J., *Electromagnetic Theory*, McGraw-Hill, New York, 1941.
- [11] Thiele, G. A., “Overview of selected hybrid methods in radiating system analysis,” *Proc. of IEEE*, vol. 80, no. 1, pp. 66-78, 1992.
- [12] Thiele, G. A., and T. H. Newhouse (1975), “A hybrid technique for combining moment methods with the geometrical theory of diffraction,” *IEEE Trans. Antenna and Propagat.*, vol. 23, no. 1, pp. 62-69.



Jeanne T. Rockway was born in San Diego, California on April 12, 1976. She received her B.S. degree in electrical and computer engineering from the University of California of San Diego in 1998. She received her M.S. and Ph.D. degrees in electrical and computer engineering from The Ohio State University in 2001 and

2005, respectively.

Since 2005, she has worked at SAIC in San Diego. Her primary research interests deal with radar and wide band antennas.



Edward H. Newman was born in Cleveland Ohio on July 9, 1946. He received the B.S.E.E., M.Sc., and Ph.D. degrees in electrical engineering from The Ohio State University in 1969, 1970, and 1974, respectively.

Since 1974 he has been a member of the Ohio State University, Department of Electrical Engineering, ElectroScience Laboratory, where he is currently a Professor. His primary research interest is in the development of method of moments techniques for the analysis of general antenna or scattering problems, and he is the primary author of the “Electromagnetic Surface Patch Code” (ESP). Other research interests include antenna optimization, wideband impedance matching, electromagnetic shielding, and automatic array calibration. He has published over 60 journal articles in these areas, and is a coauthor of the IEEE Press book *Computational Electromagnetics (Frequency Domain Method of Moments)*.

Dr. Newman is a Fellow of the IEEE, and is a member of Commission B of URSI and the Electromagnetics Institute. He is a recipient of the 1986 and 1992 College of Engineering Research Award, and is a past chairman of the Columbus sections of the IEEE Antennas and Propagation and Microwave Theory and Techniques Societies.



Ronald J. Marhefka received the B.S.E.E. degree from Ohio University, Athens, in 1969, and the M.Sc. and Ph.D. degrees in electrical engineering from The Ohio State University, Columbus, in 1971 and 1976, respectively. Since 1969, he has been with The Ohio State University ElectroScience Laboratory where

he is currently a Senior Research Scientist and Adjunct Professor.

His research interests are in the areas of developing and applying high frequency asymptotic solutions such as the Uniform Geometrical Theory of Diffraction, hybrid solutions, and other scattering techniques. He has applied these methods to numerous practical antenna and scattering problems, including airborne, spacecraft and shipboard antenna analysis and radar cross section prediction. He is the author of two user oriented computer codes, the NEC - Basic Scattering Code and one dealing with radar cross section. The codes are being used in over 300 government, industrial, and university laboratories in the U. S. and 15 countries. In addition, he is the co-author with John Kraus on the textbook *Antennas, Ed. 3*, McGraw-Hill, 2002.

He was a co-author on papers that won the *IEEE Transactions on Antennas and Propagation* Best Application Paper Award in 1976 and the R. W. P. King Paper Award in 1976. He received The Ohio State University College of Engineering Lumley Research Award in 1992 and the Annual Research Accomplishment Award in 1999. He received the IEEE Third Millennium Medal in 2000. In addition, he was the recipient of the Applied Computational Electromagnetics Society's 1993 Technical Achievement Award. Dr. Marhefka is a Fellow of IEEE and has been elected to Tau Beta Pi, Eta Kappa Nu, Phi Kappa Phi, Sigma Xi, and Commission B of URSI. He has served as an officer of the local IEEE Antenna and Propagation and Microwave Theory and Techniques Societies during 1977-1980. He served as Associate Editor of the *IEEE Transactions on Antennas and Propagation* from 1988-1992 and was Editor from 1992-1995. He was elected a member of ADCOM in 1996, Vice President in 1997, and President in 1998. He was co-chair of the Technical Program Committee for the 2003 IEEE APS/URSI Symposium. In addition, he has chaired the AP-S Publications Committee, from 1996-2003. He also is an Associate Editor of the *Applied Computational Electromagnetics Society Journal*.

Mutual Coupling between Monopoles on F-4 Aircraft at Transition Frequencies: A Comparison between MoM and MoM/UTD Hybrid Method at UHF Band

Ali Dagdeviren^{1,2}, Osman Cerezci², Fatih Ustuner¹, Bahattin Turetken¹

¹ The Scientific and Technological Research Council of Turkey (TUBITAK), National Research Institute of Electronics & Cryptology (UEKAE), EMC-TEMPEST Test Center P.O. Box 74, Gebze, Kocaeli, TURKEY

² Sakarya University, Electrical and Electronics Engineering Faculty, Esentepe, Sakarya, TURKEY

Abstract — In this paper, the analysis of mutual coupling between monopole antennas mounted on the aircraft at UHF band is presented. The Method of Moments (MoM) and hybridized MoM with Uniform Geometrical Theory of Diffraction (UTD) method (MoM/UTD) are used to calculate the coupling in 225 MHz-400 MHz frequency range. Numerical results with MoM and MoM/UTD are performed and the reliability of these methods is discussed based on the measurement results.

Keywords — Antenna Coupling, MoM, MoM/UTD

I. INTRODUCTION

Aircrafts have many communication and navigation systems for different purposes. The radiated electromagnetic interference (EMI) between the antennas of these systems is a potential serious problem and always has to be considered. The power output of the transmitter systems, sensitivity of the receiver systems and the coupling between the antennas mainly determine the EMI safety range [1,2]. So one has to compute or measure the coupling between two antennas to decide whether a potential EMI risk exists. The analytical calculation of the coupling between surface mounted antennas on aircraft or similar complex structures is difficult and time consuming, so predictions by either numerical or asymptotic methods are preferred [3].

The electrical size of the structure to be analyzed increases at high frequencies because of the shorter wavelength. Practically, these methods can be used up to UHF band. High frequency asymptotic methods, like UTD, should be utilized for electrically large structures. However, this method also has some limitations like others. For low frequencies $kL > 1$ limitation should be considered [4]. Here k is the wavenumber and L stands for the distance parameters as defined in [4]. Generally, this method becomes practical beginning from UHF. At high frequencies, the accuracy of the model becomes a limitation [5]. So, UHF band can be considered as a transition frequency range from low frequency

methods to high frequency methods. A comparison between MoM and MoM/UTD method at transition frequencies is presented.

II. ANALYSIS

The analysis has been performed in the 225 MHz – 400 MHz frequency range between COM2/V-UHF radio communication antennas located on the top and the bottom of the fuselage and on the tail (Fig. 1). The antennas are quarter wavelength monopoles. The simulations are realized by two different methods: MoM and MoM/UTD Hybrid Method.

Two scenarios have been investigated in this work: The mutual coupling between A1-A2 and A2-A3. The location of the antennas on the aircraft can be seen in Fig. 1.

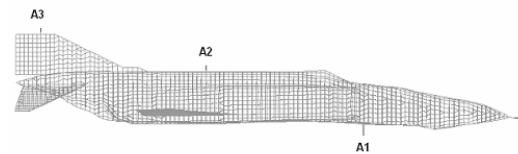


Figure 1. MoM Model and Antenna Locations.

Segment and grid sizes of around $1/10$ wavelength or less. The problem solution time is proportional to the cube of the number of segments while the computer-memory requirement is proportional to the square of the number of segments. Here, 12 cross sectional data of the model are defined, and subsequently models are generated for 175 MHz. The segment length is chosen to be equal to $\lambda/10$ at the frequency of interest. The total number of segments for the aircraft adds up to 10910.

High modeling frequency, so lower wavelength and segment length, increases the segment number of the model. For such a huge amount of segments, MoM analysis requires modeling the structure surfaces using wire segments rather than using patch model of surfaces.

Since the size of the aircraft becomes significant in terms of wavelength at UHF and above, the low frequency methods like MoM are not useful due to

long computation time and high memory requirement at these frequencies. So, an asymptotic method, the UTD is normally used. This technique based on ray tracing, considers the propagation of Electromagnetic (EM) waves as tubes of rays [6]. At each point in the space, the total EM field is calculated by superposing the incident field, reflected fields, diffracted fields and all other higher order interactions (double reflection, diffraction-reflection, reflection-diffraction etc.). In the MoM/UTD Hybrid Method, the MoM interaction Matrix is modified according to the interaction between wire segments via UTD objects: flat plates and cylinders. The MoM/UTD hybrid model of the aircraft consists of 18 plates, 9 cylinders and wire-segmented monopoles.

The technique used to hybridize the MoM and UTD was presented by Thiele and Newhouse [7-8]. Basically, the original MoM matrix elements are increased with the additional fields due to interaction mechanisms up to third order.

In short, the mn 'th element of the new impedance matrix is

$$Z'_{mn} = Z_{mn} + Z_{mn}^g. \quad (1)$$

Here Z_{mn} is due to direct field from source to observation point and Z_{mn}^g is due to other interactions (reflection, diffraction...).

The Linville method, a technique used in RF amplifier design, is used to compute the maximum coupling between the two antennas. Then mismatch losses are considered to reduce to maximum coupling due to input and output load mismatches. The maximum coupling according to Linville method is [9]:

$$C_{\max} = \frac{1 - \sqrt{1 - L^2}}{L} \quad (2)$$

where

$$L = \frac{|Y_{12} Y_{21}|}{2 \operatorname{Re}[Y_{11}] \cdot \operatorname{Re}[Y_{22}] - \operatorname{Re}[Y_{12} Y_{21}]} \quad (3)$$

As can be seen in the equation above, to calculate the maximum coupling given in eq.(2), firstly the two-port admittance parameters for the coupled antennas should be determined by exciting each antenna with the other short-circuited, then the self and mutual admittance from the currents computed by NEC should be computed [9].

In case of maximum coupling load admittance on antenna 2 must be matched[10]:

$$Y_L = \left[\frac{1 - \rho}{1 + \rho} + 1 \right] \operatorname{Re}[Y_{22}] - Y_{22} \quad (4)$$

where

$$\rho = \frac{C_{\max} (Y_{12} Y_{21})^*}{|Y_{12} Y_{21}|} \quad (5)$$

and the corresponding input admittance of antenna 1 is:

$$Y_{IN} = Y_{11} - \frac{Y_{21} Y_{12}}{Y_L + Y_{22}} \quad (6)$$

The mismatch losses are calculated according to:

$$\begin{aligned} \text{MLin} &= 10 \cdot \log(1 - |\Gamma_{in}|^2) \\ \text{MLout} &= 10 \cdot \log(1 - |\Gamma_{out}|^2) \end{aligned} \quad (7)$$

where

$$\begin{aligned} \Gamma_{in} &= \frac{Z_{in} - Z_o}{Z_{in} + Z_o} \\ \Gamma_{out} &= \frac{Z_L^* - Z_o}{Z_L^* + Z_o} \end{aligned} \quad (8)$$

III. MEASUREMENT AND RESULTS

Antenna coupling measurements have been performed in an 8.4m x 4.8m x 3.3m Semi-Anechoic Chamber (SAC). A 1:10 scaled model of the F-4 aircraft was used. The measurement setup picture can be found in Fig. 2 and depicted in Fig. 3.



Figure 2. Coupling Measurements in SAC.

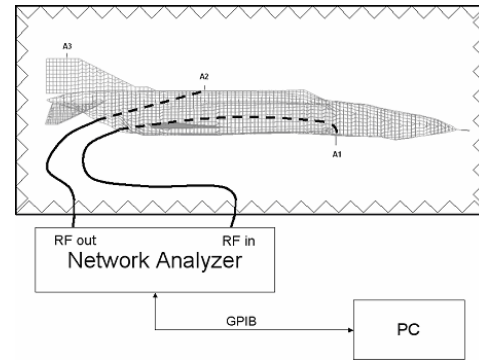


Figure 3. Detailed Measurement Setup Drawing in SAC.

The inner dimensions of the room are approximately 7.2 m long, 3.6 m wide, and 2.7 m high from the tip of the absorbers.

The frequency range to be considered for the analysis is 225 MHz-400 MHz. The aircraft model has 1:10 scaling, so the measurement was performed in 2.25

GHz-4 GHz frequency range. S_{21} , S_{11} , S_{22} parameters were measured via the network analyzer, then mismatch losses and optimum coupling were calculated according to these scattering parameters:

$$ML_1 = 10 \cdot \log(1 - |S_{11}|^2) \quad (9)$$

$$ML_2 = 10 \cdot \log(1 - |S_{22}|^2) \quad (10)$$

$$C = 10 \cdot \log(|S_{21}|^2) - ML_1 - ML_2. \quad (11)$$

The MoM coupling and MoM/UTD Hybrid method coupling between three antennas on aircraft were computed, then measured in SAC and plotted (See Fig. 4. and Fig. 5).

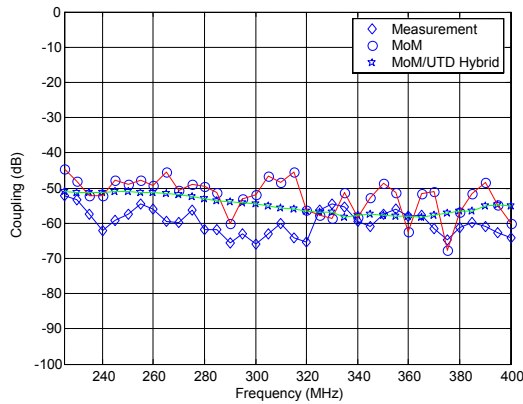


Figure 4. Coupling Between A1 and A2.

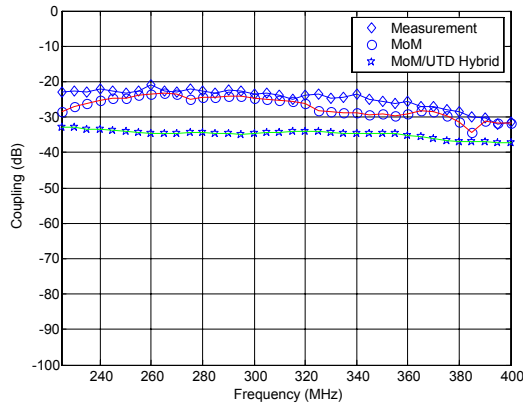


Figure 5. Coupling Between A2 and A3.

IV. CONCLUSION

In this work an efficient approach to the numerical analysis of mutual coupling between the UHF communication antennas of F-4 aircraft has been presented. The results show that coupling gathered from both methods approximated to measurement results nearly by ± 10 dB. MoM results are closer to the measurement results with respect to MoM/UTD results.

The accuracy of the simulation results depends on how precisely the model represents the aircraft. For the measurements, the precision of the scaled model

used in the measurements influences the measurement accuracy. In the case of MoM/UTD, the number of objects used and the number of maximum interactions allowed by the software affects the simulation results. In the case of MoM, wire grid size is important for the accuracy of the results. Detailed information can be found in [11] and [12].

The authors emphasize that one will better use MoM model even at the transition frequencies. A quick analysis for simplified MoM/UTD model of the complex structure can be carried out for introductory information and at higher frequencies it will be mandatory to use this model.

ACKNOWLEDGEMENT

The authors would like to thank to M. Emre Aydemir for the aircraft model, Ersan Baran for his kind help in carrying out the measurements and Nazlı Candan for her constructive suggestions on manuscript.

V. REFERENCES

- [1] M. D. Siegel, "Aircraft antenna-coupled interference analysis," in *Proc. Nat. Aerospace Electronic Conf.*, Dayton, OH, 1969, pp. 535-540.
- [2] F. Ustuner, O. Cerezci, N. Ari, S. Seker, Z. Demir, and B. Kilic, "Theoretical and experimental investigation of box-to-antenna coupled EMI noise on a helicopter under the influence of rotors," *IEEE International Symposium on Electromagnetic Compatibility*, 2003. EMC '03. 2003 Vol. 1, pp. 11-16.
- [3] B. Turetken, F. Ustuner, E. Demirel, and A. Dagdeviren, "EMI/EMC Analysis of Shipboard HF Antenna By Moment Method," *IEEE Symposium, International Conference on Mathematical Methods in Electromagnetic Theory*, June 26 – July 1, 2006, Kharkiv, Ukraine.
- [4] D.A. McNamara, C. W. I. Pistorius, and J. A. G. Malherbe, *Introduction to The Uniform Geometrical Theory of Diffraction*, Artech House, 1990.
- [5] W.D. Burnside, and R. J. Marhefka, "Antennas on Aircraft, Ships, or Any Large, Complex Environment," Chapter 20 in *Antenna Handbook* edited by Y T Lo and S W Lee.
- [6] R.G. Kouyoumjian, and P. H. Pathak, "A uniform geometrical theory of diffraction for an edge in a perfectly conducting surface," *IEEE Proceedings*, 62, Nov., 1974, pp. 1448-1361.
- [7] G. A. Thiele, AND T. H. Newhouse, "A hybrid technique for combining moment methods with the geometrical theory of diffraction," *IEEE Transactions on Antennas and Propagation*, Vol. Ap-23, No.1, January 1975.

- [8] E. P. Ekelman, and G. A. Thiele, "A hybrid technique for combining the moment method treatment of wire antennas with the GTD for curved surfaces," *IEEE Transactions on Antennas and Propagation*, Vol. Ap-28, No.6, November 1980.
- [9] D. Rubin, "The Linville Method of High Frequency Transistor Amplifier Design," *Naval Weapons Center, Research Department, NWCCL TP 845, Corona Laboratories, Corona, California*, March 1969.
- [10] SuperNEC MoM Technical Reference Manual.
- [11] SuperNEC GUI Input User Reference Manual v. 2.55.
- [12] C.W. Trueman, and S.J. Kubina, "Verifying Wire-grid Model Integrity with Program 'Check'," *ACES Winter 1990*, Vol. 5, No. 2.



Fatih Ustuner received his BS and MS degrees from Middle East Technical University in 1991 and 1994 respectively. He worked as an RF design engineer in ASELSAN Inc. from 1991 till the end of 1994. After completing his compulsory military duty, he joined TUBITAK UEKAE (National Research Institute of Electronics and Cryptology), Turkey, in 1996. He was involved EMI/EMC and all other aspects of the electromagnetic environmental effects (E3). He was completed his PhD in Sakarya University in the year 2002. He currently directs the EMC TEMPEST Test Center in TUBITAK UEKAE.



Ali Dagdeviren received his BSEE from Bilkent University, Turkey, in 1999 and MSEE from Gebze Institute of Technology, 2002. He has been working in the EMC Laboratory of The Scientific and Technical Research Council of Turkey (TUBITAK), National Research Center on Electronics and Cryptology (UEKAE) since 1999. Also he has been carrying out his PhD in Sakarya University since 2002. His research interests are mainly, asymptotic techniques in electromagnetics, RF & Microwave Circuit Design, Electromagnetic Compatibility.



Bahattin Türetken has received his B.Sc. from Yildiz Technical University in 1995, M.Sc. and PhD. degrees from Istanbul Technical University, Istanbul, Turkey in 1998 and 2002 respectively. He has been working as a senior researcher at TUBITAK-UEKAE (National Research Institute of Electronics and Cryptology) EMC & TEMPEST Test Center. He was awarded "Young Scientist Award" by URSI in 1999. He has been involved in civilian and military EMC testing, Computational Electromagnetics, Diffraction & Scattering EM Problems, Antenna Design and Application, Wiener-Hopf Technique.



Osman Cerezci received his PhD degree in 1985. Since obtaining his doctoral degree, he has carried out research in numerous branches of electromagnetic scattering and investigation of biological effects of fields. He is presently head of the department of Electrical and Electronics Engineering at Sakarya University, Turkey.

A New Iterative Method to Compute the Higher Order Contributions to the Scattered Field by Complex Structures

F. Saez de Adana, O. Gutiérrez, L. Lozano, M.F. Cátedra
 Dprt. de Ciencias de la Computación.
 Universidad de Alcalá ,28806 Alcalá de Henares (MADRID), SPAIN
 Fax: + 34 91 885 66 99
 email: kiko.saez@uah.es

Abstract – A method to compute the higher order contributions to the scattered field by complex structures is presented in this paper. The method is based on a new interpolation technique to represent the induced current with a very low amount of sample points and computational cost. The amplitude and phase of the current are represented separately. Both are defined by an interpolating function, which is built using Bézier surfaces. These functions provide the amplitude and the phase at any given point of the scattering surface in an easy way. The higher order contributions to the scattered field are obtained by using a new iterative method based on Physical Optics (PO) and the Stationary Phase Method (SPM) to compute the integral. The proposed method takes advantage of the saving in computation cost offered by the new representation of the currents reducing the order of the function which is necessary to minimize, in order to obtain the stationary phase points required to evaluate the PO integral. The results obtained show that the method is both efficient and accurate.

I. INTRODUCTION

The main contributions to the scattered field by a simple object in presence of an electromagnetic wave are mainly due to the first order effects (reflections or diffractions). However, if the complexity of the body increases (for example, an airplane, a satellite or a ship), then higher order contributions (double-reflections, diffraction-reflections, etc) become relevant, especially for certain angular margins. There are many other situations where higher order effects are relevant: the analysis of antennas onboard complex structures, the study of propagation in tunnels, the computation of the RCS of cavities, etc. In these cases, multiple reflections and /or diffractions generally, make the greatest contribution to the scattered field.

Traditionally, there are some approximate methods to tackle the problem of high order interactions for asymptotically high frequencies. The Image Method (IM) [1-3] obtains multiple reflections by repeatedly applying the Image Theory [4], calculating multiple images of the electromagnetic

source and from these the scattered field at the observation point. The main problem with this technique is that the reflecting surfaces must be flat. Another method is the Shooting and Bouncing Rays (SBR) approach, [5-8], in which tubes of rays are shot from the source in all directions. When the tube reaches the observation point after reflecting in the body surface, the previously computed field intensity level at that point is amended with the tube's contribution to the field level. The main problem with this method is the high number of rays that must be shot to obtain the scattered field accurately enough, making the computational cost very high. As it is stated in [9] an exceedingly large number of rays must be traced for very high frequencies (sometimes up to 350 points per square wavelength). Another important problem is the treatment of the diffraction due to the high number of tubes of rays in the Keller's cone produced when an incident tube of rays reaches an edge.

Other possibilities are the inverse methods based on the Geometrical Theory of Diffraction (GTD/UTD) [10,11] or the SPM [12], in which, given the structure, the source and the observation points, all the possible reflection and diffraction paths connecting the source with the observation points are obtained, taking into consideration the contribution of certain flash-points to the scattered field: reflection points in GTD/UTD or stationary phase points in SPM. The main problem with these methods is obtaining the flash-points on the surfaces involved.

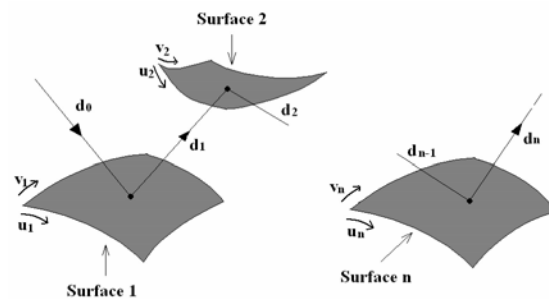


Fig. 1. Path to minimize for n reflections.

For example, Figure 1 shows a situation where a source and an observation point are placed in the vicinity of n arbitrary surfaces. If one wants to compute the reflected field at the observation point due to an n -order reflection in the surfaces of the scene, the first thing to do, using inverse methods, is to obtain the position of the n reflection points. If the geometrical surfaces are represented by parametrical surfaces (NURBS or Bézier surfaces [13,14]) as it is stated in [10] and [12], the reflection points are obtained after the minimization of the following function:

$$\begin{aligned}
 d^n(u_1, v_1, u_2, v_2, \dots, u_{n-1}, v_{n-1}, u_n, v_n) = & \\
 = d_0(u_1, v_1) + d_1(u_1, v_1, u_2, v_2) + & \\
 + d_2(u_2, v_2, u_3, v_3) + \dots + & \\
 + d_{n-1}(u_{n-1}, v_{n-1}, u_n, v_n) + d_n(u_n, v_n) & \quad (1)
 \end{aligned}$$

where d^n is the total distance of the ray path followed by the n -reflection, d_i the different stretches in which d^n can be divided (Figure 1) and u_i, v_i the parametrical coordinates that define the surface i (see references [12-14]). As can be seen, it is necessary to minimize a function of $2n$ variables. The problem is that the cost of this minimization increases exponentially with n .

The objective of the method proposed in this paper is to analyze electrically large bodies with multiple reflections and diffractions between its parts by computing efficiently the PO integrals using the SPM without the cumbersome and time-consuming problems of minimizing a function of n variables as demand the inverse ray tracing methods or the need to shooting a huge number of ray tubes as requires the SBR method. The proposed method combines the interpolation of the induced current by means of the current modes proposed in [15] with the SPM [16, 17] to obtain the scattered field. As stated in [15] the current is interpolated by means of a Bezier surface from the induced currents on a set of sampling points over the surface. Given the behavior of Bezier surfaces 8×8 sampling points are a number optimum for a good representation of the current. After the interpolation the critical points of SPM can be obtained minimizing the phase function of the PO integrand that includes the phase of the induced current. As it will be described below, there is no relationship between the SPM critical points and the control points. Therefore, the interpolation process is independent of the SPM computation.

From that, an iterative method to compute multiple order reflections and/or diffractions has been developed. The method consists, basically, of calculating iteratively the induced current in each surface involved in the reflection to obtain the scattered field at the reflection point. In each surface the induced current is expressed in terms of a current

mode. The definition of a current mode is an exponential function whose amplitude and phase are smooth functions that can be easily interpolated from their values in a reduced number of sampling points. The current in the sampling points in a surface (passive surface) is obtained from the fields at that points due the current mode defined in a surface (active surface) that is illuminating by reflection the passive surface. These fields are computed by the SPM and as it will be shown. To perform this computation it is only necessary the minimization of several functions of two variables, avoiding the minimization of functions of more than two variables necessary in the inverse methods and the shooting of a large amount of rays necessary in the SBR, reducing consequently the computation time as will be illustrated in the Results section. Once the current mode in the passive surface has been obtained, this surface is considered as the active surface and therefore it will illuminate a new surface (the new passive surface) in the next step of an iterative procedure to solve the multiple iteration problems arising in scattering and radiation problems with complex bodies.

The proposed method is advantageous with respect to the SBR because it provides the possibility of the computation of multiple interactions between large objects sampling the surface of the objects with a low amount of points, amount which is independent of the frequency. On the other hand with respect to the inverse methods presented in [10-12], the advantage is that the functions to minimize depends only on two variables, independently of the number of surfaces involved in the multiple interaction. These advantages are possible due to the most important technical combination of this paper: the combination of the SPM with the interpolation of the induced currents over a body by using Bézier surfaces.

It is important to bring out that the presented approach can be considered iterative in the sense that the PO current integrated by the SPM in the surface for a multiple interaction is computed iteratively for a surface taking into account the current of the surface considered in the previous iteration using in each surface the classical PO approach. There are other Iterative Physical Optics (IPO) approaches in the literature, which basically try to solve the Magnetic Field Integral Equation (MFIE) using IPO [18, 19] as an alternative of a matrix solution of the MFIE. The idea of our approach is not to solve any integral equation, but to provide an alternative to the classical ray methods used to compute higher order contributions in high frequency.

This paper is arranged as follows. Part 2 summarizes the procedure to obtain by interpolation the phase and amplitude functions that define a current mode. Part 3 shows how to compute the PO

integral due to a current mode for an observation point in the near or the far field by using the SPM. The iterative method considered for the computation of the multiple interactions between the different surfaces of a complex body is described in Part 4. Results for problems with double reflection, triple reflection and higher order reflection in a rectangular cavity are presented in Part 5 to show the performances of the proposed approach. Finally, in Part 6, the conclusions and the main features of the approach are summarized.

II. INTERPOLATION OF THE INDUCED CURRENT BY BÉZIER SURFACES

As mentioned above, the interpolation of the induced current was outlined in [15] and consists basically in using, as parameter interpolating function for each current mode, a Bézier surface to interpolate each component of the amplitude vector and another to interpolate the phase function. To interpolate the bi-dimensional scalar function Φ from a set of $(m+1)(n+1)$ values of the function, the control points of the Bézier surface are obtained by solving the following equation:

$$\mathbf{b} = \mathbf{U}^{-1} \Phi \mathbf{V}^{-1} \quad (2)$$

where:

$$\mathbf{b} = \begin{bmatrix} \bar{b}_{00} & \cdots & \bar{b}_{0n} \\ \vdots & \ddots & \vdots \\ \bar{b}_{m0} & \cdots & \bar{b}_{mn} \end{bmatrix}_{(m+1)(n+1)} \quad (3)$$

$$\Phi = \begin{bmatrix} \bar{\varphi}_{00} & \cdots & \bar{\varphi}_{0n} \\ \vdots & \ddots & \vdots \\ \bar{\varphi}_{m0} & \cdots & \bar{\varphi}_{mn} \end{bmatrix}_{(m+1)(n+1)} \quad (4)$$

$$\mathbf{U} = \begin{bmatrix} B_0(u_0) & \cdots & B_m(u_0) \\ \vdots & \ddots & \vdots \\ B_0(u_m) & \cdots & B_m(u_m) \end{bmatrix}_{(m+1)(m+1)} \quad (5)$$

$$\mathbf{V} = \begin{bmatrix} B_0(v_0) & \cdots & B_n(v_0) \\ \vdots & \ddots & \vdots \\ B_0(v_n) & \cdots & B_n(v_n) \end{bmatrix}_{(n+1)(n+1)} \quad (6)$$

\bar{b}_{ij} being the control points which define the surface which interpolates the function Φ , $\bar{\varphi}_{ij}$ the sampling points of that function, and B_i the Bernstein polynomials in terms of which the Bézier surface is expressed [13,14].

The interpolation can be performed taking 8×8 samples over the surface for a good representation of the current, taking into account the behavior of Bezier

surfaces as described in [13]. The samples are usually chosen equally spaced, although it is not a mandatory condition.

III. CALCULATION OF A SIMPLE REFLECTION USING THE STATIONARY PHASE METHOD AND CURRENT MODES

The use of the SPM to obtain the radiated field of an antenna in presence of a convex object and calculate the PO integral was shown in [12]. SPM is a mathematical approach that is especially suitable to calculate integrals with rapid oscillation of the integrand phase. This situation is given for the PO integral in high frequency. For this reason, SPM is advantageous for high frequency electromagnetic analysis with respect to classical numerical techniques such as the Gauss quadratures. The SPM requires the search of a set of critical points: stationary phase or internal points, boundary points and vertex points which give the first, second and third order contribution to the PO integral. In this section, we will concentrate on the application of the current modes to obtain the first order contribution, i.e., the contribution made by the stationary phase points, to the PO integral. The other contributions could be obtained in a similar way.

Consider a body in which the electric and magnetic currents have been defined in terms of current modes. The scattered field at an observation point $\bar{\mathbf{r}}$ can be obtained by computing the PO integral on the surface S' of that object:

$$\begin{aligned} \bar{\mathbf{E}}^S(\bar{\mathbf{r}}) &= \bar{\mathbf{E}}_J^S(\bar{\mathbf{r}}) + \bar{\mathbf{E}}_M^S(\bar{\mathbf{r}}) = \\ &= -j\lambda^{-1} \left(\int_{S'} (\hat{\mathbf{k}}_s \times \bar{\mathbf{J}}(\bar{\mathbf{r}}') \times \hat{\mathbf{k}}_s) \frac{e^{jk_s(\bar{\mathbf{r}}-\bar{\mathbf{r}}')}}{|\bar{\mathbf{r}}-\bar{\mathbf{r}}'|} dS \right) + \\ &+ j\eta\lambda^{-1} \left(\int_{S'} (\hat{\mathbf{k}}_s \times \bar{\mathbf{M}}(\bar{\mathbf{r}}')) \frac{e^{jk_s(\bar{\mathbf{r}}-\bar{\mathbf{r}}')}}{|\bar{\mathbf{r}}-\bar{\mathbf{r}}'|} dS \right) \end{aligned} \quad (7)$$

where $\bar{\mathbf{E}}_J^S(\bar{\mathbf{r}})$ and $\bar{\mathbf{E}}_M^S(\bar{\mathbf{r}})$ are the contributions of the induced electric and magnetic current mode $\bar{\mathbf{J}}(\bar{\mathbf{r}}')$ and $\bar{\mathbf{M}}(\bar{\mathbf{r}}')$ to the radiated field, λ is the wavelength, η is the impedance in free space and $\hat{\mathbf{k}}_s$ is the direction of observation for far field or the unit vector which joins the point $\bar{\mathbf{r}}'$ over the surface with the observation point for near field $\left(\frac{\bar{\mathbf{r}}-\bar{\mathbf{r}}'}{|\bar{\mathbf{r}}-\bar{\mathbf{r}}'|} \right)$. The induced currents can be expressed as follows:

$$\vec{J}(\vec{r}') = \hat{n} \times \begin{bmatrix} 1 - \Gamma_s & 0 \\ 0 & 1 - \Gamma_h \end{bmatrix} \begin{bmatrix} H_s^i(\vec{r}') \\ H_h^i(\vec{r}') \end{bmatrix} \quad (8)$$

$$\vec{M}(\vec{r}') = -\hat{n} \times \begin{bmatrix} 1 + \Gamma_s & 0 \\ 0 & 1 + \Gamma_h \end{bmatrix} \begin{bmatrix} E_s^i(\vec{r}') \\ E_h^i(\vec{r}') \end{bmatrix} \quad (9)$$

where \hat{n} is the unit vector normal to the surface at point \vec{r}' , Γ_s , and Γ_h are the Fresnel reflection coefficients [4], and $H_{s,h}^i$ and $E_{s,h}^i$ are the soft and hard components (perpendicular and parallel components respectively, see [4]) of the incident magnetic and electric fields at that point of the surface.

The two terms $\vec{E}_J^S(\vec{r})$ and $\vec{E}_M^S(\vec{r})$ of equation (7) can be written as follows, expressing the current by means of the amplitude and phase terms:

$$\vec{E}_J^S(\vec{r}) = -j\lambda^{-1} \left(\int_{S'} (\hat{k}_s \times \vec{J}_0(\vec{r}') \times \hat{k}_s) \frac{e^{jk[\hat{k}_s(\vec{r}-\vec{r}')+\phi(r')]}{|\vec{r}-\vec{r}'|} dS \right) \quad (10)$$

$$\vec{E}_M^S(\vec{r}) = j\eta\lambda^{-1} \int_{S'} (\hat{k}_s \times \vec{M}_0(\vec{r}')) \frac{e^{jk[\hat{k}_s(\vec{r}-\vec{r}')+\phi(r')]}{|\vec{r}-\vec{r}'|} dS \quad (11)$$

where $\vec{J}_0(\vec{r}')$, $\vec{M}_0(\vec{r}')$ are the amplitude values of the electric and magnetic current respectively at a point \vec{r}' on the surface, and $\phi(\vec{r}')$ is the phase. These functions define the corresponding current mode and it is assumed they are approximated by the Bézier surface described in part 2.

To apply the SPM, the amplitude functions can be expressed as:

$$g_J(\vec{r}') = \frac{\hat{k}_s \times \vec{J}_0(\vec{r}') \times \hat{k}_s}{|\vec{r}-\vec{r}'|} \quad (12)$$

$$g_M(\vec{r}') = \frac{\hat{k}_s \times \vec{M}_0(\vec{r}')}{|\vec{r}-\vec{r}'|} \quad (13)$$

and the phase function is expressed as:

$$f(\vec{r}') = \hat{k}_s |\vec{r}-\vec{r}'| + \phi(\vec{r}') = \begin{cases} \hat{k}_s \cdot \vec{r}' & \text{for observation in far field} \\ |\vec{r}-\vec{r}'| & \text{for observation in near field.} \end{cases} \quad (14)$$

Two integrals must be solved, one for the electric current and the other for the magnetic current. In parametric coordinates we have:

$$I_J = \int_{u=0}^{u=1} \int_{v=0}^{v=1} g_J(u, v) e^{jkf(u, v)} du dv \quad (15)$$

$$I_M = \int_{u=0}^{u=1} \int_{v=0}^{v=1} g_M(u, v) e^{jkf(u, v)} du dv. \quad (16)$$

Both integrals satisfy the conditions for the application of the SPM method [16,17]. The first step in solving the integrals is to find the critical points. As mentioned above, only the internal points will be considered here. These are the points with the parametric coordinates (u_s, v_s) , where function $f(u, v)$ has a minimum, i.e., where the parametric derivatives at this point are zero:

$$\begin{cases} f_u(u_s, v_s) = \frac{\partial f}{\partial u}(u_s, v_s) = 0 \\ f_v(u_s, v_s) = \frac{\partial f}{\partial v}(u_s, v_s) = 0. \end{cases} \quad (17)$$

The derivatives of the function $f(u, v)$ are:

$$f_u(u, v) = \begin{cases} \frac{\partial \hat{k}_s \cdot \vec{r}'}{u} + \frac{\partial \phi(\vec{r}')}{u} & \text{far field observation} \\ \frac{\partial |\vec{r}-\vec{r}'|}{u} + \frac{\partial \phi(\vec{r}')}{u} & \text{near field observation} \end{cases} \quad (18)$$

$$f_v(u, v) = \begin{cases} \frac{\partial \hat{k}_s \cdot \vec{r}'}{v} + \frac{\partial \phi(\vec{r}')}{v} & \text{far field observation} \\ \frac{\partial |\vec{r}-\vec{r}'|}{v} + \frac{\partial \phi(\vec{r}')}{v} & \text{near field observation} \end{cases} \quad (19)$$

where

$$\begin{aligned} \frac{\partial |\vec{r}-\vec{r}'|}{\partial u} &= \frac{-2(x-x')^2 \frac{\partial x'}{\partial u} - 2(y-y')^2 \frac{\partial y'}{\partial u} - 2(z-z')^2 \frac{\partial z'}{\partial u}}{2\sqrt{(x-x')^2 + (y-y')^2 + (z-z')^2}} \\ &= -\hat{k}_s \cdot \frac{\partial \vec{r}'}{\partial u} \end{aligned} \quad (20)$$

$$\begin{aligned} \frac{\partial |\vec{r}-\vec{r}'|}{\partial v} &= \frac{-2(x-x')^2 \frac{\partial x'}{\partial v} - 2(y-y')^2 \frac{\partial y'}{\partial v} - 2(z-z')^2 \frac{\partial z'}{\partial v}}{2\sqrt{(x-x')^2 + (y-y')^2 + (z-z')^2}} \\ &= -\hat{k}_s \cdot \frac{\partial \vec{r}'}{\partial v} \end{aligned} \quad (21)$$

$$\frac{\partial \hat{\mathbf{k}}_s \cdot \bar{\mathbf{r}}'}{\partial \mathbf{u}} = \hat{\mathbf{k}}_s \cdot \frac{\partial \bar{\mathbf{r}}'}{\partial \mathbf{u}} \quad (22)$$

$$\frac{\partial \hat{\mathbf{k}}_s \cdot \bar{\mathbf{r}}'}{\partial \mathbf{v}} = \hat{\mathbf{k}}_s \cdot \frac{\partial \bar{\mathbf{r}}'}{\partial \mathbf{v}} \quad (23)$$

$\frac{\partial \phi(\bar{\mathbf{r}}')}{\mathbf{u}}$ and $\frac{\partial \phi(\bar{\mathbf{r}}')}{\mathbf{v}}$ can be easily obtained as the

derivatives of the current mode and $\frac{\partial \bar{\mathbf{r}}'}{\mathbf{u}}$ and $\frac{\partial \bar{\mathbf{r}}'}{\mathbf{v}}$ can be obtained as the derivatives of the Bézier surface which describes the scattered object. The expressions for the derivatives of a Bézier surfaces can be seen in reference [13].

Then, if the derivatives of the Bézier surface which describes the body are denoted as $\bar{\mathbf{r}}'_u$ and $\bar{\mathbf{r}}'_v$, the system of equations to solve is the following, corresponding the sign + to observation in far field and the sign - to observation in near field:

$$\begin{cases} \left(\frac{\partial \phi(\bar{\mathbf{r}}')}{\mathbf{u}} \right) \pm \hat{\mathbf{k}}_s \cdot \bar{\mathbf{r}}'_u \Big|_{(u_s, v_s)} = 0 \\ \left(\frac{\partial \phi(\bar{\mathbf{r}}')}{\mathbf{v}} \right) \pm \hat{\mathbf{k}}_s \cdot \bar{\mathbf{r}}'_v \Big|_{(u_s, v_s)} = 0. \end{cases} \quad (24)$$

The Conjugate Gradient Method [20] has been used to solve the system of equations in our examples. Once the critical point has been obtained, its contribution to the PO integral is expressed as follows [12]:

$$\begin{aligned} \bar{\mathbf{I}}_J &= \frac{\pi}{k} \frac{e^{jk[\hat{\mathbf{k}}_s(\bar{\mathbf{r}} - \bar{\mathbf{r}}'(u_s, v_s)) + \phi(u_s, v_s)]}}{|\bar{\mathbf{r}} - \bar{\mathbf{r}}'(u_s, v_s)|} \\ &\times \frac{\hat{\mathbf{k}}_s \times \bar{\mathbf{J}}_0(u_s, v_s) \times \hat{\mathbf{k}}_s}{\sqrt{|f_{uu}^S \cdot f_{vv}^S - (f_{uv}^S)^2|}} e^{j\frac{\pi}{4}\sigma(\delta+1)} \end{aligned} \quad (25)$$

$$\begin{aligned} \bar{\mathbf{I}}_M &= \frac{\pi}{k} \frac{e^{jk[\hat{\mathbf{k}}_s(\bar{\mathbf{r}} - \bar{\mathbf{r}}'(u_s, v_s)) + \phi(u_s, v_s)]}}{|\bar{\mathbf{r}} - \bar{\mathbf{r}}'(u_s, v_s)|} \\ &\times \frac{\hat{\mathbf{k}}_s \times \bar{\mathbf{M}}_0(u_s, v_s)}{\sqrt{|f_{uu}^S \cdot f_{vv}^S - (f_{uv}^S)^2|}} e^{j\frac{\pi}{4}\sigma(\delta+1)} \end{aligned} \quad (26)$$

with

$$\sigma = \text{sign}(f_{uv}^S) \quad \text{and} \quad \delta = \text{sign}\left[f_{uu}^S \cdot f_{vv}^S - (f_{uv}^S)^2\right],$$

f_{uu}^S , f_{vv}^S and f_{uv}^S being the second derivatives of the phase at the point (u_s, v_s) . These are easily computed, deriving (18) and (19):

$$\begin{aligned} f_{uu}^S &= \frac{\partial}{\mathbf{u}} \left(\frac{\partial \phi(\bar{\mathbf{r}}')}{\mathbf{u}} \pm \hat{\mathbf{k}}_s \cdot \bar{\mathbf{r}}'_u \right) \Big|_{(u_s, v_s)} \\ &= \frac{\partial^2 \phi(\bar{\mathbf{r}}')}{\mathbf{u}^2} \pm \hat{\mathbf{k}}_s \cdot \bar{\mathbf{r}}''_{uu} \pm \frac{1}{|\hat{\mathbf{k}}_s|} \times \\ &\quad \left\{ (\bar{\mathbf{r}}'_u \cdot \bar{\mathbf{r}}'_u) - (\bar{\mathbf{r}}'_u \cdot \hat{\mathbf{k}}_s)^2 \right\} \Big|_{(u_s, v_s)} \end{aligned} \quad (27)$$

$$\begin{aligned} f_{vv}^S &= \frac{\partial}{\mathbf{v}} \left(\frac{\partial \phi(\bar{\mathbf{r}}')}{\mathbf{v}} \pm \hat{\mathbf{k}}_s \cdot \bar{\mathbf{r}}'_v \right) \Big|_{(u_s, v_s)} \\ &= \frac{\partial^2 \phi(\bar{\mathbf{r}}')}{\mathbf{v}^2} \pm \hat{\mathbf{k}}_s \cdot \bar{\mathbf{r}}''_{vv} \pm \frac{1}{|\hat{\mathbf{k}}_s|} \times \\ &\quad \left\{ (\bar{\mathbf{r}}'_v \cdot \bar{\mathbf{r}}'_v) - (\bar{\mathbf{r}}'_v \cdot \hat{\mathbf{k}}_s)^2 \right\} \Big|_{(u_s, v_s)} \end{aligned} \quad (28)$$

$$\begin{aligned} f_{uv}^S &= \frac{\partial}{\mathbf{u}} \left(\frac{\partial \phi(\bar{\mathbf{r}}')}{\mathbf{v}} \pm \hat{\mathbf{k}}_s \cdot \bar{\mathbf{r}}'_v \right) \Big|_{(u_s, v_s)} \\ &= \frac{\partial^2 \phi(\bar{\mathbf{r}}')}{\mathbf{u}\mathbf{v}} \pm \hat{\mathbf{k}}_s \cdot \bar{\mathbf{r}}''_{uv} \pm \frac{1}{|\hat{\mathbf{k}}_s|} \times \\ &\quad \left\{ (\bar{\mathbf{r}}'_u \cdot \bar{\mathbf{r}}'_v) - (\bar{\mathbf{r}}'_u \cdot \hat{\mathbf{k}}_s)(\bar{\mathbf{r}}'_v \cdot \hat{\mathbf{k}}_s) \right\} \Big|_{(u_s, v_s)} \end{aligned} \quad (29)$$

In equations (27-29) the sign + corresponds to observation in far field and the sign - to observation in near field. It is important to take into account the possibility of not all the surface is illuminated. In this case, only the illuminated part of the surface is considered to interpolate the current. Then, it appears a shadow boundary which contribution should be considered introducing a second order critical point as is shown in [12].

Equations (25) and (26) illustrate the advantage of the SPM with respect to other numerical integration techniques, because the value of the integral is reduced to the evaluation of a closed formula to evaluate the contribution of each critical point and the further summation of all the contributions. As it is stated in [12], there is, as much, only one first order critical point, four second order critical points and four third order critical points in each parametric surface that defines the geometry. On the other hand, there is necessary to evaluate the integrand for a high amount of points in a classical numerical integration technique (usually with an step of $\lambda/10$ in the PO application, due to the rapid variation of the integrand's phase). Therefore, the number of operations involved in the calculation of the integral using the SPM is clearly inferior giving the computational advantage of this technique for integrals with rapidly variation integrand's phase,

typical situation in the analysis of electrically large electromagnetic problems.

It is also important to highlight that the position of the critical point is independent of the sampling points chosen to interpolate the current, being both procedures (the interpolation and the SPM computation) completely independent. In this section, the objective is only to show the applicability of the current interpolation to the analysis of scattered field by means by SPM, but there is not advantage with respect to the SPM computation without current interpolation. The advantage appears, as it is stated in next Section, when multiple interactions between different parts of a complex body must be considered to obtain the total scattered field.

An example is presented here to show the accuracy of the application of the current interpolation to the SPM. In the example, indicated in Figure 2, a comparison between the results obtained with the proposed approach and those obtained using a GTD/UTD is presented. The GTD/UTD results have been obtained with the code FASANT whose accuracy has been proven in [10]. The surface in Figure 2 is a quarter of a sphere whose sides are $2.35\lambda \times 2.35\lambda$. The frequency is 300 MHz. The surface is a perfect electric conductor coated with an absorbing material that has both electric and magnetic losses with $\epsilon_r=2.5-j1.25$, $\mu_r=1.6-j0.8$ and a thickness of $\tau=0.15\lambda$. The electromagnetic illumination is by a vertical dipole placed at 12λ from the center of the sphere. The dipole's coordinates are $(2.0,3.0,0.0)$ and it is orientated according to the Z-axis of the reference system (X, Y, Z) depicted in Figure 2. The observation points are located along a line from $(4.0,2.0,0.0)$ to $(4.0,2.0,4.0)$. The minimum distance from the surface is 14.9λ . The comparison of the results of both methods is depicted in Figure 3, in which a close correspondence between both results can be observed.

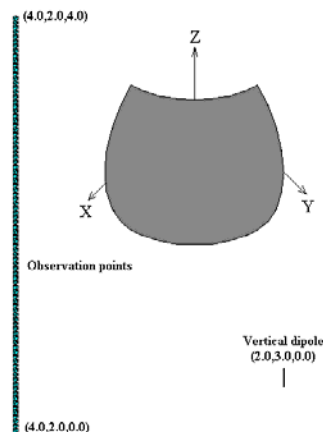


Fig. 2. Spherical section illuminated by a dipole. Position of the observation points where the scattered field is computed.

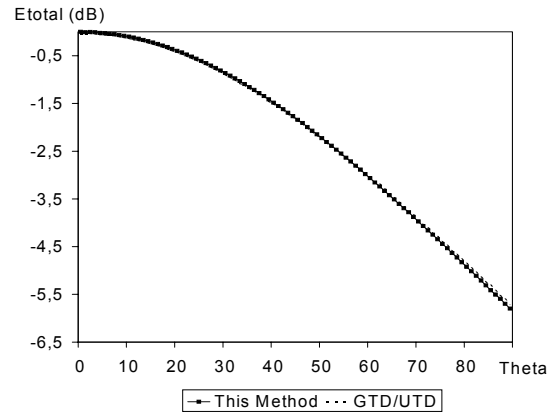


Fig. 3. Scattered field by the spherical sector illuminated by a vertical dipole.

IV. ITERATIVE METHOD FOR THE COMPUTATION OF HIGHER ORDER REFLECTIONS

When only single reflections are to be evaluated, the usage of the current interpolation approach, presented in Section 3 is not advantageous, because it replaces the minimization of the function distance that, in this case, depends on two variables, by the minimization of an interpolated phase function that depends also on two variables. Therefore, there is no gain in the minimization procedure. Moreover, the interpolation of the phase function requires the prior evaluation of the current at a set of sampling points and the corresponding interpolation using parametric interpolating surfaces. Therefore, the computation time is higher than when using a direct ray tracing to compute the stationary phase points, as stated in [12]. However, the application of a direct ray-tracing to obtain multiple reflections is much more complex, because it requires the minimization of a function with $2n$ variables, which exponentially increases the computation with n , as was mentioned in the introduction.

The solution proposed in this paper consists of applying an iterative method in which the current induced over the surfaces involved in the multiple reflections is computed sequentially. Therefore, to obtain the current induced over a surface, it is necessary to know the current over the previous one. The interpolation method is used, as it only needs to store a small amount of information to accomplish this calculation.

Let us suppose a surface that we will call active surface, over which its induced current is defined by means of the current value at a set of control points. We will compute the induced current over another

surface (the passive surface), induced by the field radiated by the currents of the active surface. For that, a mesh of points over the passive surface is defined as depicted in Figure 4. In this mesh, we will compute the impressed field and from that the corresponding induced current. The mesh corresponds to the control points, which interpolate the current surface and the impressed field at each control point of the passive surface can be computed using the interpolated current of the active surface following the procedure described in Section 3.

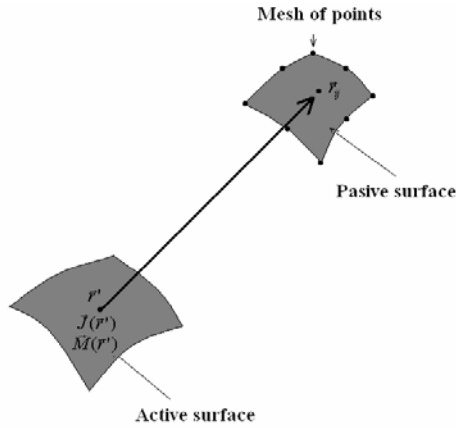


Fig. 4. Interpolation of the current on the passive surface.

This procedure can be applied iteratively. Beginning at the source that illuminates a certain structure, the radiated field can be obtained in a given direction from the multiple reflections produced. The iterative method is carried out as follows:

- a) The surfaces illuminated by the source are determined. These are the passive surfaces in the first iteration.
- b) The impressed field at a set of sampling points is computed for each passive surface. From these values the equivalent currents are interpolated.
- c) The next iteration starts. The passive surfaces become active.
- d) The surfaces illuminated by the active surfaces are determined. These become the passive surfaces.
- e) If it is the last iteration, it is checked. If not, the procedure is repeated from stage b.

An important task in the procedure is to select the passive surfaces for a given active surface. If there is not prior knowledge of which these surfaces are, all the surfaces of the model can be passive except the active. However, as it is stated in [21] the stationary phase points of the SPM correspond to the reflection points of Geometrical Optics. Therefore, the ray that joins the source with the stationary phase point and

the one that joins this point with the observation point must satisfy the Snell's law. From that, a previous selection of passive surfaces can be accomplished, determining the region of the space that satisfies the Snell's law from any point of the active surface. Only the surfaces places total or partially inside of this region can be passive surfaces. This previous selection allows reducing considerably the number of passive surfaces selected and, as a consequence, the time required for the iterative procedure. A similar reasoning can be done for the boundary and vertex critical points according of the properties of such points, described in [21].

An example with three surfaces illuminated by a plane wave with a direction of incidence \hat{k}_i , is depicted in Figure 5. Surface 1 is selected as the passive surface for the first step of the scheme, calculating the impressed field at each control point of the surface and from this the equivalent currents, which are denominated $\vec{J}^{(1)}, \vec{M}^{(1)}$. Once these currents have been determined, surface 1 becomes the active surface.

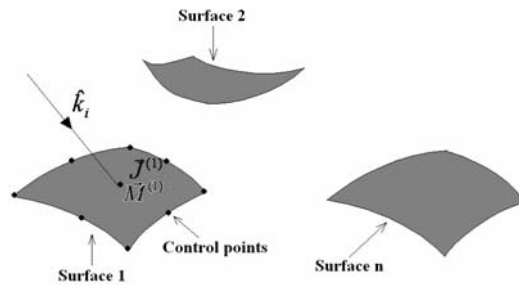


Fig. 5. First step of the iterative process. Computation of the induced currents by the incident plane wave.

The next step is to determine the radiation directions of the currents $\vec{J}^{(1)}, \vec{M}^{(1)}$ and to obtain the new passive surface. Surface 2 is the passive surface in our example. The impressed field over the control points of this surface is computed and the equivalent currents $\vec{J}^{(2)}, \vec{M}^{(2)}$ are obtained (Figure 6).

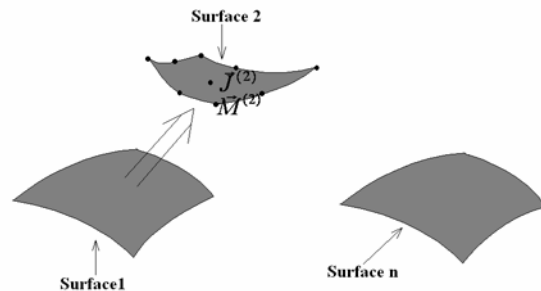


Fig. 6. Computation of the equivalent currents over surface 2 in the second step of the iterative process.

In the next step, surface 2 becomes the active surface and surface 3 the passive. The same procedure described above is applied and the equivalent currents on the surface 3 ($\vec{J}^{(3)}, \vec{M}^{(3)}$) are obtained. From these currents, the radiated field can be obtained (Figure 7).

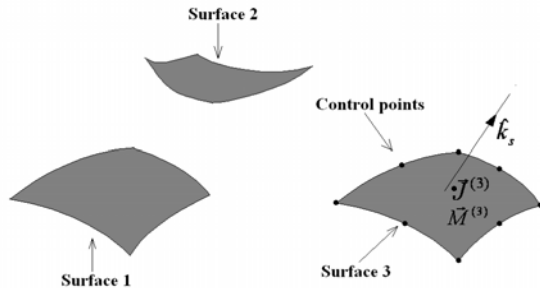


Fig. 7. Scattered field in the direction \hat{k}_s from the current calculated in the last step of the iterative process.

It is important to remark that to obtain the induced currents over the passive surfaces in each iteration, it is only necessary to calculate the radiated field by the previous surface (the active surface) from its induced currents. As these currents are represented by means of interpolated functions which depend only on the parametric coordinates of the active surface, each iteration requires several minimizations of functions of two variables, so many as sampling points are considered. Then, the minimization of a function of n variables mentioned in the introduction is being replaced by an iterative procedure consisting in the minimization of functions of two variables. As the number of sampling points in each surface is not necessary to be big as was proved in [15] the number of this functions to minimize is small and the computation time is reduced drastically as will be shown in the Results section.

V. RESULTS

In this section, the proposed method is validated comparing with the results obtained by the SPM without interpolation and by GTD/UTD for some simple cases. The comparison between the features both techniques (SPM and GTD/UTD) can be seen in [20]. These cases also illustrate the reduction in CPU time achieved with this method. After that, the application of the interpolation to a practical case is shown. The application considered is the computation of the RCS of a cavity. In this case, the proposed method is compared with the SBR, obtaining a considerable reduction in the CPU-time as it will be seen below.

The first case analyzed consists of the two surfaces indicated in Figure 8: one flat and other curved, with a curvature such that the normal vector at the surface turns at a maximum angle of 26° when it moves along the surface. We will call this angle the “maximum turning angle” of the surface. Both surfaces in Figure 8 have sides of 4 m, which is equivalent to 13.33λ and they are considered to be perfect electric conductors (PEC) coated with a material with electric and magnetic losses, characterized by a dielectric constant of $\epsilon_r=2.5-j1.25$, a magnetic constant of $\mu_r=1.6-j0.8$ and a thickness of 0.15λ . The geometry is illuminated by a vertical dipole placed at point $(0.0,-6.0,0.0)$ as shown in Figure 8. The observation points were situated along a line from $(0.0,0.0,6.0)$ to $(0.0,4.0,4.0)$. Figure 9 shows a clear agreement between results obtained with the proposed method and those obtained with GTD/UTD.

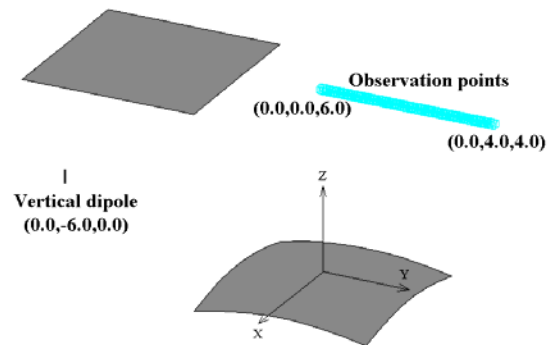


Fig. 8. Planar surface with 4 meters per side and convex surface with 4 meters per side and maximum turning angle of 26° .

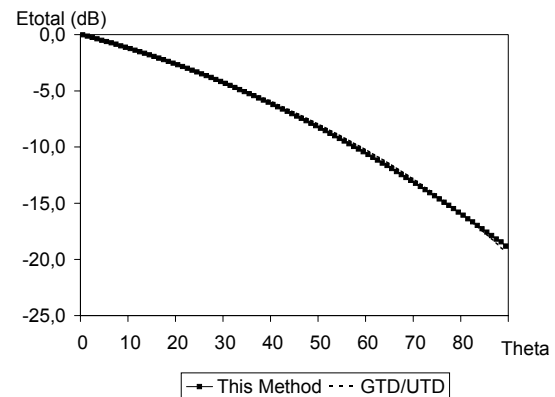


Fig. 9. Amplitude of the scattered field due to the double reflection between a planar surface and a convex surface coated with a material with losses.

The next geometry analyzed is depicted in Figure 10 and consists of three flat surfaces. The first is a PEC and the others are PECs coated with a material

with the same constants as the previous case. The plates have sides of 4 m (13.33λ). A vertical dipole was placed at $(0.0,6.0,0.0)$ and the radiated field is obtained after the third reflection along a line from $(0.0,-5.0,0.0)$ to $(0.0,-9.0)$ consisting of 90 points. The comparison between the predicted values using our approach and those obtained with GTD/UTD is presented in Figure 11.

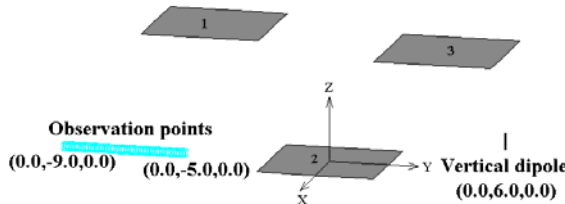


Fig. 10. Three planar surfaces.

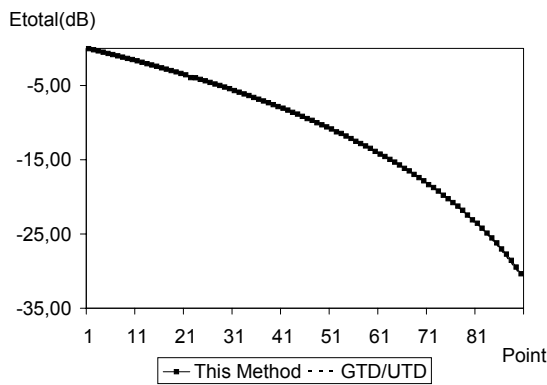


Fig. 11. Amplitude of the scattered field due to the triple reflection produced by three planar surfaces, the first a PEC and the others PECs coated with a material with losses.

To demonstrate the efficiency of the proposed approach, we can compare the difference in CPU-time needed to analyze both a flat and a convex surface. Traditional SPM takes 33 seconds whilst the interpolation method takes just 5 seconds. Both results were obtained on a Pentium III with 1 GB of RAM. Taking into account that the CPU time for the field computation is practically the same, the difference is due to the advantage of the current interpolation. Traditional SPM has to minimize a function of four variables for each observation point (90 points in the example) in order to find the stationary phase points corresponding to each observation point. On the other hand, the interpolation method has to minimize a function of two variables to obtain the induced current in each sampling point of the second surface (64 points were used, 8 in each parametric direction) and another function of two variables to find the stationary phase point corresponding to each observation point. As the induced current only has to be computed once,

90 minimizations of a function of four variables are being replaced by 154 minimizations of functions of two variables. This fact allows for the time reduction mentioned above. Therefore, the method is efficient due to the reduction of the order of minimization.

Similar conclusions can be obtained with three flat surfaces where we replace 90 six-variables sets of minimizations by 218 two-variables sets of minimizations (64 for the induced current in the second surface, 64 for the induced current in the third surface and 90 to obtain the stationary phase point corresponding to each observation point). In this case, the GTD/UTD code FASANT used for the validation is unable to treat triple-reflections on curved surfaces, requires 15 minutes and 2 seconds to perform the analysis, while the interpolation method only needs 1 minute and 23 seconds.

Finally, as mentioned above, the result of the application of the proposed method to the analysis of the RCS of a cavity is shown. The case consists in a rectangular cavity whose dimensions are $30\lambda \times 10\lambda \times 10\lambda$ (see Figure 12). The monostatic RCS was obtained varying the incidence angle for directions contained in a symmetry plane of the cavity, which contain the axis of the aperture. Figure 13 illustrates the comparison of the interpolation method with the SBR for the theta polarization. As can be seen there is a good agreement between both results. However, the SBR takes 12 hours, 12 minutes and 18 seconds, considering 10.000 ray tubes launched from the aperture (with a separation between points of a tenth of wavelength, that is to say, 100 points per square wavelength), while the interpolation method only requires 58 minutes and 47 seconds, because only 64 points are considered in the interpolation. It is important to notice that in this case the authors only try to prove that the computational cost is importantly reduced with the proposed method with respect to the SBR to obtain the same results. Logically, the diffraction should be included in both approaches to improve the results. The diffraction could be easily introduced in our approach considering the contribution of the second and third order critical points in the SPM formulation. The procedure would be identical to the one described in Section 2.

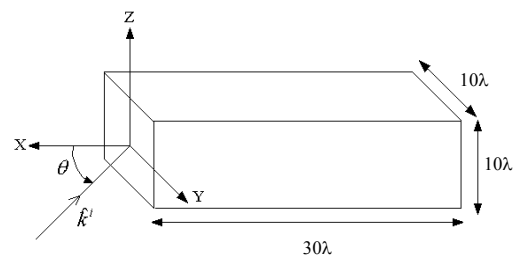


Fig. 12. Geometry of the rectangular cavity analyzed.

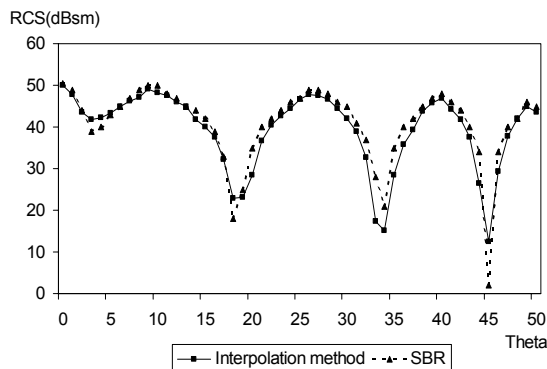


Fig. 13. Comparison between the results obtained by the interpolation method and the SBR for the monostatic RCS of the rectangular cavity.

VI. CONCLUSIONS

A method for obtaining higher order contributions to the electromagnetic scattered field by complex bodies has been developed. The method is based on the interpolation of the induced currents, by means of Bézier surfaces. For each current mode, it uses one Bézier surface to interpolate each component of the amplitude and another one to interpolate the phase. Once it has interpolated these induced currents, the scattered field is obtained by solving the PO integral using the SPM.

The method has several advantages over others currently being used to obtain these higher order contributions. The method can be used with all surfaces not only flat ones like the Image Method. The number of sampling points required to interpolate the current on a surface is very low compared to the number of rays the SBR uses to solve these kinds of problems. Finally, the advantage the proposed approach over ray-tracing inverse methods is that it only needs to minimize functions of two variables to find the ray-path, irrespectively of the order of the contribution. Whilst inverse methods need minimize functions of $2n$ variables, n being the order of the contribution, which means that the CPU-time needed for each minimization, increases exponentially with n .

The method developed is especially suitable for the analysis of problems where higher order contributions are of importance such as the propagation of tunnels or the computation of the RCS of cavities. An example of the last application has been shown in the Results section.

ACKNOWLEDGEMENTS

This work has been supported in part by Universidad de Alcalá, Project UAH PI2005/069.

REFERENCES

- [1] M.C.Lawton, and J.P.McGeehan, "The application of a deterministic ray launching algorithm for the prediction of radio channel characteristics in small-cell environments," *IEEE Transactions on Vehicular Technology*, vol 43, no. 4, November 1994, pp. 955-969.
- [2] S.Y.Tan, and H.S.Tan, "A microcellular communications propagation model based on the Uniform theory of Diffraction and Multiple Image Theory," *IEEE Transactions on Antennas and Propagation*, vol 44, No. 10, October 1996, pp. 1317-1326.
- [3] M. Domingo, R.P. Torres, and M.F. Cátedra, "Calculation of the RCS from the Interactions of Edges and Facets," *IEEE Transactions on Antennas and Propagation*, vol 42, no 6, June 1994, pp.885-890.
- [4] C.A. Balanis, *Advanced Engineering Electromagnetics*. John Wiley & Sons, New York, 1989.
- [5] H. Ling, R. Chou, and S.W. Lee, "Shooting and Bouncing Rays: Calculating the RCS of an Arbitrary Shaped Cavity," *IEEE Transactions on Antennas and Propagation*, vol. 37, February 1989, pp. 194-205.
- [6] S.W. Lee, H. Ling, and R. Chou, "Ray-Tube Integration in Shooting and Bouncing Ray Method," *Microwave & Optical Technology Letters*, vol. 1, no. 8, Aug. 1988, pp. 286-289.
- [7] S.K. Jeng, "Near-Field Scattering by Physical Theory of Diffraction and Shooting and Bouncing Rays," *IEEE Transactions on Antennas and Propagation*, vol. 46, no. 4, April 1998, pp. 551-558.
- [8] S.Y.Seidel, and T.S.Rappaport, "Site-Specific propagation prediction for wireless in building personal communication system design," *IEEE Transactions on Vehicular Technology*, vol. 43, no. 4, November 1994, pp.879-891.
- [9] H.T. Anastassiou, "A Review of Electromagnetic Scattering Analysis for Inlets, Cavities and Open Ducts," *IEEE Antennas and Propagation Magazine*, vol. 45, no 6, December 2003, pp. 27-40.
- [10] J. Pérez, F. Sáez de Adana, O. Gutiérrez, I. González, M.F. Cátedra, I. Montiel, and J. Guzmán, "FASANT: Fast Computer Tool for the Analysis of On-Board Antennas," *IEEE Antennas*

- and *Propagation Magazine*, vol. 41, no 2, April 1999, pp. 94-99.
- [11] M. F. Cátedra, J. Pérez, F. Sáez de Adana, and O. Gutiérrez, "Efficient ray-tracing techniques for 3D analysis of propagation in mobile communications. Application to picocell and microcell scenarios," *IEEE Antennas and Propagation Magazine*, vol. 40, no. 2, April 1998, pp. 15-28.
- [12] O.M. Conde, J. Pérez, and M. F. Cátedra, "Stationary Phase Method Application for the Analysis of Radiation of Complex 3-D Conducting Structures," *IEEE Transactions on Antennas & Propagation*, vol. 49, no. 5, pp. 724-731, May 2001.
- [13] G.E. Farin, *Curves and Surfaces for Computer Aided Geometric Design, A Practical Guide* 2nd edition, Academic Press Inc., London 1990.
- [14] C. de Boor, *A practical guide to splines*. Springer, Berlin, 1978.
- [15] O. Gutiérrez, F. Sáez de Adana, F. Rivas, I. González, and M. F. Cátedra, "Method to Interpolate Induced Currents with a Low Amount of Sample Points by Means of Bézier Surfaces," *Electronic Letters*, vol. 39, no. 2, pp. 177-178, January 2003.
- [16] D. S. Jones, and M. Kline, "Asymptotic Expansions of Multiple Integrals and the Method of the Stationary Phase," *Journal of Mathematical Physics*, Vol. 37, January 1957.
- [17] J. C. Cooke, "Stationary Phase in Two Dimensions," *IMA Journal of Applied Mathematics*, vol. 29, pp. 25-37, 1982.
- [18] F. Obelleiro-Basteiro, J.L. Rodriguez, and R.J. Burkholder, "An Iterative Physical Optics Approach for Analyzing the Electromagnetic Scattering by Large Open-Ended Cavities," *IEEE Transactions on Antennas and Propagation*, vol. 43, no. 4, April 1995, pp. 356-361.
- [19] K. Sarabandi, and D. Zahn, "Numerical Simulation of Scattering from Rough Surfaces Using an Iterative Physical Optics Approach," *IEEE Antennas and Propagation Society International Symposium, 1998*. 21-26 June 1998, volume 2, pp:1070 – 1073.
- [20] W.H. Press, B.P. Flannery, S.A. Teukolsky, and W.T. Vetterling, *Numerical Recipes*. Cambridge University Press, Cambridge (Gran Bretaña). 1987.
- [21] O.M. Conde, F. Saez de Adana, and M.F. Cátedra, "A Comparison Between Two High-Frequency Techniques Applied to the Analysis of On-Board Antennas," *Microwave & Optical Technology Letters*, Vol. 36, n° 5, pp. 415-417, March 2003.



Francisco Saez de Adana was born in Santander, Spain, in 1972. He received the BS, MS and PhD. degrees in Telecommunications Engineering from the University of Cantabria, Spain, in 1994, 1996 and 2000, respectively. Since 1998 he works at the University of Alcalá, first as assistant professor and since 2002 as professor. He has worked as faculty research at Arizona State University from March 2003 to August 2003.

He has participated in more than forty research projects with Spanish, European, American and Japanese companies and universities, related with analysis of on board antennas, radio propagation in mobile communication, RCS computation, etc. He has directed two Ph. D. Dissertations, has published thirteen papers in referred journals and more than 30 conference contributions at international symposia. His research interests are in areas of high-frequency methods in electromagnetic radiation and scattering, on-board antennas analysis, radio propagation on mobile communications and ray-tracing acceleration techniques.



Oscar Gutiérrez Blanco was born in Torrelavega, Spain, in 1970. He received the BS and MS degrees in Telecommunications Engineering from the University of Cantabria, Spain, in 1993 and 1996, respectively. From 1995 to 1998, he was with the Communications Engineering Department of the Cantabria as Research assistant. He received the Ph.D. degree in Telecommunication from the Alcalá university, Spain, in 2002. From 1998 to 2000, he was with the Signal Theory and communications Department of the Alcalá University, Madrid. In 2001, he is currently an assistant professor in the Computational Science Department in the Alcalá University, Madrid.

He has participated in more than 40 research projects, with Spanish and European companies, related with analysis of on board antennas, radio propagation in mobile communication, RCS computation, etc. His research interests are in high-frequency methods in electromagnetic radiation and scattering, and ray-tracing acceleration techniques.



Lorena Lozano was born in Madrid, Spain, in 1978. She received the BS and MS degrees in Telecommunications Engineering from the University of Alcalá in 2000 and 2002, respectively. She is currently pursuing the Ph.D. degree at the Computer Science Department, University of Alcalá, Spain.

She has been with the Signal Theory and Communications Department of the University of Alcalá since 1999 to 2004 and, since then, in the Computer Science Department of the University of Alcalá. From June 2004 to November 2004, she was with the Electrical Engineering Department of Arizona State University, as a research assistant. Her research interests are in areas of high-frequency methods in electromagnetic radiation and scattering, on-board antennas analysis, ray-tracing acceleration techniques, and RCS computation.



Manuel F. Catedra received his M.S. and Ph. D. degrees in Telecommunications Engineering from the Polytechnic University of Madrid (UPM) in 1977 and 1982 respectively. From 1976 to 1989 he was with the Radiocommunication and Signal Processing Department of the UPM. He has been Professor at the University of Cantabria from 1989 to 1998. He is currently Professor at the University of Alcalá, in Madrid, Spain.

He has worked on about 60 research projects solving problems of Electromagnetic Compatibility in Radio and Telecommunication Equipment, Antennas, Microwave Components and Radar Cross Section and Mobile Communications. He has developed and applied CAD tools for radio-equipment systems such as Navy-ships, aircraft, helicopters, satellites, the main contractors being Spanish or European Institutions such as EADS, ALCATEL, CNES, ALENIA, ESA, DASA, SAAB, INTA, BAZAN, INDRA, the Spanish Defence Department.

He has directed about 15 Ph D. dissertations, has published about 45 papers (IEEE, Electronic Letters, etc), two books, about 10 chapters in different books, has given short courses and has given around a hundred and thirty presentations in International Symposia.

The Use of Multiquadric Radial Basis Functions in Open Region Problems

Richard K. Gordon and W. Elliott Hutchcraft

Department of Electrical Engineering
University of Mississippi
University, MS 38677

Email: eeqordon@olemiss.edu, eweh@olemiss.edu

Abstract — With the advent of neural networks, there has been a significant amount of research utilizing radial basis functions. In this paper, radial basis functions in conjunction with a meshless algorithm are used to solve electromagnetics problems in both open and closed regions. The algorithm for the solution of partial differential equations using the radial basis functions and development of the absorbing boundary condition will be discussed in detail. Several example problems will be discussed.

Keywords — radial basis functions, meshless algorithms, absorbing boundary conditions, partial differential equation techniques

I. INTRODUCTION

Radial basis functions (RBF) have received significant attention in the scientific literature over the past several years. Specifically, they have been investigated heavily in the field of neural networks. Until rather recently, RBF's have not been widely used in computational electromagnetics. They have been shown to have very good interpolation qualities and this has led to their recent use in inverse scattering methods in electromagnetics [1-11]. In this paper, radial basis functions in conjunction with a meshless algorithm are used to solve electromagnetics problems in both open and closed regions. In the next section, a discussion of the method used to solve partial

differential equations (PDE) using RBF's will be presented and an example will be shown. In Section III, the development of an absorbing boundary condition (ABC) based on the Wilcox expansion of the electric field will be presented and results utilizing the ABC will be shown. Finally, section IV will conclude the paper with discussions of some of the advantages and disadvantages of the proposed method.

II. SOLUTION OF PARTIAL DIFFERENTIAL EQUATIONS USING RADIAL BASIS FUNCTIONS

There are several different RBF's that could be used to solve PDEs, but in this paper, the focus will be on the multiquadric functions. These functions have a function representation of

$$\sqrt{1 + \frac{\|x - x_j\|^2}{c_j^2}}. \quad (1)$$

These functions have several interesting properties. The function's magnitude depends primarily upon the radial distance from its central location, x_j . This results in each slice of the function having a circular cross-section. In addition, these functions are continuous and have an infinite number of continuous derivatives at all points in space.

The algorithm employed in solving the PDEs in this research is termed a "meshless" method. This term is derived from the fact that

only information about nodes has to be known; in other words, no connectivity data between nodes is required. This is in contrast to the finite element method (FEM), which requires the knowledge of how the nodes are connected into elements. Generating a mesh for a detailed problem can be quite cumbersome and a misconnected node, which can easily go unnoticed, could lead to major problems. Obviously, since this is not necessary in this meshless algorithm, some of the problems associated with meshing can be alleviated. To discuss the details of the proposed algorithm, consider the closed region problem described by

$$\begin{aligned} \nabla^2 E_z + k^2 E_z &= 0 \quad \text{for } (x, y) \in \Omega \\ E_z(x, y) &= f(x, y) \quad \text{for } (x, y) \in \partial\Omega. \end{aligned} \quad (2)$$

The problem domain along with the associated boundary conditions is illustrated in Fig. 1. The radial basis functions will be used as the expansion for the electric field such that

$$E_z = \sum_{j=1}^N u_j \sqrt{1 + \frac{(x-x_j)^2 + (y-y_j)^2}{c_j^2}}. \quad (3)$$

$$\begin{aligned} E_z(x, 1.0) &= \sin\left(\frac{3\pi x}{a}\right) \\ E_z(0.0, y) &= 0.0 \quad \varepsilon \quad E_z(2.0, y) = 0.0 \\ E_z(x, 0.0) &= 0.0 \end{aligned}$$

Fig. 1. Closed region problem domain.

Here, the u_j 's are the unknown coefficients. The factor, c_j , is a scale factor for each RBF. In this research, all of the c_j 's have been chosen to be equal to 0.25. Now, the expansion (3) can be substituted into the original PDE (2) to obtain

$$\begin{aligned} \nabla^2 \left[\sum_{j=1}^N u_j \sqrt{1 + \frac{(x-x_j)^2 + (y-y_j)^2}{c_j^2}} \right] + \\ k^2 \sum_{j=1}^N u_j \sqrt{1 + \frac{(x-x_j)^2 + (y-y_j)^2}{c_j^2}} = 0. \end{aligned} \quad (4)$$

At this point, there are N unknown coefficients (the u_j 's) and only one equation. N equations are necessary to solve for the N u_j 's. The method used to obtain the N equations is called collocation. Collocation enforces either (4), or the boundary conditions, at the central points of the N RBF's. This yields a matrix equation

$$Mu = b \quad (5)$$

in which the matrix, M , will have elements

$$M_{i,j} = \begin{bmatrix} \nabla^2 \sqrt{1 + \frac{(x_i-x_j)^2 + (y_i-y_j)^2}{c_j^2}} \\ +k^2 \sqrt{1 + \frac{(x_i-x_j)^2 + (y_i-y_j)^2}{c_j^2}} \end{bmatrix} \text{ for } (x_i, y_i) \text{ in } \Omega \quad (6)$$

or

$$M_{i,j} = \sqrt{1 + \frac{(x_i-x_j)^2 + (y_i-y_j)^2}{c_j^2}} \text{ for } (x_i, y_i) \text{ on } \partial\Omega. \quad (7)$$

The right-hand side vector will have elements

$$b_j = \begin{cases} 0 & \text{for } (x_i, y_i) \text{ in } \Omega \\ f(x_i, y_i) & \text{for } (x_i, y_i) \text{ on } \partial\Omega \end{cases} \quad (8)$$

and the column vector, u , will be the vector containing the coefficients for the RBF's.

To illustrate that accurate results can be obtained for the aforementioned problem, consider the case for which $\varepsilon = 25.0$ and $\lambda = \frac{2\pi}{k} = 1.0$. Plots of both the numerical and analytic solution along the line $y = 0.3$ (Fig. 2) and $x = 0.5$ (Fig. 3) illustrate the accuracy that can be obtained using this method.

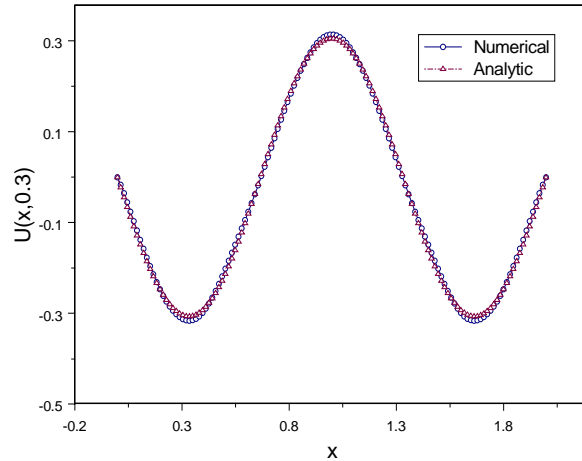


Fig. 2. Comparison of analytic and numerical solution (999 RBF's) along $y = 0$.

The solutions are obtained by employing 999 RBF's (33 equally spaced nodes along the x -direction and 33 equally spaced nodes along the y -direction) in the algorithm. In both cases, the numerical solutions lie nearly on top of the analytic solution.

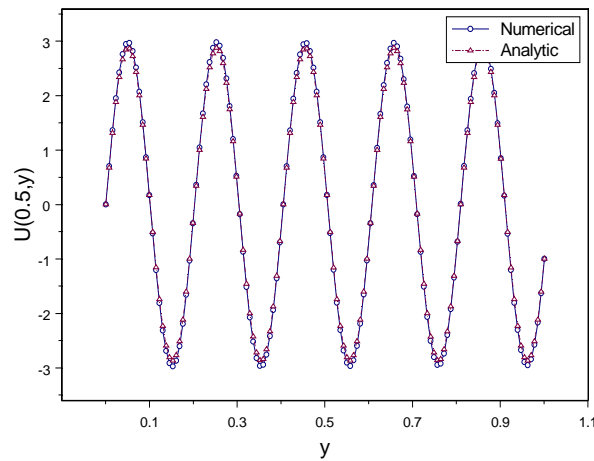


Fig. 3. Comparison of analytic and numerical solution (999 RBF's) along $x=0.5$.

This is rather impressive considering that there are only 33 basis functions in the y -direction and there are 5 wavelengths of variation in the y -direction. An investigation of the RMS Error as the number of RBF's is varied is shown in Fig.4.

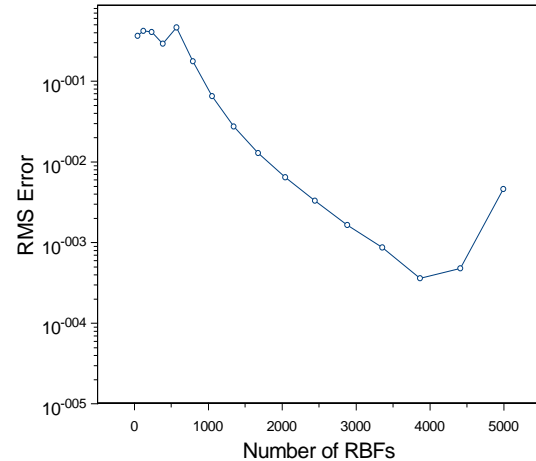


Fig. 4. RMS error as number of RBF's is varied.

This graph shows primarily what is expected. That is, as the number of RBF's is increased, the solution converges and the RMS error decreases. It should be pointed out that the computational cost of solving the matrix is higher than the traditional FEM for example, since the resulting matrix for this method is a full matrix. A direct solution technique (Gaussian elimination) was employed in the solution of the matrix equation. In addition to the disadvantage of having a full system matrix, the use of RBF's can result in ill-conditioning as the number of functions is increased. Ill-conditioning is primarily the problem for the increase in RMS error as the number of RBF's increases over 1000. A plot of the condition number as the number of RBF's is varied is shown in Fig. 5. It is important to realize that this graph is plotted on log axis; so, there are nearly 18 orders of magnitude difference between the smallest condition number and the largest condition number.

Further investigation of the condition number is required and some techniques to help alleviate the ill-conditioning will be presented in a separate paper. After seeing these results, though, it is clear that the RBF's

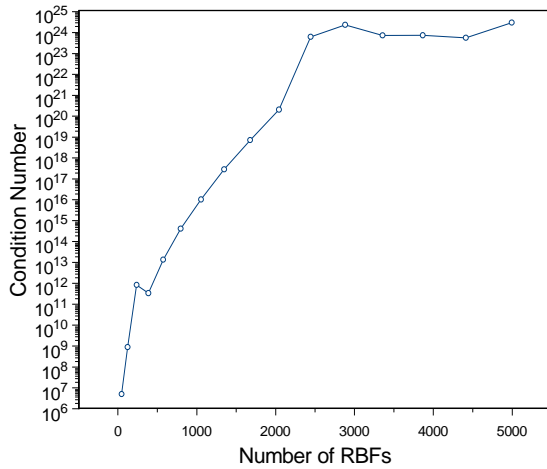


Fig. 5. Condition number as number of RBF's is varied.

can be used to solve closed region problems. In the next section, the focus will turn to that of the primary topic for this paper; that is, the discussion of the development of an ABC for an open region problem will be presented and then the ABC will be verified through several examples.

III. DEVELOPMENT OF AN ABSORBING BOUNDARY CONDITION FOR USE WITH RADIAL BASIS FUNCTIONS

Consider the scattering of a transverse magnetic (TM) incident plane wave on a cylinder of radius one wavelength as shown in Fig. 6. The nodes (central points) for the RBF's will be placed in the shaded region and along the inner and outer boundaries. The outer boundary will be placed 1.35 wavelengths away from the center of the perfect electrically conducting (PEC) cylinder. The equation enforced at collocation points that are between the PEC cylinder and the outer boundary is the Helmholtz equation

$$\nabla^2 E_z + k^2 E_z = 0. \quad (9)$$

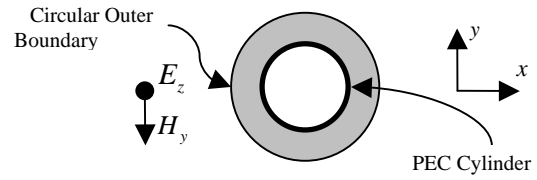


Fig. 6. Problem domain for circular PEC cylinder with circular outer boundary.

For collocation points that are on the circular cylinder, the equation enforced is

$$E_z = 0 \text{ for } r_i = \lambda \quad (10)$$

and for nodes along the outer boundary, the equation enforced will be

$$E_z(1.35, \phi) = AE_z(1.30, \phi) + BE_z(1.25, \phi). \quad (11)$$

There are several aspects that should be pointed out with respect to the implementation of the ABC. Equation (11) states that the electric field at the outer boundary is proportional to the electric field at two points that lie along the same phi plane and are 0.05 and 0.1 wavelengths interior to the outer boundary. The fact that $E_z(1.25, \phi)$ and $E_z(1.30, \phi)$ need to be known does not mean that nodes have to be placed at these locations. Since the RBF's are entire domain basis functions, a representation of E_z in terms of all of the RBF's can easily be found everywhere in the domain. Therefore, nodes are not necessary at $E_z(1.25, \phi)$ and $E_z(1.30, \phi)$. Obviously, the constants A and B in (11) must be obtained. It is first assumed that $E_z(1.25, \phi)$ and $E_z(1.30, \phi)$ can be approximated by the first two terms of the Wilcox expansion, which is

$$E_z(r, \phi) = \frac{e^{-jkr}}{\sqrt{r}} \left(C_1(\phi) + \frac{C_2(\phi)}{\rho} \right). \quad (12)$$

This assumption allows us to find C_1 and C_2 in terms of $E_z(1.25, \phi)$ and $E_z(1.30, \phi)$. Then, once these constants are known, the constants A and B can be found. After obtaining A and B , an expression for E_z along the outer boundary is known in terms of E_z at points slightly interior to the boundary. Now, by using equations (9), (10), and (11), a matrix equation can be formed and the coefficients for the RBF's can be obtained. The algorithm will initially be tested using 2636 RBF's. Since the region between the cylinder and the outer boundary has an area equal to 2.5 square wavelengths, this problem domain has been discretized to yield approximately 32 functions/wavelength. In Figs. 7 and 8, the numerical and analytic solutions for the magnitude and the phase of the electric surface current on the PEC cylinder are compared. With this mesh density, a nodal average percent error was calculated to be 1.46%.

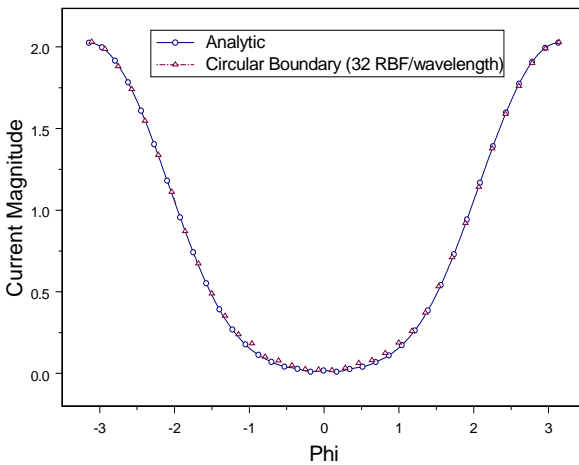


Fig. 7. Magnitude of the current along the cylinder (~ 32 RBF/wavelength).

Since 32 functions/wavelength is a rather high mesh density, the results of a simulation in which the mesh density was lowered to approximately 23 functions/wavelength (1416 nodes) are presented in Figs. 9 and 10. Even at this density, the average percentage error was still very low at only 1.6%. At this point,

the ABC has been verified to work properly for a circular outer boundary.

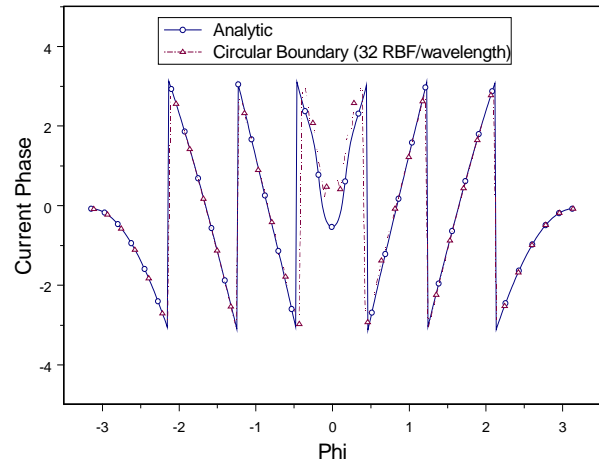


Fig. 8. Phase of the current along the cylinder (~ 32 RBF/wavelength).

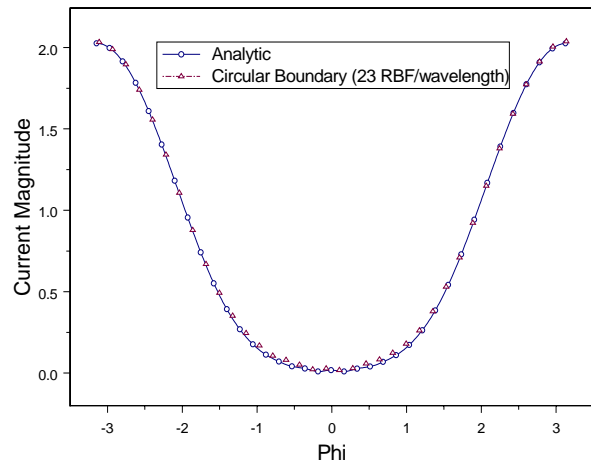


Fig. 9. Magnitude of the current along the cylinder (~ 23 RBF/wavelength).

However, one of the problems often encountered with ABCs is that special meshing is required at the boundary so that the ABC can be implemented. For example, this could include placing the nodes close to the edge of the outer boundary along a constant phi plane or having a circular boundary, etc. To illustrate the robustness of the developed ABC and show that it does not have this requirement, the same cylinder will be

considered, but the outer boundary will be changed from a circular outer boundary to a square outer boundary. An illustration of the problem domain is shown in Fig. 11.

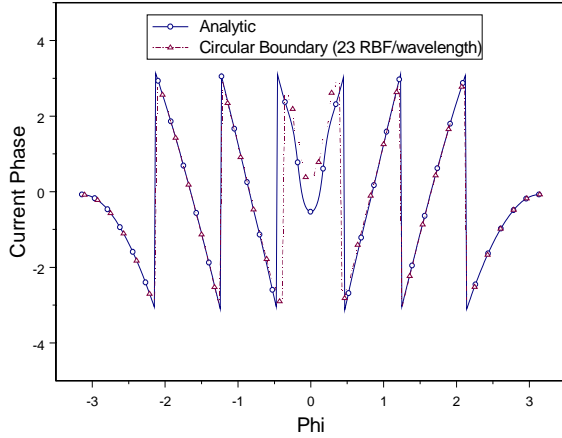


Fig. 10. Phase of the current along the cylinder (~23 RBF/wavelength).

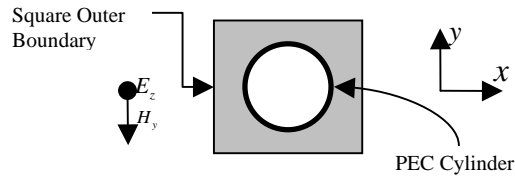


Fig. 11. Problem domain for circular PEC cylinder with circular outer boundary.

The center of each side of the square boundary will be tangent to the circular boundary from the previous example. Thus, the square’s sides will have lengths of 2.7 wavelengths and the region between the cylinder and outer boundary will have an area equal to 4.15 square wavelengths. A total of 2512 RBF’s were used in the simulation. This resulted in a mesh density of approximately 25 functions / wavelength. Comparisons of the numerical and analytic solutions for the magnitude and phase are presented in Figs. 12 and 13, respectively. The average percent error per node was 2.08%. From these graphs, one can conclude that switching from a

circular outer boundary to a square outer boundary did not significantly affect the results. This is particularly beneficial since it is desired to keep this method a “meshless” algorithm. We do not want to have to be very specific about where to put the RBF’s in the problem domain and we also do not want to specify a specific type of outer boundary.

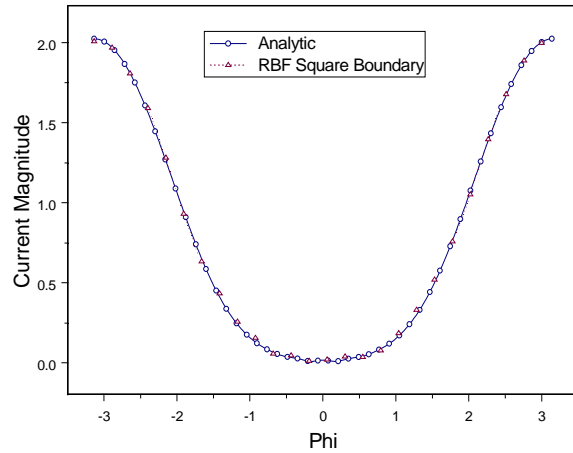


Fig. 12. Magnitude of the current along the cylinder (~25 RBF/wavelength) with square boundary.

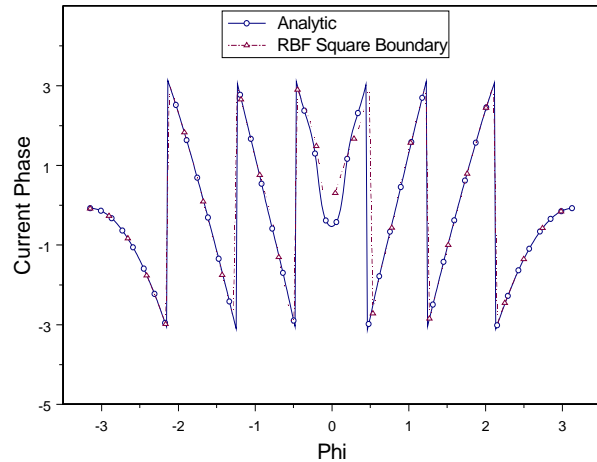


Fig. 13. Phase of the current along the cylinder (~25 RBF/wavelength) with square boundary.

IV. CONCLUSION

We have shown in this research a proof-of-

concept that a meshless method employing multiquadric radial basis functions and collocation can be used to obtain accurate results for both closed region and open region problems. Among the principle advantages of this method are the simplicity of the programming and the elimination of the need for sophisticated meshing. Among the disadvantages of this method is the fact that it yields a full matrix and that matrix can be ill-conditioned as the number of RBF's is increased. This problem is alleviated somewhat by the quickness of which each matrix element can be obtained. In addition, ill-conditioning can also result if care is not taken. Future research includes an investigation of the condition number and ways to prevent and alleviate the ill-conditioning problem that can result. Included in this investigation will be an investigation of node placement strategies as well as choice of the shape factor (c_{val}); in addition, future work will also investigate what happens with discontinuities in the problem domain and how they should be handled.

REFERENCES

- [1] M. J. F. A. I. Fedoseyev, E. J. Kansa, "Continuation for Nonlinear Elliptic Partial Differential Equations Discretized By The Multiquadric Method," *International Journal of Bifurcation and Chaos*, vol. 10, pp. 481-491, 2000.
- [2] S. C. E. Bermani, M. Raffetto, "A Threshold Electromagnetic classification approach for cylinders embedded in a lossy medium by using a neural network technique," *Microwave Opt. Technol Let*, vol. 24, pp. 13-16, 2000.
- [3] S. C. E. Bermani, M. Raffetto, "Microwave detection and dielectric characterization of cylindrical objects from amplitude-only data by means of neural networks," *IEEE Trans Antennas Propagat*, vol. 50, pp. 1309-1314, 2002.
- [4] L. U. I. Elshafiey, S. S. Udpa, "Solution of inverse problems in electromagnetics using hopfield neural networks," *IEEE Trans Magn*, vol. 31, pp. 852-861, 1995.
- [5] W. Y. Liu Guosui, Yang Chunling, Zhou Dequan, "Radar Target Classification Based on Radial Basis Function and Modified Radial Basis Function Networks," pp. 208-211.
- [6] K. A. M. R. Mydur, "A Neural-Network Approach to the Electromagnetic Imaging of Elliptic Conducting Cylinders," *Microwave Opt. Technol Let*, vol. 28, pp. 303-306, 2001.
- [7] I. T. Rekanos, "On-line inverse scattering of conducting cylinders using radial basis-function neural networks," *Microwave Opt. Technol Let*, vol. 28, pp. 378-380, 2001.
- [8] I. T. Rekanos, "Neural-network-based inverse-scattering technique for online microwave medical imaging," *IEEE Trans Magn*, vol. 38, pp. 1061-1064, 2002.
- [9] P. G. S. Caorsi, "Electromagnetic Detection of Dielectric Cylinders by a Neural Network Approach," *IEEE Trans Geosci Remote Sensing*, vol. 37, pp. 820-827, 1999.
- [10] H. H. S. Ratnajeevan, "Artificial Neural Networks in the Solution of Inverse Electromagnetic Field Problems," *IEEE Trans Magn*, vol. 29, pp. 1931-1934, 1993.
- [11] F. N. C. S. Chen, P. M. Grant, "Orthogonal least squares learning algorithm for radial basis function networks," *IEEE Trans Neural Networks*, vol. 2, pp. 302-309, 1991.



Richard K. Gordon was born in Birmingham, Alabama on November 26, 1959. He earned his B.S. in physics at Birmingham Southern College, Birmingham, AL in 1983, his M.S. in mathematics at the University of Illinois,

Urbana, IL in 1986 and his Ph. D. in electrical engineering at the University of Illinois, Urbana, IL in 1990.

He is an Associate Professor in the Department of Electrical Engineering at the University of Mississippi in Oxford, Mississippi.

Dr. Gordon is a member of Eta Kappa Nu, Phi Beta Kappa, and Tau Beta Pi.



W. Elliott Hutchcraft was born in Lexington, Kentucky on April 29, 1973. He earned his B.S. in electrical engineering at the University of Mississippi, Oxford, MS in 1996, his M.S. in electrical engineering at the

University of Mississippi, Oxford, MS in 1998 and his Ph. D. in electrical engineering at the University of Mississippi, Oxford, MS in 2003.

He is an Assistant Professor in the Department of Electrical Engineering at the University of Mississippi in Oxford, Mississippi.

Dr. Hutchcraft is a member of Eta Kappa Nu, Sigma Xi, IEEE, Tau Beta Pi, Phi Kappa Phi, and ARFTG.

A Novel Dual-band Small Size Microstrip Antenna

Abdel Fattah Sheta¹, Hoda Boghdady², Ashraf Mohra³
and Samir F. Mahmoud⁴

^{1,3} EE Dept. King Saud University, P. O.Box 800, Riyadh 11421, Saudi Arabia

² Transmission Dept., NTI, 11768, Cairo, Egypt

⁴ EE Dept., Kuwait University, P. O.Box 5969, Safat 13060, Kuwait

Abstract – A new small size dual-band microstrip antenna structure is proposed. The antenna consists of two resonant elements designed separately and integrated in such a manner to improve the compactness of the dual band structure and maintain the performance of each element. The structure is analyzed using lumped element approach and design curves are produced. The proposed approach is validated through a design example using theoretical curves and simulations. Implementation of an antenna operating in the 900 MHz and 1800 MHz bands is presented and comparisons between simulated and experimental results are given.

I. INTRODUCTION

In many regions over the world the two operating frequency systems, GSM system operating at 900 MHz, and the DCS 1800 at 1800 MHz, are simultaneously used for mobile communications. Therefore, the design of dual-band antennas for mobile handset applications has received much attention. Beside its dual-band operation, the antenna should also be small in size and excited by a single feed to meet the handset requirements. Due to their inherent flexibility, planar antennas are the most appropriate candidates to achieve these requirements. Recently, various types of planar inverted-F antennas (PIFAs) have been proposed for such applications [1]-[7]. Most of the previous works were based on simulator packages that use finite-difference time-domain (FDTD) or the method of moment. In this case the selection of the antenna dimensions for dual band operation becomes a tedious job.

In this paper, we propose a compact, dual band microstrip antenna that consists of two resonant elements. Each element can be designed separately at a specified center frequency and both elements integrated in such a way to maintain matching at the two frequencies, to have a compact structure and to provide negligible effect on each other. Each element consists of a short-circuited narrow line connected to a wider open circuited line as shown in Fig. 1. The lower frequency element (Fig. 1a) is a T-shaped patch and the high frequency element is an L-shaped patch (Fig. 1b). Both elements have a short circuited pin at the end of the narrow arm. The integrated dual band antenna is shown in Fig. 1c. The lumped

element model extracted from the transmission line theory is used to predict the resonant frequency of each element. The lumped element equivalence of the antenna elements is described in the next section where design curves are introduced. Discontinuities effects are explained in Section 3. In Section 4, we introduce specific design cases and conclusions are given in Section 5.

II. LUMPED ELEMENT EQUIVALENCE OF THE PROPOSED ANTENNA ELEMENTS

The simplest microstrip resonator is a half wavelength line opened at both ends, or a quarter wavelength line opened at one end and short-circuited at the other. Unfortunately, the size of an antenna based even on a quarter wavelength line is physically too large to be used for handset GSM applications. For this reason, a shaped short circuit resonator such as short circuited H-structure [8] or T-structure [9], which is considered as half of an open H-shaped antenna [10], has been developed as a compact antenna for single frequency operation. The H-shaped antenna has been analyzed using FDTD method, while the T-shaped one has been analyzed using the magnetic wall concept and transmission line theory.

The proposed dual-band antenna is shown in Fig. 1c and consists of two elements: a T-element that resonates at the lower frequency (Fig. 1a) and an L-element that resonates at the higher frequency (Fig. 1b). The transmission line equivalence of the short-circuited resonator elements in Figs. 1a and 1b are shown in Figs. 2a and 2b, respectively. For the T-shaped element, θ_1 and θ_2 are the effective electrical lengths of the lines of physical lengths l_1 and l_2 , respectively, after including the discontinuity effects. Z_1 and Z_2 are the characteristic impedances of the microstrip lines of widths W_1 and W_2 , respectively. These transmission lines can be represented by the lumped elements L and C as shown in Fig. 2c. For the T-shaped element (Fig. 1a) the short circuited line is equivalent to a lumped inductance given by:

$$\omega L = Z_1 \tan \theta_1 \quad (1)$$

where $\theta_1 = \omega l_1 / v_{ph1}$, v_{ph1} and Z_1 are the phase velocity and characteristic impedance of a microstrip line of width W_1 and effective length l_1 . The capacitance of the two parallel

open lines is related to their physical dimensions by

$$\omega C = 2 Y_2 \tan \theta_2 \quad (2)$$

where $\theta_2 = \omega l_2 / v_{ph2}$, v_{ph2} and Y_2 are the phase velocity and characteristic admittance ($1/Z_2$) of a microstrip line of width W_2 and effective length l_2 . Now combining (1) and (2) at the resonant frequency $\omega = \omega_0 = 1/\sqrt{LC}$, we get

$$2 \tan \theta_1 \tan \theta_2 = K \quad (3)$$

where K is the ratio of the line impedances; $K = Z_2 / Z_1$. Using (3), θ_2 is plotted against θ_1 for different values of K in Fig. 3a. It is observed that for a given value of θ_1 , θ_2 decreases with decrease of K resulting in a reduction of the total antenna size.

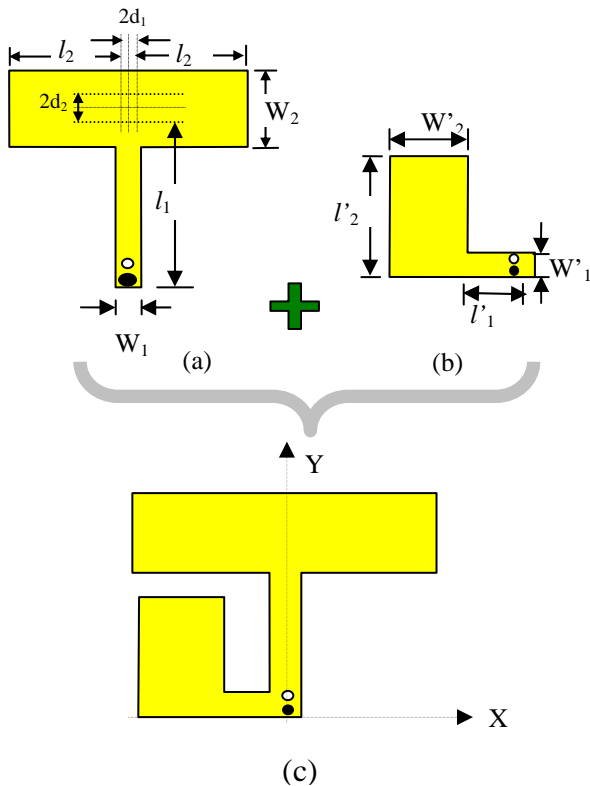


Fig. 1. a) T-shaped antenna operates at the lower frequency, b) L-shaped antenna operates at the higher frequency, and c) Geometry of the proposed dual band antenna.

Similar analysis can be carried out for the L-shaped element. So let us denote by θ'_1 and θ'_2 the effective electrical lengths of the lines l'_1 and l'_2 , respectively. Z'_1 and Z'_2 are the characteristic impedances of the microstrip lines of widths W'_1 and W'_2 , respectively. Following the same steps as for the T-shaped element, at resonance we get:

$$\tan \theta'_1 \tan \theta'_2 = K \quad (4)$$

In this case K is equal to Z'_2/Z'_1 . The design curves for this antenna are drawn in Fig. 3b for the same values of K as in Fig. 3a.

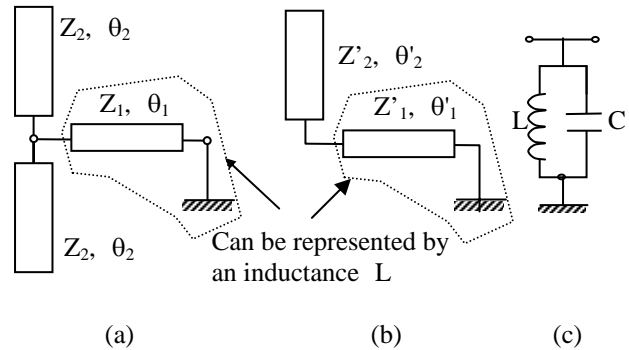


Fig. 2. a) Transmission line equivalence of antenna of Fig. 1a, b) Transmission line equivalence of antenna of Fig. 1b, and c) Lumped element equivalence of the resonators in Fig. 2(a) or 2(b).

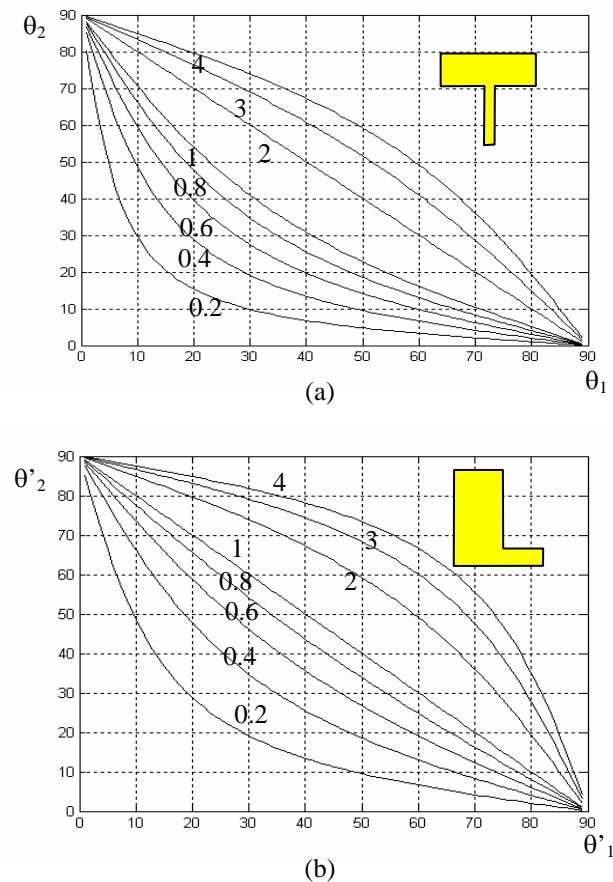


Fig. 3. θ_1 versus θ_2 for different values of K . a) T-shaped antenna, and b) L-Shaped antenna.

In this case the total electrical length of the antenna is given by $\theta'_t = \theta'_1 + \theta'_2$. It is noted that for $K = 1$ (uniform resonator), the total electrical length is 90° while the total length decreases as K decreases.

Figs. 3a and 3b, which determine the electrical lengths of the antenna arms, are helpful for a primary design of the T and L shaped elements through judicious selection of the K factors. The antenna physical dimensions l_1 , l_2 , W_1 , and W_2 (primed and unprimed) can then be calculated for specific frequencies of operation as will be described in the next section.

III. CIRCUIT LAYOUT

The circuit layout shown in Fig. 1, is the result of the conversion of the design parameters Z_1 , θ_1 , Z_2 , θ_2 , Z'_1 , θ'_1 , Z'_2 , and θ'_2 , to a physical dimensions W_1 , l_1 , W_2 , l_2 , W'_1 , l'_1 , W'_2 , and l'_2 in a selected substrate material at a design frequency. However, for wide bandwidth requirements, microstrip antennas are usually implemented on a thick air substrate. In this case, the required discontinuities in the structure significantly affect the resonance frequency of the antenna. Microstrip discontinuity can be represented as an equivalent circuit at some point in the transmission line. The component values, of the equivalent circuit, depend on the parameter of the line and the discontinuity as well as the frequency of operation. In some cases the equivalent circuit involves a shift in the phase reference planes on the transmission lines [11]. One approach for eliminating the discontinuity effect is to construct an equivalent circuit, including it in the design of the circuit, and compensating for its effect by adjusting other circuit parameters. In our case, the effects will be compensated in the lengths of the lines using either closed form expressions or through the aid of the IE3D simulator. The main discontinuities that exist in the proposed structure are the open end, T-junction, shorting post, and the bend.

Open end

An empirical expression for the open-end effect is given in [12, Eq. 1]. It can be used to calculate the equivalent additional line length Δl_{oc} .

Tee junction

The more useful representation of the Tee junction, for the design procedure, is to define the shift in reference planes as shown in Fig. 1a. The reference planes parameters d_1 , and d_2 can be calculated in terms of the substrate parameters and the lines widths W_1 , and W_2 from semi-empirical expressions given in [13, p. 245].

Shorting post

The shorting post is usually characterized by its equivalent inductance. This definition is not suitable to be incorporated in microstrip antenna design since the

resonance frequency is highly dependent of the location of the post. For this reason the shorting post is studied and compensated using the IE3D simulator. This can be achieved, first, by calculating the phase angle of S_{11} of a short circuit line of characteristic impedance Z_1 and electrical length θ_1 from

$$\text{Ang}(S_{11})\Big|_{sc} = 180 - 2 \tan^{-1}\left(\frac{Z_1 \tan \theta_1}{50}\right). \quad (5)$$

After that, an equivalent line of width W and length l terminated by a shorting post can easily be calculated with the optimization procedure tool of the IE3D. The optimization objective in this case is to match the theoretical angle from Eq. (5) to the angle of S_{11} of the physical length l at the design frequency.

Bend

The bend is usually modeled in terms of its equivalent circuit [11], which is not easy to compensate for in the lines lengths. However, it is easy to compensate for the bend and the open end, simultaneously, of the L-shape through the optimization tool of the IE3D. This can easily be performed by equating the phase angle of S_{11} of the open circuit layout in Fig. 4c to the theoretical angle of the open circuited line given by

$$\text{Ang}(S_{11})\Big|_{oc} = -180 + 2 \tan^{-1}\left(\frac{Z'_2 \cot \theta'_2}{50}\right). \quad (6)$$

For thin conventional dielectric materials, where, $2 < \epsilon_r < 10$ and thickness $0.5 < h < 2$ mm, the use of closed form expressions [11-13] for most of the microstrip discontinuities below 10 GHz leads to very good results.

IV. DESIGN CASE

The design approach described in the previous section is now validated through the design of an antenna that operates in the 900/1800 MHz bands. An air substrate of thickness 6.4 mm is used. Considering the T-shaped element, the thin line width W_1 is selected to be 2 mm. This small value helps to reduce any parasitic loading between the T and L elements after their integration. The resultant characteristic impedance of this line is $Z_1 = 193 \Omega$. Now, if we take the impedance ratio $K = 0.6$, the characteristic impedance of the wide line, Z_2 will be 115.8Ω , corresponding to about 7.7 mm line width W_2 . Fig. 3a is now used to compromise between θ_1 and θ_2 . Taking $\theta_1 = 25^\circ$, θ_2 is 32.8° . A probe feed of radius 0.5 mm is located close to the shorting post of radius 0.3 mm. For ideal lines with no discontinuity effects, the physical lengths of this element calculated at 900 MHz correspond to 25° and 32.8° would be 23.2 mm and 30.4 mm,

respectively. The physical dimensions shown in Fig. 1a are calculated as follows:

$$\Delta l_{oc} = 3.1 \text{ mm [12, Eq. 1].}$$

d_1 and d_2 are computed as 0.4 mm and 3.2 mm, respectively by use of [13, p. 245], while $l_2 = 30.4 - 3.1 = 27.3$ mm.

l_1 is obtained from the IE3D to match the theoretical phase angle of S_{11} , calculated from Eq. (5) as 58.1° , to the angle of the line terminated by a shorting post of radius 0.3 mm located as shown in Fig. 4a. The optimum length for l_1 is 19.4 mm. This means that, the effect of the shorting post at this position is equivalent to a line of the same width 2 mm and 3.8 mm length at 900 MHz.

The simulated resonance frequency corresponding to these dimensions is 935 MHz. This little variation is due to the neglect of feeder effect and the accuracy of the model used to calculate the reference planes. Slight increase of l_1 to 19.7 mm and l_2 to 28.6 mm reduces the resonance frequency to 908 MHz. In order to do a further reduction of the area occupied, the right arm of the T element is bent parallel to the narrow arm as shown in the inset of Fig. 5a. The effect of the bend is accounted for by using the simulator, and the simulation results of $|S_{11}|$ are given in Fig. 5a. The resonant frequency of the T-shaped element is 908 MHz and the bandwidth, corresponding to a 10 dB return loss, is 8 MHz.

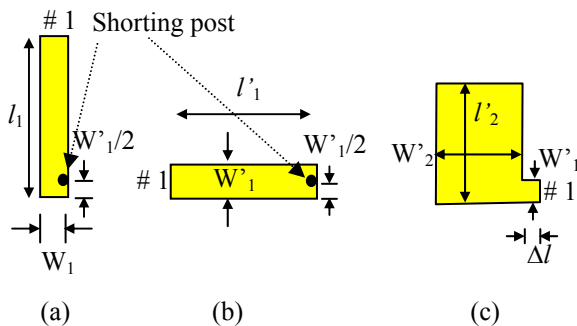
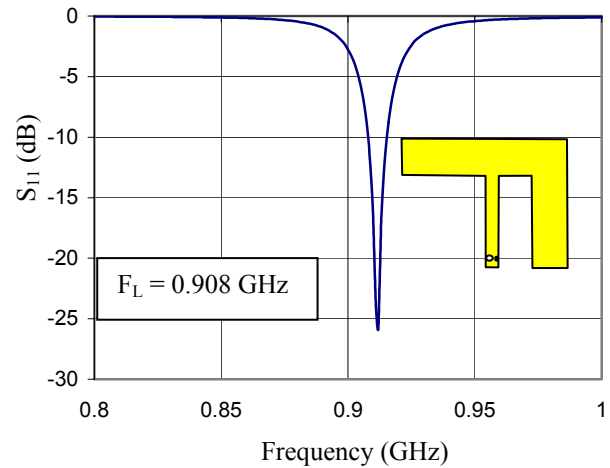


Fig. 4. Circuit layout elements to calculate discontinuities effect (a) the shoring post for the T-shaped at 900 MHz, (b) the shoring post of the L-shaped at 1800 MHz, and (c) the bend and open circuit effect of the L-shaped at 1800 MHz.

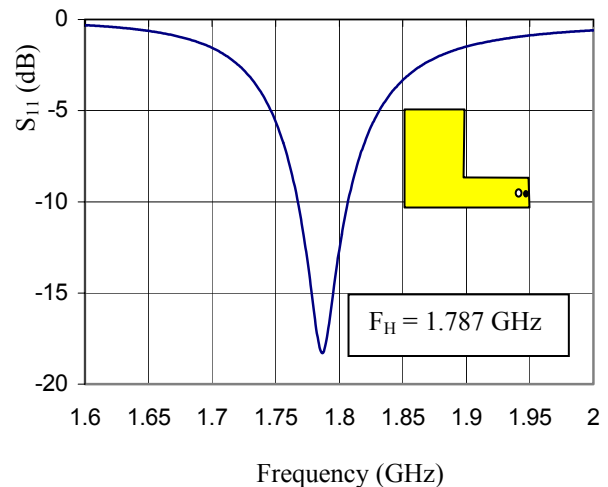
Similar steps are used to design the L-shaped antenna element at 1800 MHz. The narrower line width is selected to be $W'_1 = 3$ mm which corresponds to a characteristic impedance of 169Ω . Taking the impedance ratio $K = 0.5$, the characteristic impedance of the wider line is 84.5Ω which requires a line width of 14 mm. Taking $\theta'_1 = 28^\circ$ in Fig. 3b, θ'_2 is 43° . For ideal transmission line elements,

the physical lengths would be 13 mm, and 19.9 mm for narrow and wide lines, respectively. The physical dimensions of the L-shaped circuit layout shown in Fig. 1b are calculated as follow:

The length of the narrow line ended by a shorting post of 0.3 mm radius, shown in Fig. 4b, is calculated by equating the phase angle of S_{11} from the IE3D with the theoretical value from Eq. (5) for Z'_1 and θ'_1 at 1800 MHz. The resultant l'_1 is 6.5 mm. This means that the shorting post at this position is equivalent to a line of 3mm width and 6.5 mm length.



(a)



(b)

Fig. 5. Simulated S_{11} of the separate T and L shaped elements designed on air substrate of 6.4 mm thickness, a) Simulation results of the T-shape element designed at 900 MHz, and b) Simulation results of the L-shape element designed at 1800 MHz.

The bend is then calculated by the help of the optimization procedure of the IE3D as described in the previous section. The theoretical angle of the open circuited line from Eq. (6) is -57.8° . The circuit layout proposed is shown in Fig. 4c. The short length Δl is chosen to be 1.8 mm. The optimum value of the length l_2 to match this angle is 11.5 mm. The simulated resonance frequency obtained based on these dimensions is 1870 MHz. The shift in the resonance frequency is due to the feeder effect. This can be simply modified by little increase in any length of the circuit. For $l_2 = 15.4$ mm the simulated resonance frequency becomes 1787 MHz. The simulation results for the L-shaped element are shown in Fig. 5b where the 10 dB return loss bandwidth is 40 MHz at the center frequency.

Integration of the dual band antenna: Now the two elements are integrated as in Fig. 1c, while maintaining the same shorting post and feeder locations. The simulation results of the integrated structure are shown in Fig. 6. The lower band and upper band resonance occur now at $f_L = 907$ MHz and $f_H = 1835$ MHz with bandwidths of 8 MHz and 24 MHz respectively. It is thus seen that while the integration has almost no effect on the center frequency and bandwidth at the lower band, it caused an increase of the resonant frequency at the higher band by about 48 MHz, and a reduction in the bandwidth from 40 MHz to 24 MHz. We attribute this frequency shift and bandwidth reduction to the parasitic loading of the T- element on the L-element at the higher band. The simulated radiation patterns at the two resonant frequencies are plotted in Figs. 7 and 8. Both show an approximate omnidirectional radiation in the azimuth plane (x-z plane).

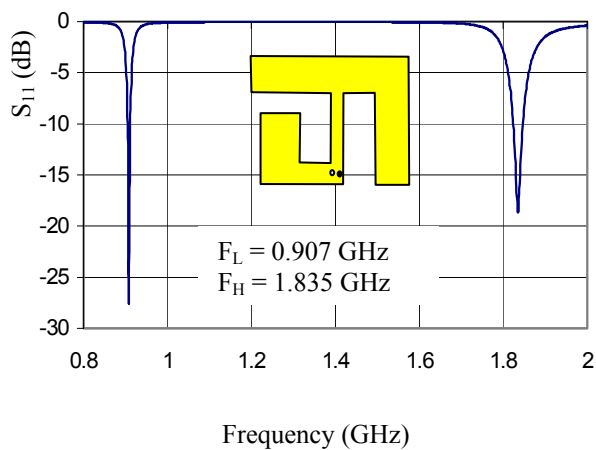


Fig. 6. Simulated S_{11} of the integrated T and L shaped elements in Figs. 5a and 5b.

The antenna gain is computed to be about -0.15 dBi and 1.5 dBi for the lower and upper resonant frequencies, respectively. Such relatively low gains are typical for compact antennas [6], [14]. We note that the antenna efficiency at the lower band is about 70%, so while the gain is -0.15 dBi the antenna directivity is equal to 1.8 dBi.

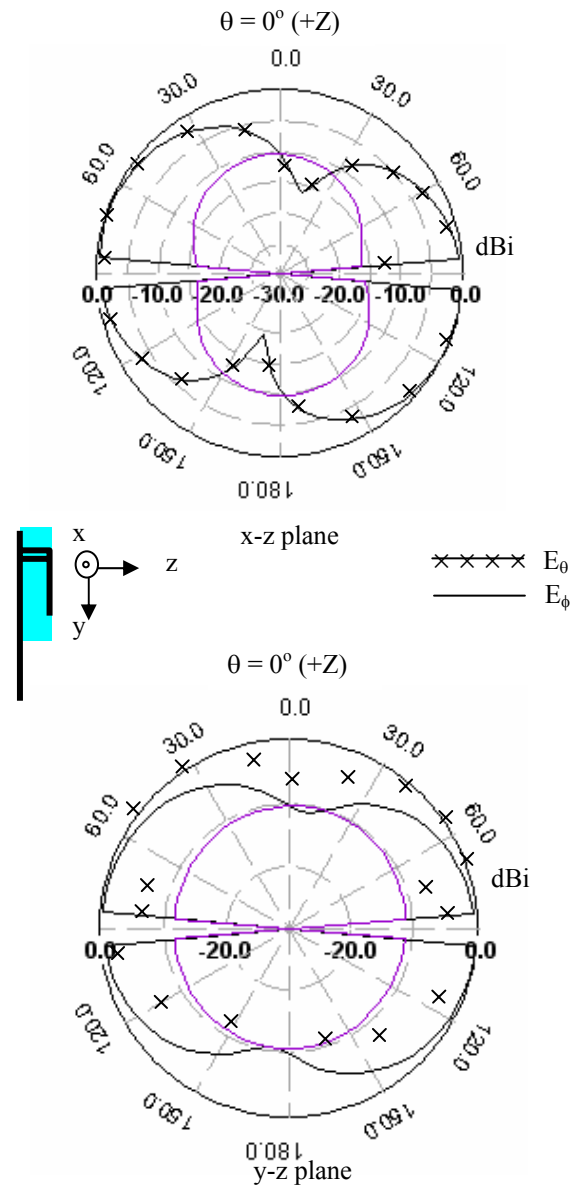


Fig. 7. Simulated radiation patterns at 907 MHz for the antenna in Fig. 5a.

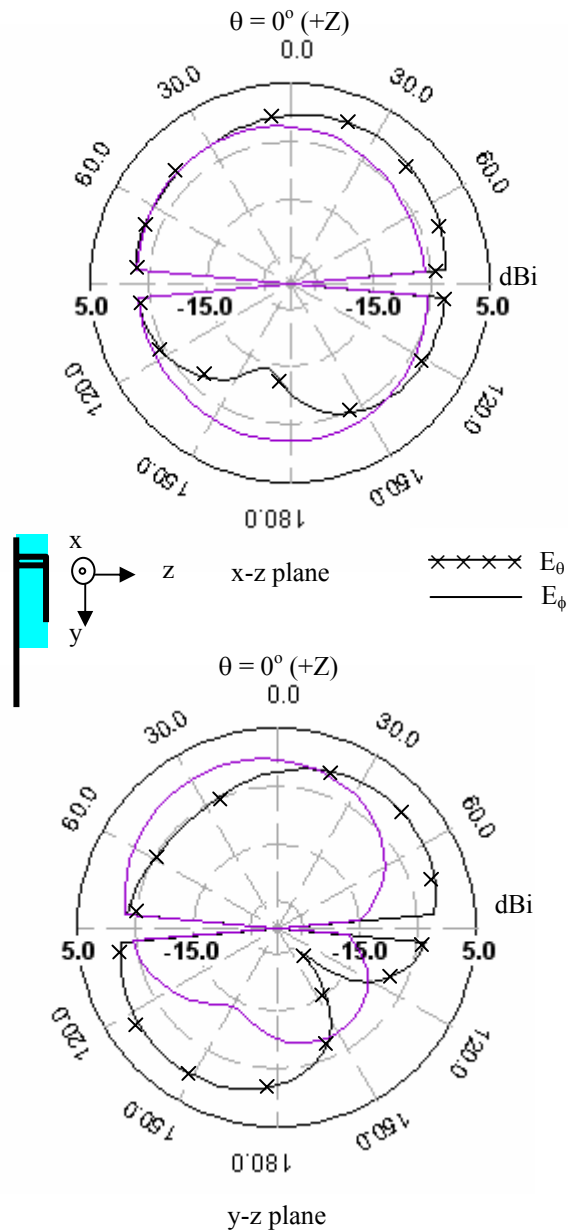


Fig. 8. Simulated radiation patterns at 1835 MHz for the antenna in Fig. 5a.

Experimental work: The dual band antenna is built on a foam substrate with dielectric constant close to that of air. The ground plane used is a copper plate of dimensions $64 \times 47 \text{ mm}^2$. The experimental results are shown in Fig. 9. The measured bandwidths based on 10 dB return loss, are about 12 and 31 MHz (compared to 8 MHz and 24 MHz from simulations) centered at 870 MHz and 1756 MHz, respectively. The observed change of the center frequencies and bandwidths from the simulation results

may be attributed to the inaccurate tools used for installing the feeder and short circuit. Simulations have shown that the resonance frequencies and bandwidths are sensitive to the locations of the short circuit and the feed. In addition, extra losses in the experiment, due to dielectric loss and finite ground plane, may be responsible for the increased experimental bandwidths compared to the simulation results.

Finally, to appreciate the size reduction achieved, we note that the built antenna occupies a volume of $27 \times 44 \times 6.4 \text{ mm}^3$ and mounted on a ground plane of $64 \times 47 \text{ mm}^2$. In terms of the wavelength at 1800 MHz ($\lambda = 166 \text{ mm}$), the antenna volume is about $0.16\lambda \times 0.26\lambda \times 0.04\lambda$ which makes it quite compact.

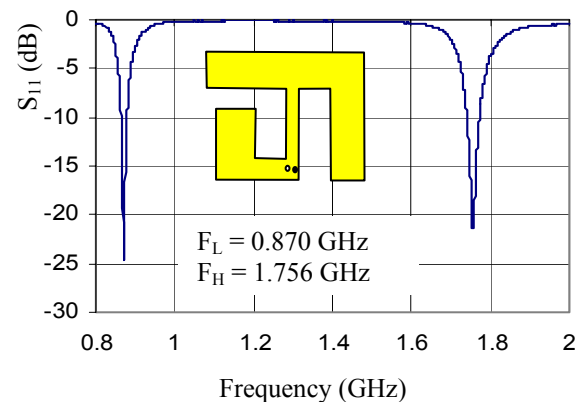


Fig. 9. Measured S_{11} of the integrated T and L shaped elements in Figs. 5a and 5b.

V. CONCLUSION

A new small size dual-band antenna structure has been proposed. Namely a T-patch antenna element tuned at 900 MHz is integrated with an L-patch tuned at 1800 MHz. A simple design procedure based on lumped element representation is used to obtain design equations and curves that are used for a preliminary design. The design is trimmed by using the IE3D simulation tool to account for the end and bend effects. Simulation results show the feasibility of achieving a compact dual band antenna occupying a volume of $0.16\lambda \times 0.26\lambda \times 0.04\lambda$, where λ is the wavelength at the upper band (1800 MHz). The simulation results are validated by building and testing an antenna prototype. Experimental and simulation results show reasonable agreement in terms of the center frequencies and bandwidths.

REFERENCES

- [1] Z. D. Liu, P. S. Hall, and D. Wake, "Dual-frequency planar inverted F antenna," *IEEE Trans. Antennas Propagat.*, vol. 45, pp. 1451–1458, Oct. 1997.
- [2] C. R. Rowell, and R. D. Murch, "A compact PIFA suitable for dual-frequency 900/1800-MHz operation," *IEEE Trans. Antennas Propagat.*, vol. 46, pp. 596–598, April 1998.
- [3] S. Tarvas, and A. Isohatala, "An internal dual-band mobile phone antenna," *Proc. IEEE AP-Symp.*, pp. 266–269, 2000.
- [4] P. Salonen, M. Keskilammi, and M. Kivikoski, "Single-feed dual-band planar inverted-F antenna with U-shaped slot," *IEEE Trans. Antennas Propagat.*, vol. 48, pp. 1262–1267, August 1998.
- [5] G. H. K. Lui, and R. D. Murch, "Compact dual-frequency PIFA designs using LC resonators," *IEEE Trans. Antennas Propagat.*, vol. 49, pp. 1016–1019, July 2001.
- [6] F. R. Hsiao, H. T. Chen, G. Y. Lee, T. W. Chiou, and K. L. Wong, "A dual-band planar inverted-F patch antenna with a branch-line slit," *Microwave Opt. Technol. Lett.*, vol. 32, pp. 310–312, Feb. 2002.
- [7] C. W. Chiu, and F. L. Lin, "Compact dual-band PIFA with multi-resonators," *Electron. Letters*, vol. 38, no. 12, pp. 538–539, 2002.
- [8] D. Singh C. Kallialakis, P. Gardner, and P. S. Hall, "Small H-shaped antennas for MMIC applications," *IEEE Trans. Antennas and Propagat.* vol. 48, pp. 1134–1140, July 2000.
- [9] A. Mohra, A. F. Sheta, and S. F. Mahmoud, "Analysis and design of small size short circuited microstrip T-shaped antenna," *Proc. of 20th National Radio Science Conference*, B18, Cairo, Egypt, 2003.
- [10] A.F Sheta, A. Mohra, and S. F. Mahmoud, "Multi-band operation of compact H-shaped microstrip patch antenna," *Microwave. Optical Tech. Letters*, vol. 35, pp. 363–367, Dec. 2002.
- [11] B. C. Wadell, *Transmission Line Design Handbook*, Artech House, Norwood, MA, 1991.
- [12] M. R. Kirschning, R. H. Jansen, and N. H. L. Koster, "Accurate model for open end effect of microstrip lines," *Electron Lett.*, Vol. 17, pp. 123–125, 1981.
- [13] T.C. Edwards, and M. B. Steer, *Foundations of Interconnect and Microstrip Design*, John Wiley & Sons, 2000.
- [14] S.F. Mahmoud, and R. K. Deeb, "Characteristics of a circular microstrip patch antenna with a shorting post," *Journal of Electromagnetic Wave Applications*, vol. 16, Feb. 2002.



Abdel fattah sheta received B.S. degree in Communications and Electro - Physics from Alexandria University, Egypt in 1985. He obtained his M.S. degree in Electrical Engineering Department, Cairo University, in 1991. In 1996, he received the Ph.D degree in microwave circuits analysis and design from ENST, Université de Bretagne Occidentale, France. During 1996-1998, he worked as a researcher in the National Telecommunication Institute, Cairo, Egypt. In 1998 he joined Electric Engineering Department, Cairo University, Fayoum Branch. Currently he is an associate Prof. In Electrical Engineering at King Saud University, Saudi Arabia. His current research interests include microstrip antennas, planar and uniplanar MIC's and MMIC's.



Hoda Boghdady graduated from Electronics and Communication Engineering Dept., Cairo University, Egypt in 1983, obtained M.Sc. from Cairo University, Egypt and Ph.D. from North Carolina State University, USA, in 1987 and 1993 respectively. Currently, Deputy Head of the Transmission Dept. at the National Telecommunication Institute in Egypt. Current research interests: microstrip antennas, CAD for planar microwave circuits



Ashraf S. Mohra graduated from the Electronics and Comm. Engineering Dept., Zagazig University, Egypt in 1986. He received the M.Sc. and Ph.D degrees in Electronics and Comm. Department, Ain Shams University, Cairo, Egypt, in 1994 and 2000, respectively. During 1989-2000 he was a researcher in microstrip Department at Electronics Research Institute, Egypt. He worked as a visiting prof., Mansoura University (2000-2002) and Akhbar El-Yom Academy (2003-2005). He was promoted to Associate Prof. in 2005. Currently he works in the Electrical Engineering Department at King Saud University, Saudi Arabia. His current research interests include microstrip antennas, hybrid junctions, computer aided design of planar and uniplanar of MIC's and MMIC's.



Samir F. Mahmoud graduated from the Electronic Engineering Dept., Cairo university, Egypt in 1964. He received the M.Sc and Ph.D. degrees in the Electrical Engineering Department, Queen's university, Kingston, Ontario, Canada in 1970 and 1973. During the academic year 1973-1974, he was a visiting research fellow at the Cooperative Institute for Research in Environmental Sciences (CIRES). Boulder, CO, doing research on Communication in Tunnels. He spent two sabbatical years, 1980-1982, between Queen Mary College, London and the British Aerospace, Stevenage, where he was involved in design of antennas for satellite communication. Currently Dr. Mahmoud is a full professor at the EE Department, Kuwait University. Recently, he has visited several places including Interuniversity Micro-Electronics Centre (IMEC), Leuven, Belgium and spent a sabbatical leave at Queen's University and the royal Military College, Kingston, Ontario, Canada in 2001-2002. His research activities have been in the areas of antennas, geophysics, tunnel communication, e.m wave interaction with composite materials and microwave integrated circuits. He is the author of "Electromagnetic Waveguides; theory and applications", IEE Electromagnetic series, vol. 32. Dr. Mahmoud is a Fellow of IEE and one of the recipients of the best IEEE/MTT paper for 2003.

An Efficient Broadband Analysis of an Antenna via 3D FEM and Pade Approximation in the Frequency Domain

Brahim Essakhi¹, Lionel Pichon²

LGEP, UMRS 8507 CNRS, SUPELEC,

UNIVERSITE PARIS SUD, UNIVERSITE PIERRE ET MARIE CURIE

Plateau du Moulon, 91192 Gif-sur-Yvette, France

¹ essakhi@lgep.supelec.fr ² pichon@lgep.supelec.fr

Abstract – The paper presents a finite element model for the calculation of the impedance of an antenna over a wide frequency band. The antenna has been designed to analyze a rectenna (rectifying antenna) in the context of wireless microwave energy transfer. The modelling approach combines a 3D edge element method (FEM) with a Padé approximation procedure. It allows to obtain an explicit expression of the impedance over a large frequency band. The comparison of the proposed technique with a standard finite element method shows that the computational cost is significantly reduced.

I. INTRODUCTION

Microwave rectennas (rectifying antennas) are devoted to power transmission and detection. Applications include long distance power beaming, signal detection and wireless control systems. Power transmitting and receiving systems must be designed so that the power transmitted from the transmitting antenna is transmitted efficiently to the rectenna and is converted into DC power by rectifiers. Efficient field-circuit simulations are required in the design and characterization of such rectennas since non linear lumped elements are included. The knowledge of the input impedance of the antenna is of particular importance in evaluation the conversion efficiency.

In [1] a rectenna structure involving a loop antenna was studied. This rectenna is devoted to low-power applications. The targeted applications include microwave power reception from various sources in a large frequency range. The operating frequency may belong to the industrial, scientific and medical band (central frequency of 2.45 GHz). Also investigations include radio-frequency identification (RFID) applications where wideband signals may be used. For these reasons a reliable circuit model of the rectenna allowing a global simulation over the band [0, 20] GHz was required. The circuit model takes into account both distributed electromagnetic portions of the antenna and the rectifier circuit. From the 3D electromagnetic modelling of the structure the input impedance was obtained as a function of the frequency. This technique provides an adequate way to incorporate the impedance into a non-linear circuit simulation. With such an approach the

impedance has to be calculated over a wide frequency band with a 3D modeling tool. This can be achieved as in [1] with a standard frequency domain method (boundary element method or finite element method for example).

A finite element model provides an efficient way for solving electromagnetic problems. In a frequency domain analysis the electromagnetic fields are discretized over a meshed volume. The unknowns are the solution of a linear system whose matrix depends on frequency. In a wide frequency band analysis the linear system has to be solved for each frequency of interest. This often leads to a huge computational cost. An alternative approach is to search for a power series expansion of the solution about a center frequency. The approach requires only one single matrix inversion. The radius of convergence is limited but it is possible to extend the interval using a corresponding Padé approximant. This technique is known as an asymptotic wave form analysis (AWE).

The AWE approach has been combined with integral equations in 3D [2]-[4] to solve scattering problems involving perfectly metallic obstacles. For solving general electromagnetic problems including inhomogeneous media and complex geometries, the finite element method (FEM) provides a powerful tool. The AWE approach used in connection with FEM was shown to deal with electromagnetic problems within bounded domains in [5]-[7] where passive microwave devices such as waveguides and cavities were studied. In these almost closed structures the boundaries of the studied domain consist of perfectly conducting walls or access planes. Then the efficiency of AWE relies on the fact that dominant poles and zeros of the network transfer function can be used to build rational approximations of the solution. Indeed in such a case the resonant modes, can be computed in a first step from a generalized eigenvalue problem and can be used in a second step to give an expansion of the solution. On the other hand, for electromagnetic problems in unbounded domains like radiation of an antenna in free space or scattering problems the fields cannot be expressed with resonant modes of the structure and efficient

Padé approximation are difficult to obtain. An extension of AWE combined with finite elements for radiation problems has been proposed in [8] for the 2D case. In a 2D analysis the structure is infinite along one direction and the electromagnetic problem reduces to a scalar wave problem (TM case or TE case). In such a configuration one of the two fields (electric or magnetic) has the same direction that the infinitely long structure. The ability of this method was demonstrated in the scattering of canonical obstacles having simple shapes.

In this work the AWE technique used in conjunction with finite elements is successfully extended in three dimensions (3D) for solving radiation problems in free space. The approach combines the vectorial finite element method and a Padé approximation. The numerical method is shown to provide a fast computation of the impedance of an antenna over a wide frequency band. The antenna is the loop antenna of the rectenna considered in [1] for which only a three dimensional analysis allows to obtain the distribution of the electromagnetic fields. The method is based on first order edge finite elements. A Silver-Müller boundary condition is used for the truncation of the domain. Once the finite element matrix has been built for one frequency an explicit expression (power series) of the fields and the impedance are available over a frequency band. From the power series a Padé approximation (rational function) can be derived. It is shown that a very good approximation is obtained even if several sharp resonance peaks are included in the studied range. The comparisons between the presented technique and a standard finite element analysis clearly underline the advantages of the proposed model.

II. ELECTROMAGNETIC PROBLEM

We consider the 3D problem of an antenna radiating in its surrounding medium. The dimensions of the studied device are shown in Fig. 1. The loop is assumed to be infinitely thin and perfectly conducting. However for the sake of generality the induced current density \mathbf{J} is included in the equations since the presented analysis remains also valid in this case. The loop is excited by an impressed current \mathbf{J}_{imp} between the ends of the two arms.

For a full wave analysis we deal with the Maxwell equations in the frequency domain:

$$\nabla \times \mathbf{E} = -j\omega \mathbf{B} \quad (1)$$

$$\nabla \times \mathbf{H} = \mathbf{J}_{imp} + \mathbf{J} + j\omega \mathbf{D}, \quad (2)$$

where \mathbf{E} and \mathbf{H} are the electric and magnetic field respectively, μ is the permeability, ε is the permittivity.

The constitutive relations are given by:

$$\mathbf{B} = \mu \mathbf{H} \quad (3)$$

$$\mathbf{D} = \varepsilon \mathbf{E}. \quad (4)$$

The Ohm law gives:

$$\mathbf{J} = \sigma \mathbf{E}. \quad (5)$$

From equations (1-4), we establish the vector wave equation in terms of the electric field \mathbf{E} :

$$\nabla \times \frac{1}{\mu} \nabla \times \mathbf{E} + j\omega(\sigma + j\varepsilon\omega)\mathbf{E} = -j\omega \mathbf{J}_{imp}. \quad (6)$$

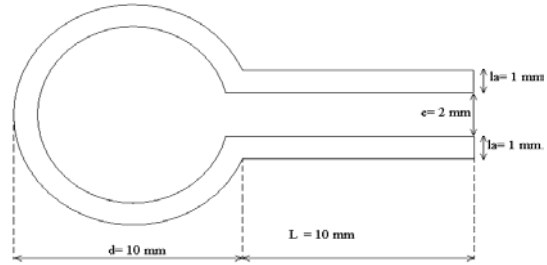


Fig. 1. The loop antenna and its dimensions.

III. FINITE ELEMENT FORMULATION

A computation using the finite element method is performed in a finite region which includes the antenna and some of its surrounding medium. In order to truncate the volume of the computational domain the Silver-Müller condition is applied as an absorbing boundary condition [9]. It is given by:

$$n \times \nabla \times \mathbf{E} = jk \mathbf{E}_{tan} \quad (7)$$

where k is the wave number in free space and \mathbf{E}_{tan} is the tangential electric field on the outer boundary surface.

This ABC preserves the sparsity and symmetric features of the final matrix. It is exact for normal incidence. Let denote Ω the computational domain and Γ the outer boundary. As usual with FEM, we define the space of the work:

$$V = \left\{ u \in (L^2(\Omega))^3, \nabla \times u \in (L^2(\Omega))^3 \right\}. \quad (8)$$

A weak formulation of the problem is obtained after multiplying the vector wave equation by a test function F in V :

$$\langle j\omega(\sigma + j\varepsilon\omega)\mathbf{E}, \mathbf{F} \rangle_{\Omega} + \langle \frac{1}{\mu} \nabla \times \mathbf{E}, \nabla \times \mathbf{F} \rangle_{\Omega} + \langle j\omega \sqrt{\frac{\varepsilon}{\mu}} \mathbf{E}, \mathbf{F} \rangle_{\Gamma} = -j\omega \langle \mathbf{J}_{imp}, \mathbf{F} \rangle_{\Omega} \quad (9)$$

where $\langle \cdot, \cdot \rangle_{\Omega}$ denotes the scalar product in V .

To solve equation (9) numerically, the domain is discretized with tetrahedral elements. The electric field can be written in terms of basis functions associated with the edges of these elements [10, 11]. From equation (9) and by using test functions \mathbf{F} the same as interpolation functions (Galerkin method) we get:

$$\left(A_0 + \omega A_1 + \omega^2 A_2 \right) \mathbf{v} = \mathbf{b} \quad (10)$$

where \mathbf{v} is the unknowns' vector, \mathbf{b} is the excitation currents vector and A_0, A_1 , and A_2 are matrices which only depend on the mesh and on the medium.

IV. AN EFFICIENT COMPUTATIONAL SCHEME FOR BROADBAND ANALYSIS

Consider an arbitrary ω_0 such that A_0 is non-singular, the Taylor series expansion of the matrix polynomial in equation (10), about the frequency ω_0 can be written as:

$$A(\omega) = \bar{A}_0 + (\omega - \omega_0) \bar{A}_1 + (\omega - \omega_0)^2 \bar{A}_2 \quad (11)$$

where the matrices A_i , ($i = 0, 1, 2$) can be obtained from equation (10) and equation (11):

$$\bar{A}_0 = A_0 + \omega_0 A_1 + \omega_0^2 A_2, \quad (12a)$$

$$\bar{A}_1 = A_1 + 2\omega_0 A_2, \quad (12b)$$

$$\bar{A}_2 = A_2. \quad (12c)$$

The solution vector $\mathbf{v}(\omega)$ has power series representation about ω_0 , given by:

$$\mathbf{v}(\omega) = \sum_{i=0}^{\infty} \mathbf{v}_i (\omega - \omega_0)^i. \quad (13)$$

The power series representation of the excitation vector $\mathbf{b}(\omega)$ is written as:

$$\mathbf{b}(\omega) = \sum_{i=0}^{\infty} \mathbf{b}_i (\omega - \omega_0)^i. \quad (14)$$

We can evaluate the coefficients of the power series of $\mathbf{v}(\omega)$ by the following procedure:

$$\left(\bar{A}_0 + (\omega - \omega_0) \bar{A}_1 + (\omega - \omega_0)^2 \bar{A}_2 \right) (\mathbf{v}_0 + \dots + \mathbf{v}_1 (\omega - \omega_0) + \dots) = \mathbf{b}_0 + \mathbf{b}_1 (\omega - \omega_0) + \dots \quad (15)$$

If we equate both sides of equation (15) term by term, we obtain the following iterative expression:

$$\mathbf{v}_i = \bar{A}_0^{-1} \mathbf{b}_i - \sum_{j=1, j \leq i} \bar{A}_0^{-1} \bar{A}_j \mathbf{v}_{i-j}, \quad i = 0, 1, \dots \quad (16)$$

It is very important to note that only a single inverse \bar{A}_0^{-1} is needed in the iteration procedure.

V. PADÉ APPROXIMATION

A Padé approximation is derived by expanding a function as a ratio of two power series and determining both the numerator and denominator coefficients. Padé approximations are usually superior to Taylor expansion when functions contain poles, because the use of rational functions allows a good representation, and it provides an extension beyond the interval of convergence of the series [12]. The solution is expressed as a power series of the form:

$$\mathbf{v}(\omega) = \sum_{i=0}^{\infty} \mathbf{v}_i (\omega - \omega_0)^i, \quad (17)$$

where the coefficients \mathbf{v}_i , $i = 0, 1, 2, \dots$ can be computed iteratively using (16). The expansion is convergent within the region $|\omega - \omega_0| < R$, where R is the radius of convergence of this power series.

Since $\mathbf{v}(\omega)$ is complex, and since the Padé approximants are rational functions, we concentrate on a single component of $\mathbf{v}(\omega)$, say $\mathbf{v}^j(\omega)$, and we write its power series representation in the form:

$$\mathbf{v}^j(\omega) = \sum_{i=0}^{\infty} \mathbf{v}_i^j (\omega - \omega_0)^i, \quad (18)$$

where the coefficient \mathbf{v}_i^j is scalar. A Padé approximant of the power series equation (18) is a rational function of the form:

$$[N/M](\omega) = \frac{Q_N(\omega)}{P_M(\omega)}, \quad (19)$$

where

$$Q_N(\omega) = \sum_{i=0}^N q_i (\omega - \omega_0)^i \text{ et}$$

$$P_M(\omega) = \sum_{i=0}^M p_i (\omega - \omega_0)^i. \quad (20)$$

We take $p_0 = 1$, the $M+N+1$ unknowns can be obtained by the condition that the equation

$$v^j(\omega) \approx [N/M](\omega), \quad (21)$$

holds up to terms $O(v^{N+M+1})$. This equation implies that

$$Q_N(\omega) = P_M(\omega) \sum_{i=0}^{\infty} v_i^j (\omega - \omega_0)^i. \quad (22)$$

Then we have

$$\sum_{i=0}^N q_i (\omega - \omega_0)^i = \sum_{i=0}^{\infty} l_i (\omega - \omega_0)^i \quad (23)$$

where

$$l_i = \sum_{k=0}^i v_{i-k}^j p_k. \quad (24)$$

Hence q_i and p_i can be determined from the following system

$$p_0 = 1 \quad (25a)$$

$$q_i = \sum_{k=0}^i v_{i-k}^j q_k, \quad \text{if } 1 \leq i \leq N \quad (25b)$$

$$p_i = 0, \quad \text{if } i > N \quad (25c)$$

$$\sum_{k=1}^i v_{i-k}^j p_k = -p_0 v_i^j, \quad \text{if } N < i < N + M \quad (25d)$$

$$p_i = 0, \quad \text{if } i > M. \quad (25e)$$

Hence the unknown coefficients of the Padé approximant can be determined from linear system. We use the diagonal Padé approximation ($N = M$) which is more accurate; in this case we have $2N+1$ unknown coefficients.

VI. NUMERICAL RESULTS

Figure 2 shows a typical mesh used in the computation for the loop and the surrounding air. The electromagnetic analysis was performed over a broad band I = [0 GHz, 20 GHz]. In a first step, the studied frequency band is divided in $L = 4$ intervals $I_i, i=1, \dots, L$ such that $I_1=[0 \text{ GHz}, 5 \text{ GHz}]$, $I_2=[5 \text{ GHz}, 10 \text{ GHz}]$, $I_3=[10 \text{ GHz}, 15 \text{ GHz}]$ and $I_4=[15 \text{ GHz}, 20 \text{ GHz}]$. In each band the centre frequency has been chosen in the middle.

We denote $[N/M]_i(\omega), i=1, \dots, L$ the Padé approximation of the impedance in each

interval I_i . In this case $N=M=2$. The impedance can be written as:

$$Z(\omega) = \sum_{j=1}^L Z^j(\omega), \quad (26)$$

where

$$Z^j(\omega) = \begin{cases} [2/2]_j(\omega) & \text{if } \omega \in I_j \\ 0 & \text{otherwise} \end{cases}.$$

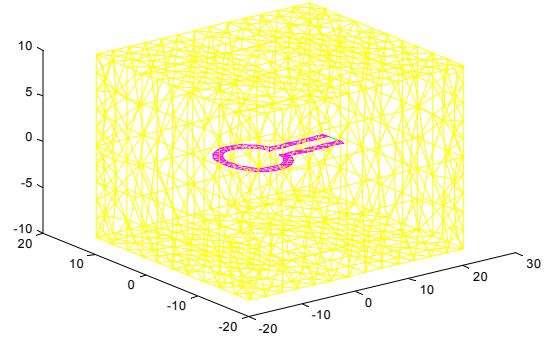


Fig. 2. The volume of the computation.

The comparison between a standard finite element model and the Padé approximation is shown on Fig. 3 and Fig. 4. The two curves are in an excellent agreement over the whole wide frequency band. In the standard approach the finite element problem has been solved for a number of 200 frequencies to obtain the behaviour of the curve. With the Padé approximation only 4 frequencies are needed. The computational cost is then significantly reduced since the amount of time required to find the Padé coefficients is negligible.

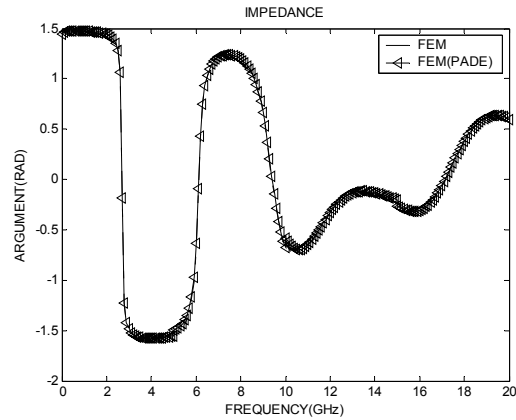


Fig. 3. Argument of the impedance: The comparison between 3D model and the Pade approximation [2/2] over four bands.

For three bands it was shown that the Padé approximant [3/3] gives very good results. Thus, for two bands a [3/3] approximation gives a bad

approximation at the junction between the two bands Fig. 5. In this case an increase of the order of the Padé approximant is required: we show the corresponding results for a [5/5] approximation in Fig. 6.

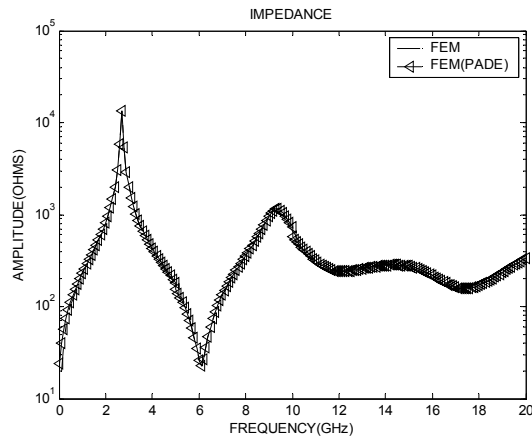


Fig. 4. The Amplitude: The comparison between 3D model and the Padé approximation [2/2] over four bands.

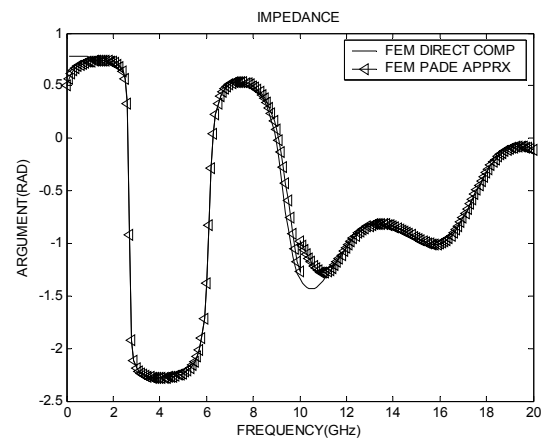


Fig. 5. Argument of the impedance: The comparison between 3D model and the padé approximation [3/3] over two bands.

VII. Conclusion

This paper describes an accurate and very efficient FEM approach to compute the impedance of an antenna over a wide frequency band. The electromagnetic problem addressed in this work is a fully three-dimensional one. In a standard finite element approach the linear system has to be solved for each frequency of interest. The power series expansion method presented in this work resolves this problem very efficiently. The advantage of this approach is that only a single resolution of the linear system is required to evaluate the series expansion using a Padé approximation. Then the approach

allows one to cover a whole given frequency band with a minimum number of resolution of the linear system. In particular the resonance peaks are very well recovered. It is worth to be noted that satisfactory results are obtained when using a Silver-Müller radiation condition: the impedance is computed from the near-field and numerical values near the antenna are not very sensitive to the boundary condition. Work is in progress to combine a Padé approximation with PML (perfectly matched layer) in order to address more general radiation problems in three dimensions for which global quantities have to be obtained over a wide band.

REFERENCES

- [1] P. Leroy, G. Akoun, B. Essakhi, L. Santandrea, and L. Pichon, "An efficient global analysis of a rectenna using the combination of full-wave model and a rational approximation," *EPJ-European physical journal*, Vol. 29, pp 39-45, 2005.
- [2] D. Jiao, X. Y. Zhu, and J. M. Jin, "Fast and accurate frequency-sweep calculation using asymptotic waveform evaluation and combined-field integral equation," *Radio Science*, Vol. 34, No. 5, Pages 1055-1063, September-October 1999.
- [3] Y. E. Erdemli, J. Gong, C. J. Reddy, and J. L. Volakis, "Fast RCS Pattern Fill Using AWE Technique," *IEEE Transactions on Antenna and Propagation*, Vol. 46, No.11, November 1998.
- [4] C. J. Reddy, M. D. Deshpande, C. R. Cockrell, and F. B. Beck. "Fast RCS Computation over a frequency band using method of moments in conjunction with asymptotic waveform evaluation technique," *IEEE Transactions on Antenna and Propagation*, Vol. 46, No. 8 August 1998.
- [5] S.V. Polstyanko, R. Dyczij-Edlinger, and J.F Lee, "A fast frequency sweep technique for the efficient analysis of dielectric wavaguides," *IEEE Transaction on microwave theory and techniques*, Vol. 45, No. 7, pp 1118-1126, July 1997.
- [6] X.M Zhang, and J.F Lee, "Application of the AWE Method with the 3-D TVFEM to model responses of passive microwave components," *IEEE Transaction on microwave theory and techniques*, Vol. 46, No. 11, pp 1735-1741, November1998.
- [7] J.E Bracken, D.K Sun, and Z.J. Cendes, "S-Domain Methods for Simultaneous Time and Frequency Characterization of

- Electromagnetic Devices,” *IEEE Transaction on microwave theory and techniques*, Vol. 46, No. 9, pp 1277-1290, September 1998.
- [8] M. Kuzuoglu, and R. Mittra, “Finite element solution of electromagnetic problems over a wide frequency range via the Padé approximation,” *Comput. Methods Appl. Mech. Engrg*, Vol. 169, pp 263-277, 1999.
- [9] A.K. Belhora, and L. Pichon, “Efficient absorbing boundary conditions for the finite element solution of 3D scattering problems,” *IEEE Transactions on Magnetics*, Vol. 31, No. 3, pp. 1534-1537, May 1995.
- [10] L. Pichon, and A. Razek, “Analysis of three dimensional dielectric loaded cavities with edge elements,” *ACES Journal*, Vol. 6, No. 2, pp 133-142, 1991.
- [11] J.P. Webb, “Edge elements and what they can do for you,” *IEEE Transactions on Magnetics*, Vol. 25, No 2, pp. 1460-1465, March 1993.
- [12] C. Brezinski *Padé-Type Approximation and General Orthogonal Polynomials*, Birkhäuser-Verlag, Basel, 1980.



Brahim Essakhi was born in Rabat, in 1974. He obtained a Master's in Applied Mathematics from Ecole Normale Supérieure (ENS) in Cachan (France) in 2001. In 2002 he joined the Laboratoire de Génie Electrique de Paris (LGEP) associated to CNRS, SUPELEC, University of Paris-Sud and University of Pierre et Marie Curie where he earned a PhD in 2005. His main scientific interests are numerical methods, wave propagation modeling, and electromagnetic compatibility.



Lionel Pichon was born in Romorantin, France, in 1961. He obtained the Dip. Eng. from Ecole Supérieure d'Ingénieurs en Electronique et Electrotechnique (ESIEE) in 1984. In 1985 he joined the Laboratoire de Génie Electrique de Paris LGEP associated to CNRS, SUPELEC, University of Paris-Sud, University of Pierre et Marie Curie where he earned a PhD in 1989. He is now Chargé de Recherche at the CNRS. His research interests include computational electromagnetics in microwaves, and electromagnetic compatibility.

EBG Design using FSS Elements in Rectangular Waveguide

R. S. Kshetrimayum¹ and L. Zhu²

¹Microwave Lab, Electronic Communication Engineering, Indian Institute of Science,
Bangalore, India 560012

Email: krakhesh@ece.iisc.ernet.in

²Communication Research Laboratory, School of Electrical & Electronic Engineering,
Nanyang Technological University, Singapore 639798

Abstract — A novel waveguide based EBG structure is originated by periodically loading FSS strip elements in rectangular waveguide. Efficient and accurate Hybrid MoM-Immittance Approach is used for the full-wave characterization, which is validated by experimental results. A parametric study of effect of various factors on the EBG width has been done. Various existing and novel FSS strips have been investigated to improve the roll-off characteristics in the passband. Double square loop FSS strip loaded waveguide gives improvement in the roll-off factors. Such novel waveguide based EBG structures may be used in the design of harmonic suppressed waveguide filters, band reject filters and suppression of harmonics for waveguide resonators or antennas.

I. INTRODUCTION

Photonic bandgap (PBG) structures are artificially made structures with periodically loaded obstacles in 1-D, 2-D, or 3-D. They are capable of forbidding electromagnetic propagation in either all or selected directions [1]-[3]. Although periodic structures have been investigated in microwave community for many decades, new ideas and concepts developed in optical domain [4]-[5] have renewed interest in microwave area. EM waves behave in such crystals similar to that of electronic behavior in semiconductors hence it is also named as Electromagnetic bandgap (EBG) structure. In microwave community, preferable nomenclature is EBG structure [6]. As in Photonic crystals (PC), photon propagation is impeded by periodic discontinuity, EM waves in EBG materials are hindered by periodic discontinuity making it a slow wave structure. The slow wave behavior in passband characteristics of EBG structures can be used as a slow wave medium for size miniaturized microwave devices and circuits [7]. Surface waves propagating in high dielectric constant slabs carry substantial energy in unwanted directions and create unnecessary coupling between the devices. EBG structures can be used to alleviate these problems by suppressing higher order modes and surface waves [8]. In filters, EBG structures are employed for harmonic suppression and improving filter performance without increasing dimension of the device [9]. In antenna design, EBG structures can be used to enhance antenna broadside gain, to suppress surface

waves and to reduce cross-polarization levels [10]. On the basis of dimensions in which periodic perturbations like dielectric rods, holes and patterns in waveguides and microstrip substrates are introduced, EBG structures can be categorized as 1-D, 2-D or 3-D. Conventional EBG structures are 1-D/2-D/3-D periodic structures that satisfy Bragg's conditions, i.e, inter-cell separation (period) is close to half guided wavelength. Frequency Selective Surface (FSS) is widely used in microwave and optical engineering as spatial and frequency filters [11]-[12]. In this paper, we have originated an alternative 1-D waveguide based EBG structure by periodically loading rectangular waveguide with FSS strip elements printed on dielectric substrate. Efficient and accurate Hybrid MoM-Immittance Approach [13] has been used for all the simulation works.

II. ORGANIZATION OF THE PAPER

First, a wide resonant strip in X-band waveguide is validated with experimental results. There is good agreement between the Hybrid MoM-Immittance and experimental results. Next, we study the effect of various parameters on the EBG width for simple square FSS strip loaded waveguide. From the parametric study of effect of various factors on the EBG width, we have designed an optimized wideband EBG structure using the FSS square strip. It has been observed that although square FSS strip loaded periodic waveguide structure gives a very broad EBG width, the roll-off characteristics in the passband of the periodic waveguide structure is not good. Hence we try to improve this performance by considering various existing FSS and novel FSS strip elements loaded waveguide structure. Seven FSS strip structures viz., square (FSS1), square loop (FSS2), ring (FSS3), cross (FSS4) and other novel FSS structures: double square loop (FSS5), FSS6 (FSS2+FSS4) and FSS7 (FSS1+FSS4) loaded waveguide has been investigated. Double square loop loaded periodic waveguide structure shows a promising candidate for improving the roll-off factors in the waveguide based EBG structures. The scattering performance for a periodic waveguide based EBG structure loaded with different number of double square loop unit/cells have been investigated. It is observed that with the increase of number of unit/cells,

insertion loss goes into deep rejection band and roll-off factor in the passband improves. Such waveguide based EBG structures can be used for various applications like design of harmonic suppressed waveguide filters, band rejection filters and harmonic suppression of waveguide resonators.

III. EXPERIMENTAL VALIDATION OF HYBRID MOM-IMMITTANCE APPROACH

Hybrid MoM-Immittance approach is the hybrid of MoM and Immittance approach [13]. In this method, Galerkin's MoM method and Fourier transform techniques are employed to transform the electric-field integral equation (EFIE) into a matrix system of linear equations. Dyadic Greens' functions are calculated from the TE and TM circuit models for 1-D inhomogeneous multilayered structures. It has been employed for study of guided-wave characteristics of printed periodic waveguide structures [14]. This method has been validated for various waveguide based structures in comparison with analytical results [14] and HFSS simulation results [13]-[14]. Here we will do an experimental validation of this efficient and accurate approach. Fig. 1(a) shows a X-band waveguide with a centered strip of width=0.280 inch and depth=0.360 inch. The equivalent circuit of the waveguide structure under investigation can be represented by a shunt susceptance as shown in Fig. 1(b). Fig. 1(c) illustrates the normalized susceptance versus frequency. Note the choice of basis functions: half-basis functions are employed at the edge where the strip touches the waveguide walls. It can be observed that there is close agreement between the Hybrid MoM-Immittance Approach and experimental results from [15].

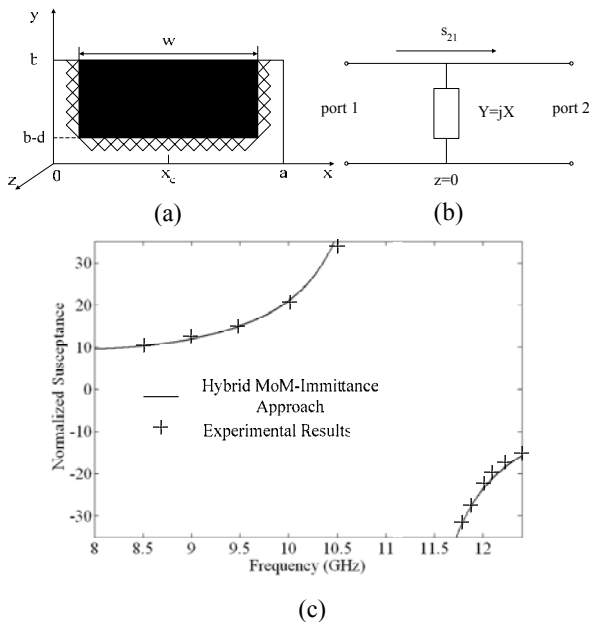


Fig. 1. A rectangular waveguide with a wide resonant strip (a) Cross section, (b) Equivalent circuit, and (c) Normalized susceptance of a centered strip of $w=0.280$ inch and $d=0.360$ inch.

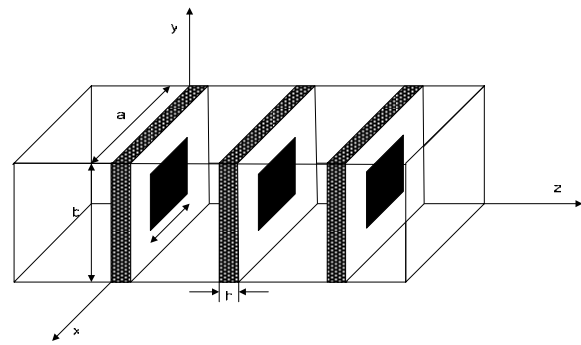


Fig. 2. 3-D geometry of a rectangular waveguide ($a \times b$) loaded with a square strip (l) printed on a dielectric layer of thickness h (3 unit cell).

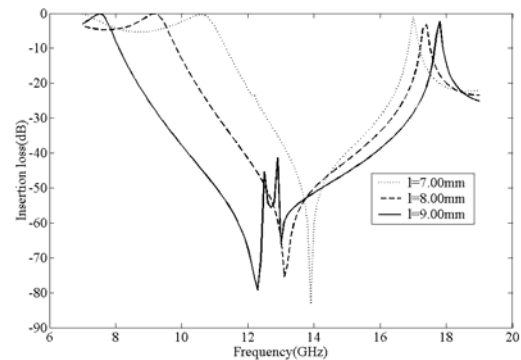


Fig. 3. Insertion loss versus frequency for different dimension of square strip (l).

IV. EFFECT OF VARIOUS PARAMETERS ON EBG WIDTH

Figure 2 shows a rectangular waveguide loaded with three transverse layers of FSS square strips printed on dielectric layer of thickness h . In order to understand the EBG performances properly, let us investigate the effect of various parameters on the EBG width. The actual waveguide based EBG structure composed of periodic waveguide structures with many transversal layers of FSS strips. Here, we have considered a three unit/cell finite periodic waveguide structure for investigation on the -10 dB insertion loss EBG width. The various parameters which may control the EBG performances are:

- 1) Dimension of FSS square strip (l),
- 2) Dielectric constant of dielectric layer on which the FSS elements are printed (ϵ_r),
- 3) Thickness of the dielectric layer (h),
- 4) Period of the periodic waveguide structure (p),
- 5) Number of unit/cells (h).

The square FSS strip elements are printed on a dielectric layer of $\epsilon_r = 3$ and thickness $h = 1$ mm. The waveguide dimensions are $a = 22.86$ mm and $b = 10.16$ mm and the dimension of the FSS square strip elements is chosen as $l = 7$ mm.

A. Dimension of FSS Square Strip (l)

It has been observed that with increase of dimension for the FSS square strip from $l = 7$ mm, 8 mm, and 9 mm (other parameters kept the same), there is downward shift in the resonant frequency of the FSS square strip element as illustrated in Fig. 3. There is also significant increase in the -10dB insertion loss EBG width with increase in the dimension of FSS square strip (refer to Table I).

B. Dielectric Constant of Dielectric on which the FSS Elements are Printed (ϵ_r)

As the relative permittivity (ϵ_r) of the dielectric layer on which FSS square strip are printed increases from 3, 4, and 5.7 (other parameters kept constant for all the three cases), the resonant frequency of FSS square printed waveguide structure decreases as depicted in Fig. 4 and the fractional EBG width increases as tabulated in Table I.

C. Thickness of the Dielectric Layer (h)

An interesting observation is that when we increase the thickness of the dielectric layer, the fractional EBG width decreases. For a dielectric layer of $\epsilon_r = 3$ and thickness of the dielectric layer $h = 1$ mm, the fractional EBG width is 24% (refer to Fig. 5 and Table I). It reduces to 13.51% as we increase the dielectric layer thickness h to 3 mm, keeping same the other parameters of the waveguide structure of Fig. 2.

D. Periodicity (p)

It is a good idea to investigate the role of periodicity p in increasing the EBG width. Fig. 6 illustrates the bandstop of square FSS printed waveguide structure of Fig. 2 for various periodicity p . It can be observed that there is a downward frequency shift in bandstop as periodicity p is increased from $p = 4.8$ mm, 5.8 mm, and 6.8 mm. Besides, there is visible enhanced bandwidth for periodicity of $p = 4.8$ mm in comparison to other values of p . It is because the connecting waveguide section approaches half guided-wavelength, the frequency at which each square loop resonates, thereby further widening the EBG width. The scattering parameter results shown are for two unit/cells i.e., $n = 2$ for periodic waveguide structure.

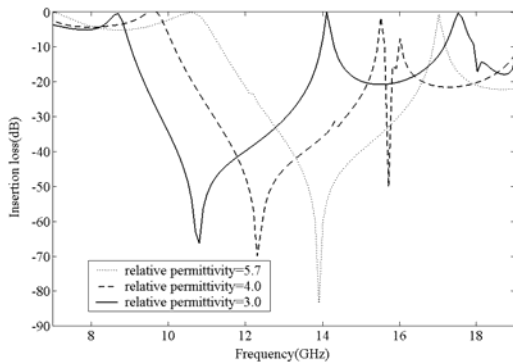


Fig. 4. Insertion loss versus frequency for different values of relative electrical permittivity (ϵ_r).

E. Number of Unit/cells (n)

Fig. 7 shows insertion loss (S_{21}) for the finitely extended periodic structure with number of unit cells varying from $n = 2, 3,$ and 5 for a fixed periodicity $p = 4.8$ mm. It can be observed that as number of unit cells (n) increases, insertion loss goes into deep rejection band as mentioned in many literatures [3]. There is also slight decrease in the EBG width as the number of unit/cells increases as shown in Fig. 7.

Table I. -10 dB insertion loss EBG width versus various parameters.

a	9mm	8mm	7mm
EBG width	(18.4-8.0)/13.2	(18.2-12.2)/15.2	(18.2-14.3)/16.2
	78.78%	39.47%	24%
Relative permittivity	3	4	7
EBG width	(18.2-14.3)/16.25	(16.7-12.7)/14.7	(14.8-10.8)/12.8
	24%	27.2%	31.25%
h	1mm	2mm	3mm
EBG width	(18.2-14.3)/16.25	(16.4-13.8)/15.1	(15.8-13.8)/14.8
	24%	17.21%	13.51%
p	4.8mm	5.8mm	6.8mm
EBG width	(15.5-9.6)/12.55	(15.3-10.1)/12.7	(15.2-10.8)/13.6
	47.01%	40.94%	33.84%

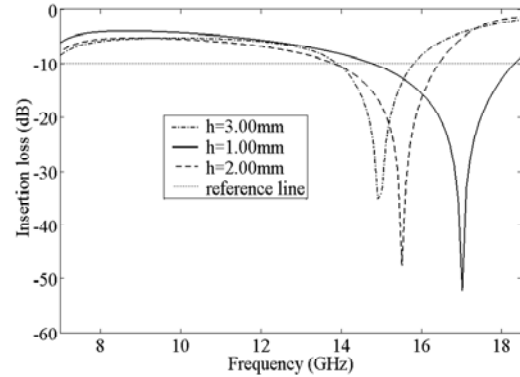


Fig. 5. Insertion loss versus frequency for different thickness of the dielectric layer (h).

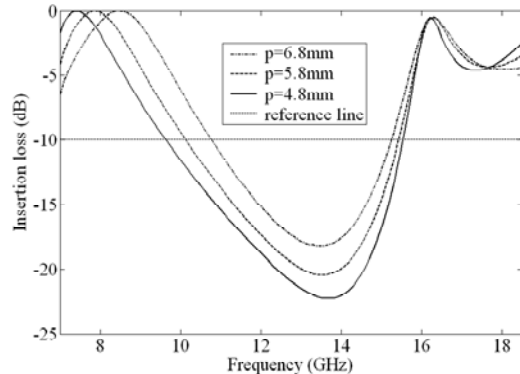


Fig. 6. Insertion loss versus frequency for different period (p).

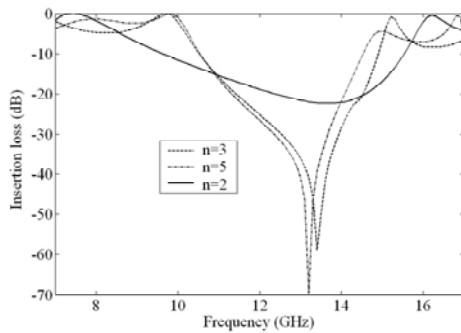


Fig. 7. Insertion loss versus frequency for different number of units/cells (n).

V. COMPACT WAVEGUIDE BASED EBG STRUCTURE

A waveguide based EBG structure is constructed by periodically loading FSS square strips in rectangular waveguide whose geometry (side view) is shown in Fig. 7 (b) and its front view is depicted in Fig. 7 (a). The thickness of the dielectric layer h is chosen as 1mm and the relative permittivity of the dielectric layer is 3. The period p is chosen approximately $\lambda_g/2$ (at the Bragg's frequency) which is equal to 4.8 mm. The scattering performance of the designed EBG structure is plotted in Fig. 7 (c). It can be observed that there exists a deep bandgap or forbidden band with $|S_{11}|$ of about 0dB in the frequency region from 10.5 GHz to 15.5 GHz. The EBG structure is compact because of the increased slow-wave factor due to the dielectric layer. For $n=5$, the overall length of the 1-D EBG structure is $5 \text{ mm} \times 4.8 \text{ mm} = 24 \text{ mm}$ only.

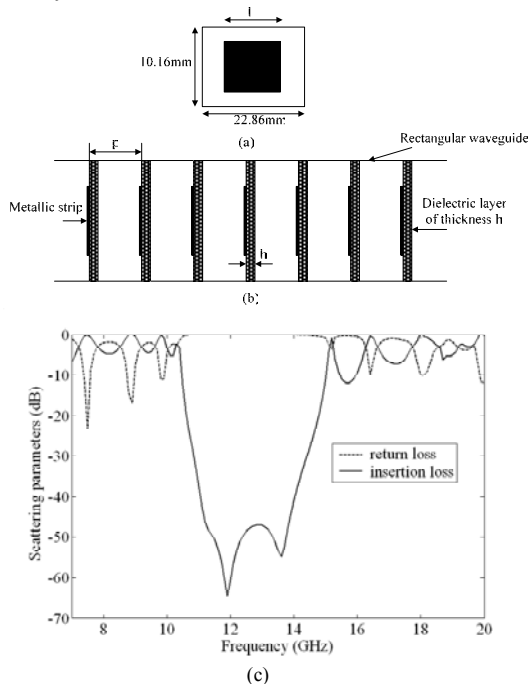
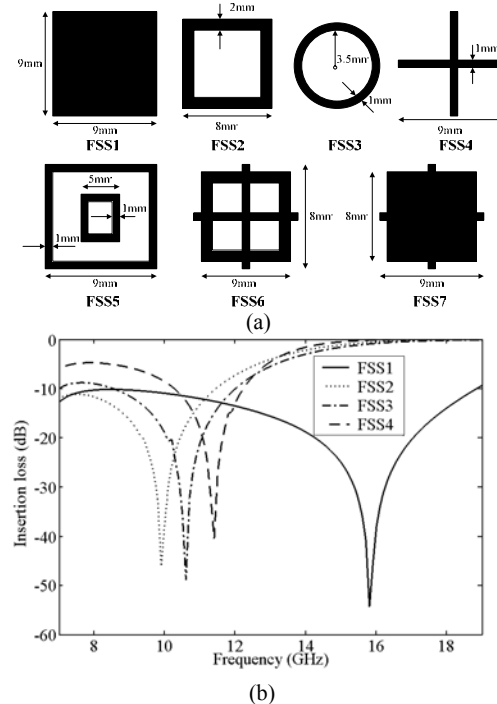


Fig. 8. Geometry of the waveguide based EBG structure; (a) Front view, (b) Side view, and (c) Scattering performance of the waveguide based EBG structure.

VI. IMPROVING THE ROLL-OFF CHARACTERISTICS

In this section, we will consider various FSS strip loaded waveguide structure to improve the EBG roll-off characteristics in the passband. Several FSS strip structures viz., square (FSS1), square loop (FSS2), ring (FSS3), cross (FSS4) and other novel FSS structures: double square loop (FSS5), FSS6 (FSS2+FSS4) and FSS7 (FSS1+FSS4) loaded waveguide have been investigated and their front view is depicted in Fig. 9 (a). The insertion loss in dB for first 4 FSS structures loaded waveguide structure is shown in Fig. 9(b). The insertion loss in dB for remaining 3 novel FSS structures loaded waveguide structure is depicted in Fig. 9(c). It can be observed that the insertion loss characteristics after resonance go upward towards zero as the frequency increases whereas the insertion loss before resonance usually touches around -10 dB and goes downward further as the frequency decreases. To improve the roll-off characteristics, it should go to 0 dB instead of -10 dB and then should go down as the frequency decreases. The best insertion loss characteristics for improving the EBG roll-off characteristics is for FSS 5 i.e., double square loop FSS structure.

Since the double square loop FSS strip loaded waveguide unit/cell gives the best roll-off characteristics. Let us study the effect of number of unit/cells on the EBG performance specially the roll-off characteristics. From Fig. 10 (b), we can see that as the number of unit/cells of the finite periodic waveguide structure whose geometry depicted in Fig. 10 (a), the roll-off factor increases. The dimensions of the double square loops are chosen as $l_1=9 \text{ mm}$ and $l_2= 5\text{mm}$. Both the square loops have strip thickness 1mm. They are transversely put in a X-band waveguide. The period p is chosen as 5.58 mm and thickness of the dielectric layer of dielectric constant 3 is taken as $h=1 \text{ mm}$.



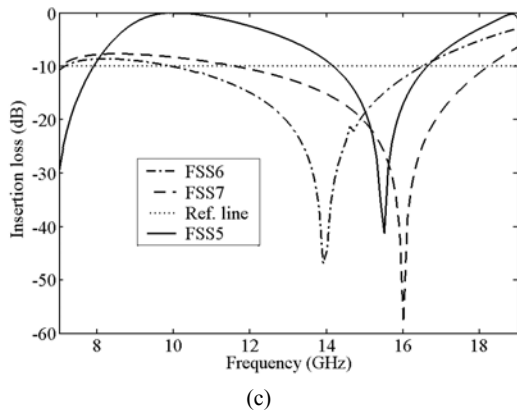


Fig. 9. (a) Front view of the waveguide loaded with various FSS strips, Insertion loss for (b) first 4 FSS strip elements, and (c) remaining 3 novel FSS strip elements.

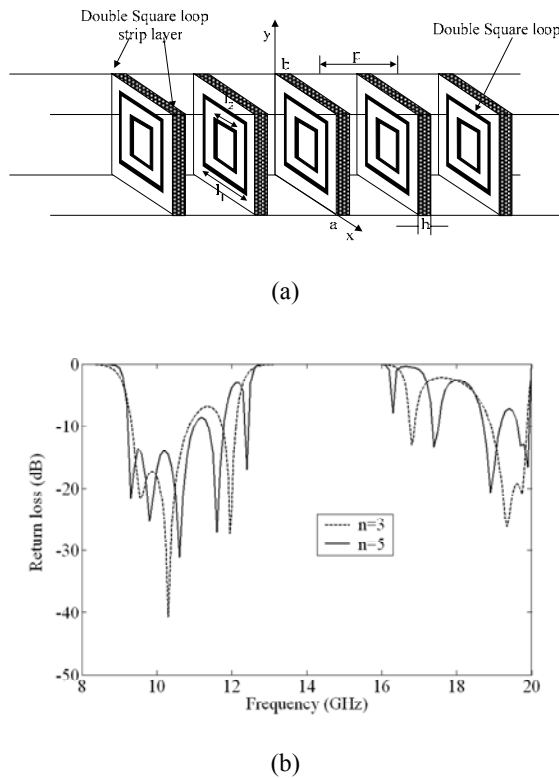


Fig. 10. (a) Geometry of double square loop FSS printed finite periodic waveguide structure acting as EBG structures and (b) Magnitude of scattering parameters.

VII. CONCLUSION

In this paper, we have originated and investigated a novel EBG structure by periodically loading transversally FSS strip elements in rectangular waveguide. First, we have done a parametric study on effect of various factors on the EBG width. Based on the parametric study, an optimized wideband waveguide based EBG structure using the square FSS strip element has been designed.

Although, the EBG structure using simple square FSS strip elements exhibits broad EBG width, the roll-off factor in the passband is not good. We have investigated various existing and novel FSS strip elements to improve its roll-off factors. Double square loop FSS printed waveguide structure shows a promising candidate for this. It has also been observed that with the increase of number of unit/cells, the insertion loss goes into deep rejection band and the roll-off factor in the passband improves. Such EBG structures can be used in the design of harmonic suppressed waveguide filters, band rejection filters and harmonic suppression of waveguide resonators.

REFERENCES

- [1] F. R. Yang, R. Coccioli, Y. Qian, and T. Itoh, "Planar PBG structures: Basic properties and applications," *IEICE Trans. Electron.*, vol. E83-C, no. 5, pp. 687–696, May 2000.
- [2] *IEEE Trans. on Microwave Theory Tech.*, (Special Issue), vol. 47, Nov. 1999.
- [3] L. Zhu, "Guided-wave characteristics of periodic coplanar waveguides with inductive loading: unit length transmission parameters," *IEEE Trans. on Microwave Theory Tech.*, vol. 51, pp. 2133–2138, Oct. 2003.
- [4] E. Yablonovitch, "Photonic band-gap structures," *J. Opt. Soc. Am. B*, vol. 10, no. 2, pp. 283–295, Feb. 1993.
- [5] J. D. Joannopoulos, R. D. Meade, and J. N. Winn, *Photonic Crystals*, Princeton Univ. Press, Princeton, NJ, 1995.
- [6] A. A. Oliner, "Periodic structures and photonic-band-gap terminology: Historical perspective," in *Proc. 29th European Microwave Conf.*, Munich, Germany, pp. 295–298, Oct. 1999.
- [7] D. Ahn, J.-S. Park, C.-S. Kim, J. Kim, Y. Qian, and T. Itoh, "A design of the low-pass filter using novel microstrip defected ground structure," *IEEE Trans. Microwave Theory Tech.*, vol. 49, no.1, pp. 86–93, Jan. 2001.
- [8] R. Coccioli, and T. Itoh, "Design of photonic band-gap substrates for surface waves suppression," in *Proc. IEEE International Microwave Symposium Dig.*, vol. 3, pp. 1259–1262, June 1998.
- [9] R. Gonzalo, P. D. Maagt, and M. Sorolla, "Enhanced patch antenna performance by suppressing surface waves using photonic-band substrates," *IEEE Trans. Microwave Theory Tech.*, vol. 47, no.11, pp. 2123–2130, Nov. 1999.
- [10] B. A. Munk, *Frequency Selective Surfaces: Theory and Design*, New York: John Wiley & Sons, Inc., 2000.
- [11] R. Mittra, C. H. Chan, and T. Cwik, "Techniques for analyzing frequency selective surfaces - a review," *Proc. IEEE*, vol. 76, no. 12, pp. 1593–1615, Dec. 1988.

- [12] *Frequency Selective Surface and Grid Array* Edited by T. K. Wu, 2nd ed., New York: John Wiley & Sons, Inc., 1995.
- [13] R.S. Kshetrimayum, and L. Zhu, "Hybrid MOM-Immittance approach for full-wave characterization of printed strips and slots in layered waveguide and its applications," *IEICE Trans on Electron.*, vol. E87-C, no. 5, pp. 700-707, May 2004.
- [14] R. S. Kshetrimayum, and L. Zhu, "Guided-wave characteristics of waveguide based periodic structures loaded with various FSS strip layers," *IEEE Trans. on Antennas Propagat.*, Vol. 53, No. 1, pp 120-124, Jan. 2005.
- [15] H. B. Chu, and K. Chang, "Analysis of a wide resonant strip in waveguide," *IEEE Trans. Microwave Theory Tech.*, vol. 40, pp. 495-498, March 1992.



Rakesh Singh Kshetrimayum (S'01-M'05) received the B. Tech. (first class honors) degree in Electrical Engineering from the Indian Institute of Technology, Bombay, India, in 2000 and the Ph.D. degree in Electrical and Electronic

Engineering from the Nanyang Technological University, Singapore, in 2005. From 2001 to 2002, he was a Software Engineer at the Mphasis Architecting Value, Pune, India. From 2004 to 2005, he was a Research Associate at the Electrical Communication Engineering Department, Indian Institute of Science, Bangalore, India. From May-July 2005, he was a Post-Doctoral Visiting Scholar at the Electrical Engineering Department, Pennsylvania State University, Pennsylvania, USA. Presently, he is a faculty at the Electronics and Communication Engineering department of the Indian Institute of Technology, Guwahati. His research interests include printed periodic structures, filters, EBG, metamaterials, computational electromagnetics, scattering problems and microstrip antennas. Dr Kshetrimayum is also a member of the IEICE, Japan and IEE, UK. He was awarded the KTH-Royal Institute of Technology-Stockholm Electrum Foundation Scholarship (2003-2004), the Nanyang Technological University - Singapore PhD Research Scholarship (2001-2004), the Travel Grant to attend the International Symposium on Microwave and Optical Technologies ISMOT 2005 at Fukouka, Japan. He is listed in Who's Who in the World 2006 23rd Edition.



Lei Zhu (S'91-M'93-SM'00) received the B.Eng. and M.Eng. degrees in radio engineering from the Nanjing Institute of Technology (now Southeast University), Nanjing, China in 1985 and 1988, respectively and the Ph.D. degree in Electronic Engineering from the University of Electro-Communications, Tokyo, Japan in 1993. From 1993 to 1996, he was a Research Engineer with Matsushita-Kotobuki Electronics Industries Ltd., Tokyo, Japan. From 1996 to 2000, he was a Research Fellow with Ecole Polytechnique de Montréal, Montréal, QC, Canada. Since July 2000, he has been an Associate Professor with the School of Electrical and Electronic Engineering, Nanyang Technological University, Singapore. His current research interests include the study of planar integrated dual-mode filters, ultra-broad bandpass filters, broad-band interconnects, planar antenna elements/arrays, uniplanar coplanar waveguide (CPW)/coplanar stripline (CPS) circuits as well as full-wave three-dimensional (3-D) method of moments (MoM) modeling of planar integrated circuits and antennas, numerical deembedding or parameter-extraction techniques and field-theory-based computer-aided design (CAD) synthesis/optimization design procedures. Dr. Zhu had held as an Associate Editor of the *IEICE Transactions on Electronics* (2003-2005) and a member of the Editorial Board of the *IEEE Transactions on Microwave Theory and Techniques* (2000-2005). He was the recipient of the Japanese Government (Monbusho) Graduate Fellowship (1989-1993). He was also awarded the 1996 Silver Award of Excellent Invention presented by the Matsushita-Kotobuki Electronics Industries Ltd., Japan, the 1997 Asia-Pacific Microwave Prize Award presented at the Asia-Pacific Microwave Conference, Hong Kong. In 2002, he was a Japan Society for Promotion of Science (JSPS) Research Fellow and a Guest Professor at the University of Ulm, Germany in 2005.

Electromagnetic Modeling and Design of Dual-Band Septum Polarizers

Anatoliy A. Kirilenko¹, Dmitriy Yu. Kulik¹, Leonid A. Rud¹, Vladimir I. Tkachenko¹, and Naftali Herscovici²

¹Institute of Radiophysics and Electronics
National Academy of Sciences of Ukraine
Kharkov, 61085, Ukraine

²Atlantic Microwave Co.
Bolton, MA 01740-1196, USA

Abstract—A highly efficient, full-wave electromagnetic model and CAD of septum polarizers terminated with a square or circular output waveguide is presented. The model is based on the mode-matching and generalized S-matrix techniques. The capabilities of the CAD program are demonstrated by the design of dual-band polarizers where the separation between two bands is more than 50%. For a square output polarizer, results are compared and found to be in good agreement with data obtained with the WASP-NET program. A discussion on the inherent limitations of the achievable performance and critical parameters is presented. An influence of higher-order modes propagating in the polarizer output over the high-frequency operation band on the radiation and polarization patterns of a septum polarizer combined with a corrugated conical horn is specially investigated.

I. INTRODUCTION

Septum polarizers (SP), built on a square waveguide with stepped ridged waveguide junctions, have found many applications in antenna and other microwave systems. Single-band configurations with a square output waveguide were widely investigated. The four-step polarizer, initially designed in [1] by trial and error experimental methods, satisfied the return loss criteria but required an additional dielectric-slab phase shifter to adjust the 90-degree phase difference between the TE_{10} and TE_{01} orthogonal modes. There were difficulties in producing an acceptable phase shift with an experimental tuning of the polarizer without phase-adjusting structures, [2].

Full-wave solutions and numerical optimization procedures allowed the design of various single-band polarizers with a square output port that met the required characteristics over a broad bandwidth. The design results of a five-step septum polarizer without an

additional phase adjustment were reported in [3]. A section of corrugated waveguide was proposed to use as the phase-correction device, [4]. The broadband polarizers with a stepped-thickness septum were investigated in [5], [6]. A dynamical optimization procedure that included in the optimization process not only the stepped septum configuration but also several step discontinuities (placed before and after the septum) was proposed in [7]. An algorithm based on the approximation of aperture field distribution by Gegenbauer polynomials was used in [8] to analyze the SP experimentally studied in [6].

The septum polarizer with a circular output port is more convenient for antenna applications because it can be connected directly to a flange of smooth or corrugated conical horn. An example of the design of a square septum polarizer, which is directly combined with a smooth conical circular waveguide horn, is shown in [9]. A design procedure for the single-band polarizer with a circular output waveguide is discussed in [8] however results of this design were not presented. Some results are reported in [10] for compact three- and four-step polarizers.

To the authors' knowledge, except for [11], dual-band septum polarizers operating over two distant (with more than 15% separation) frequency bands have not been yet considered in the literature. In addition to the need to meet common requirements (such as return loss, isolation, and axial ratio performance), in this case a new parameter has to be considered: the level of suppression of the higher-order modes. These modes are always excited and can propagate over the high-frequency band. In the case of square output port, these modes are the TE_{11} and TM_{11} ones, and in the case of circular output port they are the axial-symmetric TM_{01} and two polarization-degenerated TE_{21} modes.

In the present paper, the electromagnetic model, optimization procedure, designing results for the dual-band polarizers with square or circular output waveguides, and some features of their characteristics are discussed.

II. DESIGN PROCEDURE

II.1. The Electromagnetic Model

A polarizer with a circular output waveguide and its geometrical parameters are shown in Fig. 1. The electromagnetic model is based on the generalized S -matrix technique. In applying this technique, the key-elements are identified with the following waveguide discontinuities:

- double step in a rectangular waveguide;
- bifurcated-to-ridged waveguide transition;
- ridged-to-ridged waveguide junction;
- square-to-square waveguide junction;
- square-to-circular waveguide transition.

The full-wave S -matrices of all the key-elements are calculated using the mode-matching technique. In the case when the jointed circular and square waveguides have overlapping cross-sections (as shown in Fig. 1(a)), this transition is considered as two waveguides connected via a zero-length square waveguide with the wall size $a_{vrt} = D$ where D is the diameter of the output circular waveguide. In this case, the circular output is circumscribed to the virtual square waveguide. In this case, the circular output is circumscribed to the virtual square waveguide. All the aforementioned key-elements are calculated and combined with the aid of an electromagnetic solver similar to the one reported in [12]. The eigen-value problem for the single-ridged waveguide is solved using the moment method with basis and test functions that take into account the field behavior near edges. Some details of this method can be found in [13].

II.2. The Optimization Procedure

The SP-CAD program allows the design of a dual- and single-band polarizer according to a given set of specifications such as:

- return loss (RL);
- isolation (IS) between input waveguides;
- axial ratio (AR) of the resulting field generated by two outgoing orthogonal dominant modes;
- suppression level (SL) of the higher parasitic modes in the output port if the latter is overmoded.

The used optimization procedure is based on the descent method.

The SP-CAD program operates with the given number

of polarizer components. Some of them are fixed, and others are changed during the optimization process. For a given number of septum steps N , the fixed geometrical parameters are:

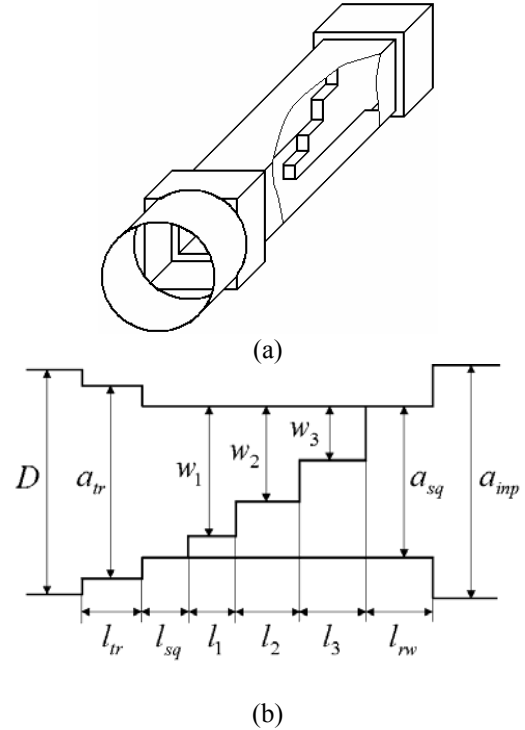


Fig. 1. Schematic structure of a three-step polarizer with a circular output waveguide. (a) General view, (b) Longitudinal-section view.

- the cross-sections of the two identical input rectangular waveguides, $a_{imp} \times b_{imp}$;
- the septum thickness, t ;
- the size of a square housing for the ridged waveguide sections, $a_{sq} \times a_{sq}$;
- the size of the transformer square section, $a_{tr} \times a_{tr}$, placed between the above-mentioned housing and output circular waveguide;
- the diameter of the circular waveguide, D .

The other available SP configurations have the square output port with $a_{out} = a_{tr}$.

Generally, the gap sizes w_i and lengths l_i , $i = 1, 2, \dots, N$ of the single-ridged waveguide sections, the length l_{rv} of the two identical rectangular waveguides of the $a_{imp} \times (a_{sq} - t)/2$ cross section, and the lengths l_{sq} and l_{tr} of the square waveguide sections (see Fig. 1(b)) are included in the vector of objective variables for the

optimization procedure. The following error function is minimized during the optimization:

$$F(\bar{x}) = \min \sum_{j=1}^2 \sum_{m=1}^{M_j} \left[W_{RL}^{(j)} \left(\frac{RL_j}{RL_m^{(j)}} \right)^2 + W_{IS}^{(j)} \left(\frac{IS_j}{IS_m^{(j)}} \right)^2 + W_{AR}^{(j)} \left(\frac{AR_m^{(j)}}{AR_j} \right)^2 + W_{SL}^{(j)} \left(\frac{SL_j}{SL_m^{(j)}} \right)^2 \right] \quad (1)$$

where

- \bar{x} is the vector of the objective variables;
- M_j is the given number of the frequency points $f_m^{(j)}$ within the j th specified band;
- $W_{RL}^{(j)}$ is the return loss weighting coefficient;
- RL_j is the specified return loss value (in dB);
- $RL_m^{(j)} = RL_m^{(j)}(f_m^{(j)}, \bar{x})$ is the actual return loss value calculated at the frequency $f_m^{(j)}$ and with the current values of the objective variables.

The similar notations are used in (1) for the other controlled characteristics.

II.3. The Initial Guess

To the authors' knowledge, there are no well established models that can be applied for the preliminary SP synthesis. As in any multivariable optimization routine based on gradient or descent methods, the selection of the initial guess is the most difficult problem. Various approaches can be adopted to overcome this problem. The first of them consists in the electrical scaling of a known SP geometry (for example, from [1] to a new frequency operation band. This approach can be used for a simple configuration representing a stepped septum in a straight square waveguide (as in [1], [3]).

With the SP-CAD, the choice of the invariable polarizer dimensions is based on the following considerations. The square housing size a_{sq} must be such that the cutoff frequency of the TE_{11} and TM_{11} modes in the hollow $a_{sq} \times a_{sq}$ waveguide is between the polarizer operation bands. Preferable size a_{out} for the SP with a square output waveguide is that permits to propagate the higher TE_{11} and TM_{11} modes over the high-frequency band only.

If the SP with a circular output is required, the output diameter D can be chosen using similar considerations. In the last case, the recommended size of square

transformer section a_{tr} is such that the cutoff frequencies of dominant modes in the circular and transformer waveguide section are close to each other. This takes place if $a_{tr} \approx 0.85D$.

A simple way to define the initial septum geometry is to define the ridge gap dimensions according to the linear representation (for example) such as $w_i = a_{sq} (1 - i/(N+1))$, $i = 1, 2, \dots, N$. The lengths of the corresponding waveguide sections can be set as $l_i = (0.4 - 0.5)a_{sq}$.

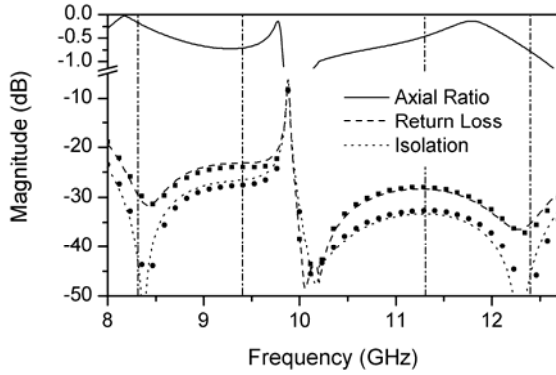
II.4. The Surrogate Models

The SP-CAD allows two options: the optimization can be done either with the *exact numerical models* of all components or with *interpolated models* of the generalized S -matrices of some components (called here "surrogate" models).

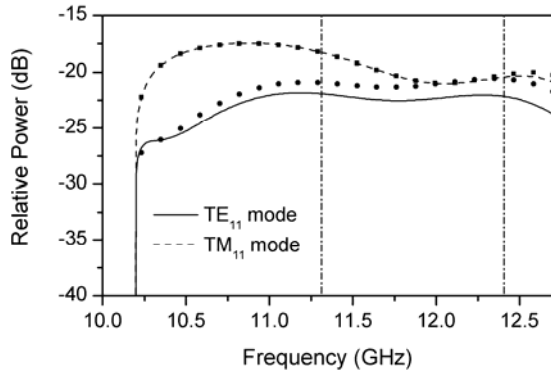
Before starting the optimization process, one-dimensional *frequency buffers* are created for the exact S -matrices of the polarizer components with *fixed geometry*. For example, for a square-to-circular waveguide transition, the buffer is calculated at the given set of frequency points $f_m^{(j)}$ only once, and is not recalculated during the optimization process.

The exact models of polarizer components with *varying geometry* (such as the ridged-to-ridged waveguide junctions) are substituted by their *two-dimensional surrogates*. The latter are obtained by the interpolation of the full-wave S -matrices of the above-mentioned junctions at a given set of sampling points for geometrical parameters at each frequency $f_m^{(j)}$. In this case, the varied geometrical parameters are the sizes of gaps w_n , $n = 1, 2, \dots, N$ of adjacent ridged waveguide sections. The calculation of the database for the surrogate models is a time-consuming procedure, but once the database is created, the overall CPU time used for the polarizer optimization is considerably reduced. The database is stored in files and can be used repeatedly to optimize polarizers differing only by the parameters a_{tr} and/or D .

The program can operate in various accuracy modes. The low-accuracy mode with using the surrogate models allows a rough evaluation of a certain SP topology. This mode is a fast and suitable way for the definition of the initial guess for the final optimization performed in the high-accuracy mode. The frequency



(a)



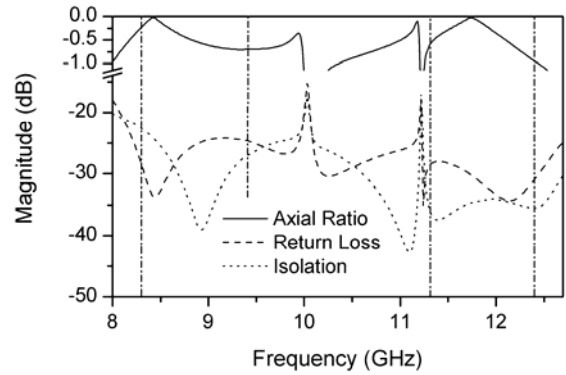
(b)

Fig. 2. Performance of the designed four-step WR-90 septum polarizer with a square output waveguide and comparison with the WASP-NET analysis. Dimensions (in millimeters): $a_{inp} = 22.86$, $b_{inp} = 10.16$, $a_{sq} = 20.8$, $l_{rw} = 5.39$, $t = 1.5$, $w_1 = 17.23$, $l_1 = 9.03$, $w_2 = 13.85$, $l_2 = 9.53$, $w_3 = 10.48$, $l_3 = 8.46$, $w_4 = 4.83$, $l_4 = 3.72$, $a_{out} = 20.8$.

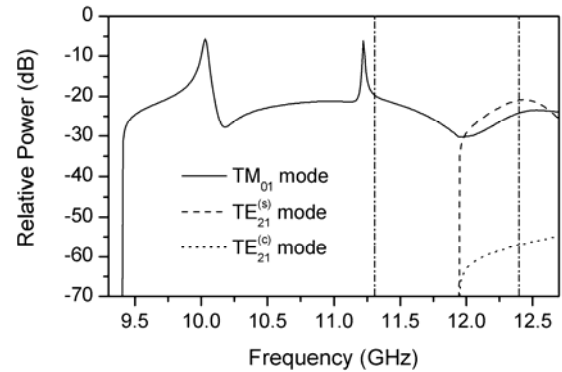
analysis of the optimized SP is performed with using the exact numerical models of all the SP components in the chosen accuracy mode.

III. SOME RESULTS OF THE SP DESIGN

The SP-CAD program has been successfully applied in the design of polarizers having a square or circular output waveguide. The results for four-step optimized polarizers operating in several frequency ranges are presented in Figs. 2 to 5. They have been analyzed with the high-accuracy exact model under the SP dimensions shown in the figures captions. The SP operation bands are delimited in the figures by the vertical dashed-dotted lines. Figures marked as “(a)” show the axial ratio (AX), return loss (RL), and isolation (IS) polarizers performance whereas the “(b)” figures characterize the relative powers (suppression levels (SL)) of unwanted



(a)



(b)

Fig. 3. Performance of the designed four-step WR-90 septum polarizer with a circular output waveguide. Dimensions (in millimeters): $a_{inp} = 22.86$, $b_{inp} = 10.16$, $a_{sq} = 20.5$, $l_{rw} = 4.1$, $t = 1.5$, $w_1 = 17.11$, $l_1 = 9.77$, $w_2 = 14.03$, $l_2 = 10.16$, $w_3 = 10.68$, $l_3 = 8.35$, $w_4 = 4.57$, $l_4 = 3.45$, $l_{sq} = 5.8$, $a_{tr} = 21.6$, $l_{tr} = 8.48$, $D = 24.4$.

higher-order modes in the SP output.

The optimization of all the SPs has been carried out with the following specification within two bands:

- return loss $RL \leq -20$ dB;
- isolation between the input waveguides $IS \leq -25$ dB;
- axial ratio (calculated from the dominant modes amplitudes in the SP output) $AR \geq -1$ dB;
- higher-order mode suppression level $SL \leq -20$ dB.

Figs. 2(a)-(b) show the predicted performances of the optimized square-output polarizer designed for two bands, 8.3 GHz - 9.4 GHz and 11.3 GHz - 12.4 GHz. Input ports are the WR-90 waveguides. The resulting characteristics are close to the specified ones within both bands. For comparison purposes, the numerical data obtained with WASP-NET program, described in

[14], and [15], are plotted by symbols in Figs. 2(a)-(b) as well. Good agreement between data obtained with two programs is evident. This is mainly due to the fact that both programs are based on the mode-matching technique and the calculations were carried out with the same frequency, $f_{\max} = 72$ GHz, limiting maximal cutoff frequencies of modes in ports of all the key-elements. Some differences at high frequencies are due to the following reasons. First, two programs uses the different algorithms in the calculation of the ridged waveguide modal basis. In addition, the number of modes taken into account between any connected discontinuities was set as twenty in the SP-CAD program when using the S -matrix technique. In the WASP program, this number is determined indirectly: all modes in connecting waveguide sections with cutoffs $f_{\text{con}} \leq f_{\max}$ are taken into account. The WASP results in Fig. 2 were calculated at $f_{\text{con}} = 0.55f_{\max}$.

A characteristic feature of the frequency responses shown in Fig. 2(a) is a sharp resonance at $f = 9.88$ GHz. It shows up before the cutoff frequency of the TE_{11} and TM_{11} modes ($f_{\text{cut}} \approx 10.19$ GHz) in the output waveguide (see Fig. 2(b)). When passing this frequency point, the TE_{10} mode transmission coefficient and axial ratio response decrease drastically and the differential phase shift exhibits a sharp jump. It is the resonance effect that limits the widths of the polarizer operation bands. This effect is due to the resonance of the first higher quasi- TE_{11} mode that propagates in the ridged waveguide sections and does not propagate in the input and output waveguides. Similar resonances are named as *resonances on higher "ghost" (or "closed") modes* and have been studied in the literature (see, for example, [16], [17]). The discussed resonance has been experimentally observed in [3] and specially noted in [5] when analyzing single-band SPs. It is an inherent feature of the SPs and cannot be avoided. One can only control the resonance frequency value by a proper choice of the SP size a_{sq} .

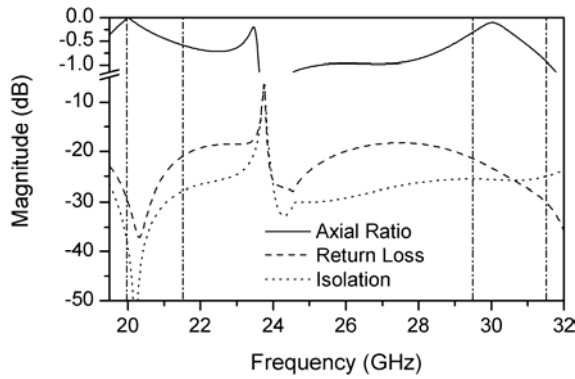
The results for the optimized WR-90 SP with a circular output waveguide are shown in Fig. 3. The return loss, isolation, and axial ratio responses meet the specification over the two specified bands practically (see Fig. 3 (a)). The circular output diameter for this SP is chosen so that the parasitic TM_{01} mode cutoff ($f_{\text{cut}} = 9.41$ GHz) is outside the low-frequency band and the TE_{21} cutoff ($f_{\text{cut}} = 11.94$ GHz) is within the high-frequency band. The curves of the parasitic mode powers are shown in Fig. 3(b). There are two TE_{21}

modes, $TE_{21}^{(s)}$ and $TE_{21}^{(c)}$, which transversal field components are orthogonal and rotated by 45° relative to each other. Here, the superscript s or c denotes the $\sin n\varphi$ or $\cos n\varphi$ polar-angle function, respectively, in the Herz vector representation for the modes in a circular waveguide. It is remarkable that the level of the $TE_{21}^{(s)}$ mode is considerably higher than the $TE_{21}^{(c)}$ one. This is caused by that the $TE_{21}^{(s)}$ mode is efficiently excited by the TE_{11} mode propagating in the SP square waveguide sections because both these modes have similar field distributions.

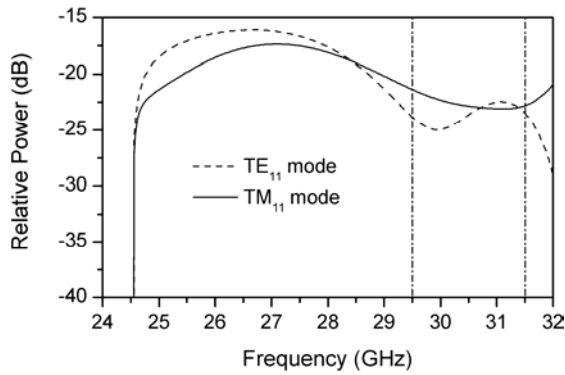
In contrast to the polarizer with a square output, the frequency responses in Fig. 3 (a) have two resonances. The first of them has the same nature as that in Fig. 2 (a). The second resonance appears before the beginning of high-frequency band. It is caused by the transformer square section TE_{11} mode coupled with the $TE_{21}^{(s)}$ mode in the circular output waveguide and playing a role of that closed in the SP cavity. This resonance is a reason of an increased level of the TM_{01} mode before the high-frequency band (see Fig. 3 (b)). To shift the resonance to a lower frequency, a larger output diameter has to be chosen. However, in this case the TM_{01} mode starts to propagate within the low-frequency band that is not acceptable for some SP applications. A similar resonance peak does not appear before the TM_{01} mode cutoff. This mode is excited by the TM_{11} mode of the transformer square section with the cutoff frequency higher than the TM_{01} one. In this case, there are no closed modes and a resonance has not to be appeared, [17]. The aforementioned resonances can lead to some difficulties in designing the SP with a circular output port at a smaller separation between two bands.

The separation between the bands of the aforementioned polarizers is 46% with respect to the total SP operation range and both these bands are within the WR-90 waveguide frequency range. Figs. 4 and 5 demonstrate the SP-CAD capabilities in designing the millimeter-wave polarizers provided with the input WR-34 rectangular waveguides and operating over the bands 20 GHz - 21.5 GHz and 29.5 GHz - 31.5 GHz. The SPs have been designed under the performance specification identical to that for the WR-90 polarizers. The separation between the bands already is about 70%. It should be noted that the low-frequency SP band is entirely outside of the standard frequency range (22 GHz-33 GHz) of the WR-34 waveguide.

The square-output SP performance shown in Figs. 4



(a)



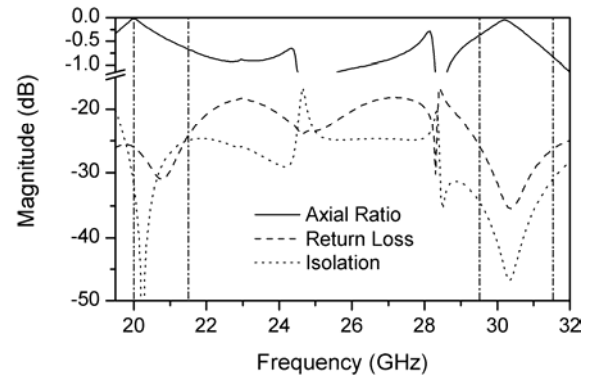
(b)

Fig. 4. Performance of the designed four-step WR-34 septum polarizer with a square output waveguide. Dimensions (in millimeters): $a_{inp} = 8.636$, $b_{inp} = 4.318$, $a_{sq} = 8.636$, $l_{rw} = 8.70$, $t = 1.0$, $w_1 = 7.10$, $l_1 = 3.45$, $w_2 = 5.90$, $l_2 = 3.84$, $w_3 = 4.61$, $l_3 = 3.73$, $w_4 = 2.58$, $l_4 = 1.63$, $a_{out} = 8.636$.

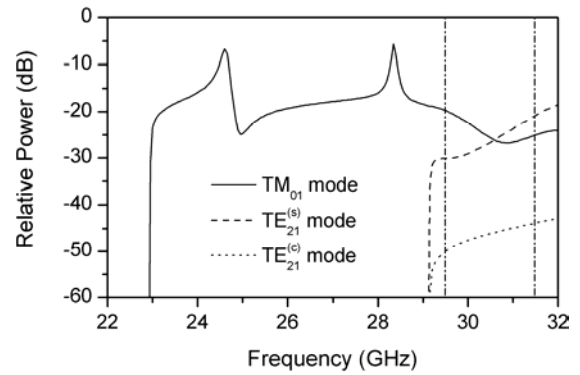
(a)-(b) meet the specifications over two bands. The designed circular-output SP has the characteristics close to the specified ones as well (see Fig. 5). This follows partly from a fact that the bands are widely separated and the second resonance is sufficiently far from the beginning of high-frequency band in contrast to the SP of Fig. 3.

IV. THE ANALYSIS OF POLARIZER WITH CORRUGATED HORN

Though the above-discussed higher-order modes are low in power, the following question has to be studied specially: how do they influence the resulting axial ratio value in the SP output? As an example, let us consider the SP illustrated by Fig. 3. For this SP, one (TM_{01}) or



(a)



(b)

Fig. 5. Performance of the designed four-step WR-34 septum polarizer with a circular output waveguide. Dimensions (in millimeters): $a_{inp} = 8.636$, $b_{inp} = 4.318$, $a_{sq} = 8.40$, $l_{rw} = 9.27$, $t = 1.0$, $w_1 = 6.88$, $l_1 = 3.52$, $w_2 = 5.63$, $l_2 = 3.65$, $w_3 = 4.34$, $l_3 = 3.40$, $w_4 = 1.95$, $l_4 = 1.43$, $l_{sq} = 1.07$, $a_{tr} = 8.6$, $l_{tr} = 2.57$, $D = 10.0$.

three (TM_{01} , $TE_{21}^{(c)}$, and $TE_{21}^{(s)}$) higher-order modes can propagate in the circular output over the 11.3 GHz – 11.94 GHz or 11.94 GHz – 12.4 GHz subbands of the high-frequency band, respectively (see Fig. 3 (b)).

We will further emphasize the second subband because of the greater number of higher-order propagating modes there. One can see that within this subband the TM_{01} and $TE_{21}^{(s)}$ modes are excited with comparable amplitudes that are essentially higher than the $TE_{21}^{(c)}$ mode one. However, these modes have the field component distributions and propagation constants differing from each other and from those of the dominant $TE_{11}^{(s)}$ and $TE_{11}^{(c)}$ modes. This will lead to a different axial ratio of the polarization ellipse of the

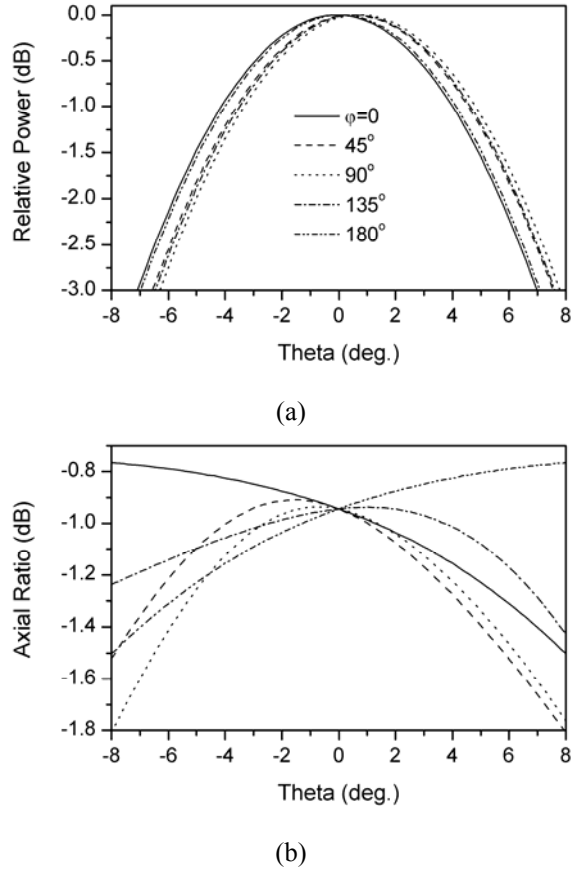


Fig. 6. The radiation (a) and polarization (b) patterns of the cascade consisting of the septum polarizer and corrugated conical horn.

entire field, i.e. including all the propagating higher-order modes, calculated at an arbitrary point of the SP circular output cross-section and at different distances from the output beginning. The axial ratio at any point of the output waveguide axis has to be equal to that calculated from the dominant modes amplitudes because the electrical field components of the considered higher-order modes are zero at the axis.

Due to the aforementioned entire field properties, it is difficult to obtain a certain answer to the above-put question. Such a conclusion is valid for the first subband with one high-order TM_{01} mode as well. More objective information can be obtained from the analysis of far field radiation and polarization patterns for a cascade of the septum polarizer and corrugated horn. A dual-band corrugated conical horn has been previously designed for two frequency bands identical to those for the polarizer of Fig. 3 using a numerical procedure reported in [18]. The horn is characterized by the following parameters: input waveguide diameter

$D_{inp} = 24.4$ mm, aperture diameter $D_{horn} = 132$ mm, semi-flare angle $\alpha = 15^\circ$, throat circular waveguide section of the diameter D_{inp} and the length l . Eight modes are taken into account in this section. It should be noted that the value of l influences essentially the radiated field characteristics.

The radiation and polarization patterns of the polarizer-horn cascade with $l = 8.7$ mm are shown in Fig. 6(a) and 6(b), respectively. They are computed at $f = 12.4$ GHz for several φ -planes within the 3-dB θ -angle sector. At the considered frequency, the polarizer has the worst axial ratio value $AX = -0.94$ dB calculated from the dominant modes amplitudes and comparable amplitudes of the propagating TM_{01} and $TE_{21}^{(s)}$ higher-order modes (see Fig. 3). Just these modes result in a deviation of the radiation pattern maximum (up to $\Delta\theta = 0.8^\circ$ at $\varphi = 90^\circ$) from the axial direction $\theta = 0$ (Fig. 6(a)) and in an asymmetry of the polarization patterns in different φ -planes (Fig. 6 (b)). As expected, the axial ratio curves intersect at the point $\theta = 0$ for all the φ -planes on the level equal to that for the polarizer (compare Fig. 3 (b) at $f = 12.4$ GHz and Fig. 6 (b) at $\theta = 0$). This is because the fields of higher-order modes do not make a contribution to the polarization patterns in the axial direction $\theta = 0$. The symmetry condition of type $F(\varphi, \pm\theta) = F(180^\circ + \varphi, \mp\theta)$ is carried out for the relative power and axial ratio dependences on θ (for example, see curves for $\varphi = 0$ and $\varphi = 180^\circ$ in Fig. 6(a) and 6(b)).

One would expect that the similar features are valid for the radiation and polarization patterns of SPs with a square output as well.

V. CONCLUSION

The results presented in this paper show the capabilities of the SP-CAD program as a tool for efficient and accurate design of compact waveguide septum polarizers terminated with square or circular output waveguides and operating in two distant frequency bands. The SP-CAD produces results that are in good agreement with those calculated with an extensively validated electromagnetic solver. The nature of the resonance effects limiting the bandwidths of different polarizer configurations is discussed. The influence of propagating higher-order modes on characteristics of the far field radiated from a corrugated conical horn terminating a polarizer is analyzed. It is found that

higher-order modes produce a deviation of the radiation pattern maximum and an asymmetry of the polarization pattern relative to the axial direction.

ACKNOWLEDGMENT

The authors would like to thank Prof. F. Arndt, University of Bremen, Germany, for his kind contribution in analyzing the septum polarizers with WASP.

REFERENCES

- [1] Chen M.H. and G.N. Tsandoulas, "A wide-band square-waveguide array polarizer," *IEEE Trans. Antennas Propag.*, vol. 21, pp.389-391, May 1973.
- [2] Ege T. and P. McAndrew, "Analysis of stepped septum polarizers," *Electron. Lett.*, vol. 21, pp. 1166-1168, Nov. 1985.
- [3] Esteban J. and J.M. Rebolgar, "Field theory CAD of septum OMT-polarizer," in *1992 IEEE AP-S Int. Symp. Dig.*, pp. 2146-2149.
- [4] Ihmels R., U. Papziner, and F. Arndt, "Field theory design of a corrugated septum OMT," in *1993 IEEE MTT-S Int. Microwave Symp. Dig.*, pp. 909-912.
- [5] Bornemann J. and V. Labay, "Ridged waveguide polarizers with finite and stepped-thickness septum," *IEEE Trans. Microwave Theory Techn.*, vol. 43, pp.1782-1787, Aug. 1995.
- [6] Bornemann J. and S. Amari, "Septum polarizer design for antenna feeds produced by casting," in *1997 IEEE AP-S Int. Symp. Dig.*, pp. 1422-1425.
- [7] Piovano B., G. Bertin, L. Accatino, and M. Mongiardo, "CAD and optimization of compact wide-band septum polarizers," in *Proc. 29th Europ. Microwave Conf.*, vol. 3, Munich, Germany, Oct. 1999, pp. 235-238.
- [8] Bouki-Hacene N., J. Sombrin, and A. Papiernik, "Approximation by Gegenbauer polynomials in the study of a rectangular ridged waveguide. Application to the analysis of a waveguide septum polarizer," *Int. J. Numerical Modeling*, vol. 16, pp. 299-318, Apr. 2003.
- [9] Beyer R. and F. Arndt, "Efficient hybrid mode-matching/-finite-element (MM/FE) method for the design of waveguide components and slot radiators," in *1998 IEEE MTT-S Int. Microwave Symp. Dig.*, pp. 1275-1278.
- [10] Kirilenko A.A., D.Yu. Kulik, L.A. Rud, V.I. Tkachenko, and N. Herscovici, "Compact septum polarizers with a circular output waveguide," in *Proc. 5th Int. Kharkov Symp. Physics and Engineering of Microwave, MM, and SubMM Waves, MSMW'04*, Kharkov, Ukraine, June 2004, pp. 686-688.
- [11] Kirilenko A., D. Kulik., L. Rud, V. Tkachenko, and N. Herscovici, "CAD of double-band septum polarizers," in *Proc. 34th Eur. Microwave Conf.*, Amsterdam, Netherlands, Oct. 2004, pp. 277-280.
- [12] Kirilenko A., D. Kulik, Yu. Parkhomenko, L. Rud., and V. Tkachenko, "Automatic electromagnetic solvers based on mode-matching, transverse resonance, and S-matrix technique," in *Proc. XIV Int. Conf. Microwaves, Radar and Wireless Communications, MICON-2002*, Gdansk, Poland, May 2002, pp. 815-824.
- [13] Kirilenko A.A., L.A. Rud, and V.I. Tkachenko, "CAD of evanescent-mode band-pass filters based on the short ridged waveguide sections," *Int. J. RF Microwave CAE*, vol. 8, pp.354-365, Nov. 2001.
- [14] MIG, Microwave Innovation Group, "A CAD tool utilizing fast hybrid MM/FE/MoM/FD techniques," *Microwave Journal*, vol. 45, 178-180, Sept. 2002.
- [15] Arndt F., J. Brandt, V. Catina, J. Ritter, I. Rullhusen, J. Dauelsberg, U. Hilgefert, and W. Wessel, "Fast CAD and optimization of waveguide components and aperture antennas by hybrid MM/FE/MoM/FD methods – state-of-art and recent advances," *IEEE Trans. Microwave Theory Techn.*, vol. 52, pp. 292-302, Jan. 2004.
- [16] Jaynes E.T., "Ghost modes in imperfect waveguides," *Proc. IRE*, vol. 46, pp. 416-418, Feb. 1958.
- [17] Shestopalov V.P., A.A. Kirilenko, and L.A. Rud', *Resonance Wave Scattering. Vol. 2. Waveguide Discontinuities*. Kiev: Naukova Dumka, 1986, ch. 4, 5.
- [18] Perov A., L. Rud, S. Senkevich, and V. Tkachenko, "Automated design of corrugated conical horns for dual-band applications," in *Proc. 10th Int. Conf. Mathematical Methods in Electromagnetic Theory, MMET-04*, Dnepropetrovsk, Ukraine, Sept. 2004, pp. 478-480.



Anatoliy A. Kirilenko was born in Tambov, Russia, in 1943. He was graduated from the Radiophysics Department of the Kharkov State University, Ukraine, in 1965. He received the Ph.D. and D.Sc. degrees from the Kharkov State University, in 1970 and 1980, respectively, and Professor title in radiophysics from the Academy of Sciences, USSR, in 1989. Since 1965, he has been with the Institute of Radiophysics and Electronics, National Academy of Sciences of Ukraine, Kharkov, where he is currently a Head of the Department of Computational Electromagnetics. Since 1981, he is a Professor of the National Aerospace University, Kharkov. His research interests are analytical and numerical methods in electromagnetics, resonance phenomena in waveguides and gratings, microwave CAE and CAD. Prof. Kirilenko is a Winner of the 1989 State Prize of Ukraine in the field of Science and Technology and a recipient of the 1991 award for the best software in the field of microwave electronics in the former USSR.



Dmitriy Yu. Kulik was born in Kharkov, Ukraine, in 1965. He received the Radioelectronics Engineering degree from the Kharkov Aviation Institute, in 1988 and Ph.D. degree in radiophysics from the Institute of Radiophysics and Electronics, National Academy of Sciences of Ukraine, Kharkov, in 2003. From 1988 to 1993, he was with the Radar Department, from 1993 to 1998, with the Center of Remote Sensing of Earth, and since 1998, with the Department of Computational Electromagnetics of the Institute of Radiophysics and Electronics, where he is currently a Researcher Scientist. His research interests are a computer simulation of microwave devices, development of the software for designing waveguide filters and diplexers.



Leonid A. Rud was born in the Donetsk region, Ukraine, in 1946. He received the Radiophysics Engineering degree from the Kharkov Institute of Radioelectronics, in 1964, Ph.D. and D.Sc. degrees in radiophysics from the Kharkov State University, in 1976 and 1990, respectively, and the Senior Scientist title in radiophysics from the Academy of Sciences, USSR, in 1984.

Since 1971, he has been with the Institute of Radiophysics and Electronics, National Academy of Sciences of Ukraine, Kharkov, where he is currently a Leading Scientist of the Department of Computational Electromagnetics. His research interests include the mathematical simulation of wave scattering from waveguide discontinuities, spectral theory of open waveguide resonators, CAD of waveguide and antenna components, frequency-selective devices. Dr. Rud is a Winner of the 1989 State Prize of Ukraine in the field of Science and Technology.



Vladimir I. Tkachenko was born in Lviv, Ukraine, in 1951. He received the Researcher and Ph.D. degrees in radio-physics from the Kharkov State University, in 1973 and 1986, respectively. From 1973 to 1981, he was with the Low Temperature Physics Institute, National Academy of Sciences of Ukraine, Kharkov, where he was involved in the development of superconductive antennas theory. In 1981, he joined the Institute of Radiophysics and Electronics, the National Academy of Sciences of Ukraine, Kharkov, where he is currently a Senior Scientist of the Department of Computational Electro-magnetics. From 1991 to 1996, he was an Assistant Professor at the Kharkov State Technical University of Radioelectronics. His research interests are numerical algorithms and software for the design of microwave devices and large-scale modeling software for the waveguide systems. Dr. Tkachenko is a recipient of the 1991 award for the best software in the field of microwave electronics in the former USSR.



Naftali Herscovici was born in Bucuresti, Romania, in 1954. He received his B.Sc., M.Sc. from the Technion, Haifa, Israel and his Ph.D. from the University of Massachusetts, Amherst, in 1978, 1985 and 1992, respectively. Between 1982 and 1989 he was employed by Rafael, Haifa, Israel as an Antenna Research Engineer; there he was engaged in research and development of microwave antennas. He is currently the Director of the Antenna Department at Atlantic Microwave, Bolton, MA USA. He is the author of over 50 technical papers in various journal and conference publications. His research interests include microstrip antennas and arrays, reflector antennas and feeds, pattern synthesis and antenna modeling.

The Influence of Data Density on the Consistency of Performance of the Feature Selective Validation (FSV) Technique

Alistair Duffy*, Antonio Orlandi†

* De Montfort University, Leicester, UK

† UAq EMC Laboratory, University of L'Aquila, L'Aquila, Italy

contacts: apd@dmu.ac.uk, orlandi@ing.univaq.it

ABSTRACT — The human visual system has an immense capacity for compensating for poor or incomplete data. Psycho-visual coding schemes make use of the brain's ability to extrapolate and interpolate independently of conscious awareness to reduce data (bit) rates but maintain the same level of 'information' within a video signal. However, when attempting to produce a simple method for comparing data-sets, primarily for validation of computational electromagnetics, could give rise to a problem. Namely that someone undertaking the visual inspection of (e.g.) modeled data against experimental data will see the same picture whether sampled at N , $100N$ or $0.01N$ data points whereas the software undertaking the comparison would process three very different data sets. The Feature Selective Validation (FSV) method was developed to attempt to mimic the group response of a number of experts undertaking the visual comparison. Hence, the quality of performance of the FSV method should not be severely affected by the number of data points if this assertion is to hold, despite the obvious potential for variation. This paper investigates the FSV performance as a function of data density and shows that the accuracy of its performance remains largely unimpeded by variations in the precision of the data supplied.

I. INTRODUCTION

In order for this paper to investigate the effect of data density on the FSV method, it needs to consider two issues. The first is to review the FSV method, clarifying what data is being used (including what this paper considers as data density), how it is being used, why and how the data density impacts on the underlying equations. The second factor is how does a normal graphical representation of data differ from how the data is presented to the FSV method. This section will overview the FSV method and the issues surrounding graphical representation and then lead on to a more detailed review of the FSV heuristics and then to tests to ascertain the quality of performance of the FSV method.

1.1. FSV OVERVIEW

A typical scenario for the validation of computational electromagnetics involves the modeling of a system that can be directly measured. The resulting pair of data sets are then presented graphically to those involved in this exercise who will ascribe a quality level to the comparison: such as 'good'. Closer inspection may add a qualifier to this descriptor: such as 'good, but...'. The Feature Selective Validation (FSV) method was conceived as a technique to support this exercise, providing a numerical value to the quality of a comparison constructed from components analogous to the general approach used by humans. Namely, comparing the trends of the two data sets and comparing the individual features, perhaps resonant features, and combining these to give an overall confidence in the goodness of fit. The reason for the development of FSV over using existing methods, such as correlation, was that the existing methods do not offer sufficient discrimination or potential for feedback to the users.

The basis for the FSV method is to low pass and high pass filter the original two data sets, take differences of the low pass data to give the Amplitude Difference Measure (ADM) and take a mix of differences of derivatives of the low and high pass data to give the Feature Difference Measure (FDM). These represent the trend / envelope difference and the resonant-type feature difference discussed earlier. These are then treated as independent components and a Global Difference Measure (GDM) obtained from the ADM and FDM. More detail is given in section 2 and in references [1 – 3].

1.2. REPRESENTATION ISSUES

When a set of measurements is taken and represented graphically, it is usual to present the data with lines joining the points, as in Figure 1.

Figure 2 shows the same data but represented more in the manner that a computer would 'see' it.

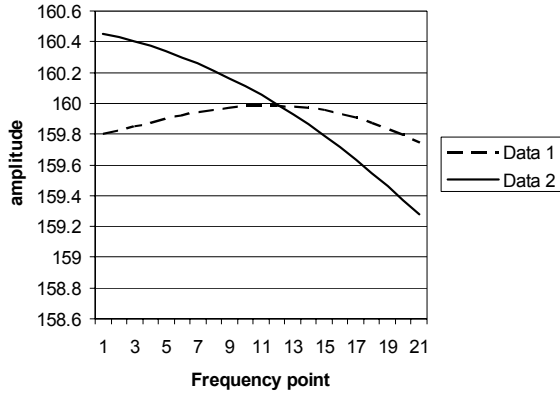


Figure 1. Normal presentation of data using lines.

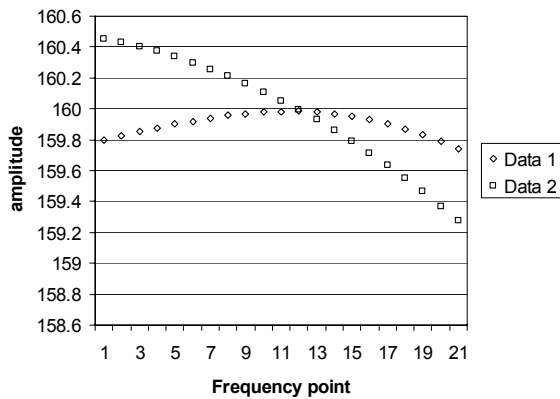


Figure 2. "Non-interpolated" presentation of data.

While we look at continuous lines on a graph, the computer ‘sees’ points (more correctly a table of numbers). The presence of lines gives a sense of certainty to the locations in both ordinate and abscissa, however, representation as points shows the possibility of uncertainty in the location. While this is a trivial example, it can be seen that having fewer points on a graph increases the uncertainty, but presents less noise in the form of high frequency components. However, more data points increases the precision of the data but increases the noise present. Effectively, manipulating the number of data points may have virtually no effect on the visual representation of the data but will have a substantial effect on the data presented for analysis; for example halving the number of data points reduces the amount of data available for analysis by 3 dB but results in virtually no difference in the visual effect.

1.3. PURPOSE OF STUDY

Bringing together the two themes discussed so far we can see that the use of a tool like the FSV method for the validation of CEM should, as far as possible, predict the response of a large group of users. By doing this, a

level of confidence can be attributed to the quality of the comparison. The response of the large group of users will be done ‘by-eye’ based on lines on a graph, suggesting continuous functions, further implicitly suggesting a level of precision that may not be realistically expected from the data. However, the response of the computer program will be obtained by following a clear and predetermined algorithm based on discrete points, i.e. non-continuous functions with the implication of uncertainty between these points.

Hence, the purpose of, and the research question for, this study is to see if varying the number of points presented to the FSV method will leave the output relatively unchanged, and certainly in line with user opinion. From this, it may be possible to issue some guidelines recommending good practice in the use of the FSV method so as to ensure a high level of consistency between applications.

There is the further issue that should be considered regarding the fact that as the number of data points used to represent the systems being compared is increased or decreased, the information content is either increased or decreased, the precision in the data (i.e. the tolerance of each point along the *x* axis) varies and the noise content (or aliasing effect due to sampling effects) varies. Hence, while comparing data with, for example, 400 points in one instance and 100 points in another instance, may look identical, they are clearly separate sets of results. Issues surrounding data density and the veracity of the conclusions to be drawn from this are common in other walks of engineering (e.g. [4, 5]).

The next section will review the mathematics behind the FSV method and this will be followed by the tests to address the research question set out above.

II. THE FSV METHOD

The FSV method was outlined above. This section reviews the governing equations and the methods used to represent the FSV output to users.

II.1. FSV EQUATIONS

The governing equations are as follows. Note *x* is the independent variable, Lo_i and Hi_i are the low pass and high pass filtered versions of i^{th} data set $i = 1,2$ (the subscript indicating the data set) and the single and double primes show the first and second derivatives with respect to *x* obtained using a central difference scheme,

$$ADM(x) = \frac{\left| |Lo_1(x)| - |Lo_2(x)| \right|}{\frac{1}{N} \sum_{i=1}^N (|Lo_1(i)| + |Lo_2(i)|)} \quad (1)$$

$$FDM(x) = 2 \left(FDM_1(x) + FDM_2(x) + FDM_3(x) \right) \quad (2)$$

$$FDM_1(x) = \frac{|Lo_1'(x)| - |Lo_2'(x)|}{\frac{2}{N} \sum_{i=1}^N (|Lo_1'(i)| + |Lo_2'(i)|)} \quad (3)$$

$$FDM_2(x) = \frac{|Hi_1'(x)| - |Hi_2'(x)|}{\frac{6}{N} \sum_{i=1}^N (|Hi_1'(i)| + |Hi_2'(i)|)} \quad (4)$$

$$FDM_3(x) = \frac{|Hi_1''(x)| - |Hi_2''(x)|}{\frac{7.2}{N} \sum_{i=1}^N (|Hi_1''(i)| + |Hi_2''(i)|)} \quad (5)$$

$$GDM(x) = \sqrt{ADM(x)^2 + FDM(x)^2} \quad (6)$$

In the summary, single value representations of the ADM, FDM, and GDM are obtained by taking the mean value over the range of x of interest.

Given that a central difference scheme has been used for the derivatives, it is assumed that the data points are evenly spaced. So, from Table I it can be seen that

$$y'(x_4) = (y(x_5) - y(x_3)) / (x_5 - x_3) \quad (7)$$

Table I. Representation of trial data.

Point number	Data value
1	$y(x_1)$
2	$y(x_2)$
3	$y(x_3)$
4	$y(x_4)$
5	$y(x_5)$
6	$y(x_6)$

However, in an undersampled version of this, as indicated in Table II

$$y'(x_4) = (y(x_6) - y(x_5)) / (x_6 - x_5) \quad (8)$$

Table II. Under sampled data of Table I.

Point number	Data value
3	$Y(x_2)$
4	$y(x_4)$
5	$Y(x_6)$

There are two practical implications for using this data in FSV. The first is that where there is a low rate of change in the data, then $y(x_5) - y(x_3) \approx y(x_6) - y(x_5)$ and a high rate of change may render this approximation incorrect. The second point is that in Table II the separation of data points is $2\Delta x$, where Δx is the separation in Table I. However, in the FSV equations employing derivatives, the derivatives appear in both the numerator and denominator of the equations, so the Δx effect will cancel. Of course, this is only true if the Δx used for derivatives of dataset 1 is equal to the Δx used for derivatives of dataset 2. This assumption has been made in this analysis.

This leaves the issue of whether Δy_a is sufficiently close to Δy_b where a and b represent two different sampling rates. This will be implicitly investigated in the next section.

In order to help interpret the results in the next section, methods used to represent the FSV data to users will be reviewed.

II.2. FSV REPRESENTATION

The basic representation of the FSV output can be either simply numeric (i.e. single figure values for the ADM, FDM and GDM) or point-by-point values ($\{A, F, G\}DM(x)$ as in the previous equations). However, one of the design requirements for FSV was to provide a range of diagnostic information [2]. Bearing in mind the aim for the FSV method to mirror the opinions of a group of engineers, it has been found that the proportions of each of the measures that falls into the definitions of the natural language descriptors, given in Table III, provides a useful histogram which is suggestive of the proportions of a large group who, when assessing the original comparisons would categorize them according to the categories [3]. These are called the confidence histograms for each of the measures.

Table III. Natural language descriptors for FSV $\{A, F, G\}DM$.

FSV value (quantitative)	Natural language descriptor
$Value \leq 0.1$	Excellent
$0.1 \leq Value < 0.2$	Very good
$0.2 \leq Value < 0.4$	Good
$0.4 \leq Value < 0.8$	Fair
$0.8 \leq Value < 1.6$	Poor
$1.6 \leq Value$	Very poor

Given that the confidence histograms aim to provide a synthetic group response, a wide spread of similar

height categories would lead to the interpretation that there can be a low confidence in attributing a single epithet to a comparison. For example, if the confidence histogram showed an approximately even distribution between Good, Fair, and Poor, it would be inappropriate to describe the comparison as Fair; it would be better to describe it as Good – Poor. In order to capture this in a more algorithmic manner, the ‘spread’ of the confidence histograms has been introduced [6]. The Spread is the number of categories that contains 85% of the data points (taking the difference between the most and least favourable category). So, for example, if in the previous example, 30% of the points fell into each of the Good, Fair, and Poor categories, then the Spread would be 3. If, on the other hand, approximately half fell into the excellent category and nearly half into the Very Poor category, then the spread would be 6. Effectively, the Spread is a measure of the variance of the histogram data.

In order to balance the Spread, where a Spread of 2 could equally result from a combination of Excellent-Very Good as it could from Poor – Very Poor, a Grade measure has also been introduced alongside the Spread. Whereas the Spread could be thought of as a variance measure, the Grade is similar to an upper action line in process control. The Grade is the number of categories, starting with Excellent that need to be included for 85% of the data points in the particular measure to be counted. Thus, in the Good-Fair-Poor illustration the Grade would be 5; in the Excellent-Very Good illustration, the Grade would be 2 but the Poor-Very Poor illustration would have a Grade of 6. So together, the Grade-Spread gives a simple indication of the quality and reliability of the comparison.

The following analysis uses Grade-Spread in addition to the summary values to quantify the differences that varying the data density has on the comparison results. The results were obtained using a stand-alone FSV application [7, 8].

III. TESTS

In order to assess the performance of FSV when faced with varying data density, tests with three different data types have been performed. These are (1) EMC modelling of a via performance (2) very high feature density performance and (3) sinusoid representations. In doing this (1) is representative of real data that will commonly be presented to FSV, (2) is representative of data at one extreme of complexity and (3) is representative of data at the other extreme of complexity.

III.1. VIA PERFORMANCE

The system was modeled with 5768 points per data set, this is shown in Figure 3, and the data was then down sampled to a minimum of 177 points: Figure 4.

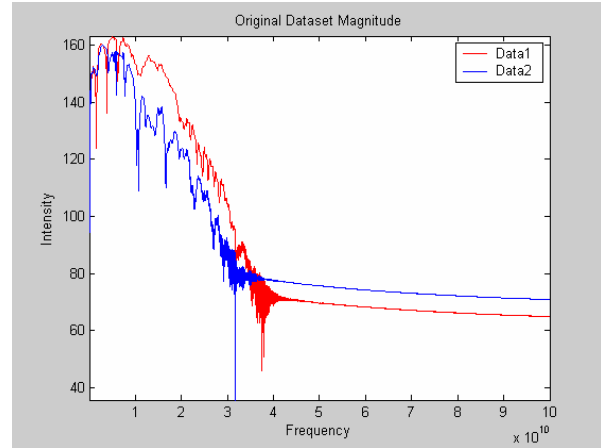


Figure 3. Via models: 5768 samples.

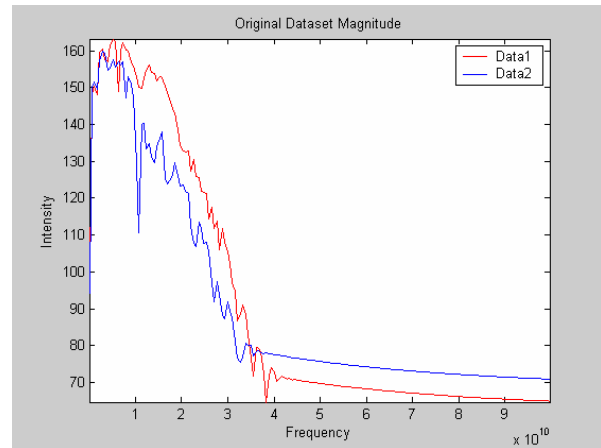


Figure 4. Downsampled data of Figure 3: 177 samples.

Table IV. FSV summary values for various data densities between the representations of Figures 3 and 4.

	ADM	FDM	GDM
No of Data points			
5768	0.165	0.604	0.665
2839	0.152	0.536	0.587
1419	0.139	0.395	0.448
709	0.132	0.321	0.374
384	0.132	0.277	0.332
177	0.140	0.274	0.334

Initial visual observations of this data suggest that the downsampling, as would be expected, has reduced the level of ‘high-Q’ features resulting in an overall visual improvement in the Feature (i.e. the ‘high-Q’ aspect) component of the original data, leaving the Amplitude (i.e. the envelope / trend) information relatively unaffected. The effect of the changes can be seen in Table IV which lists the ADM, FDM and GDM components for various data densities.

From a natural language descriptor equivalent, the ADM is unchanged at Very Good, whereas the GDM has gone from Fair to Good, reflecting a likely visual analysis.

However, in order to address possible researcher bias, the Grade-Spread information, as discussed in Section 2 was noted. For all the data densities, the ADM Grade remained at 3 and the Spread at 3. On the other hand, the Grade for the FDM and GDM was 5 for 5768 points – 709 points inclusive and was 4 for the remaining two comparisons. The Spread was mostly 4 for the FDM and GDM (it did nudge into 5 for the FDM and GDM of 2839 samples and for the FDM of 1419 samples). However, together this data suggests that the FSV routine is only particularly sensitive to the number of data points used as far as the eye is sensitive to the filtering and smoothing effects of the reduction in the number data points used to present the graphs.

III.2. HIGH FEATURE DENSITY

In this test, very highly structured and noisy data was downsampled. Figure 5 gives the original data and Figures 6 and 7 give undersampled versions of this data.

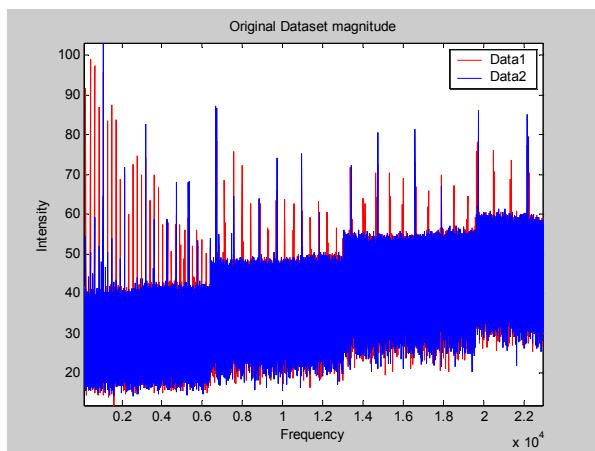


Figure 5. Original data: 3000 samples.

From these three figures, it is clear that the general structure of the data becomes visibly clear once the

original data has been downsampled to 50%. Once the structure has become visibly clearer, it is not immediately obvious what effect the reduction in data density will have on the quality of comparison. Table V gives the Difference Measures for various data densities.

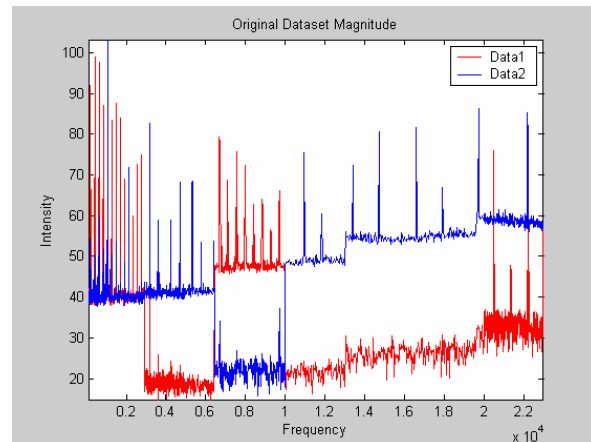


Figure 6. Downsampled data of Figure 5: 1500 samples.

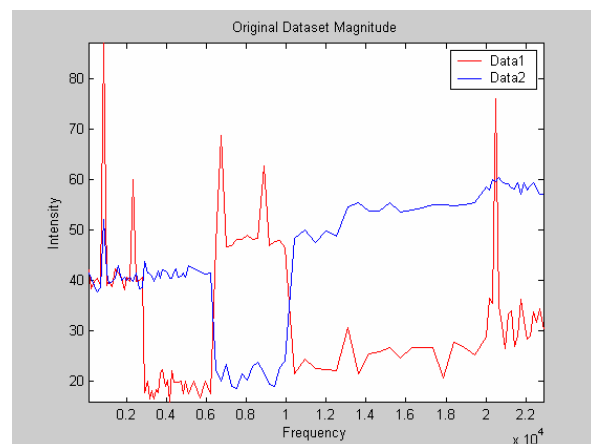


Figure 7. Downsampled data of Figure 5: 97 samples.

Table V. FSV summary values for various data densities between the representations of Figures 5 and 7.

	ADM	FDM	GDM
No of Data points			
3000	0.354	0.609	0.772
1500	0.547	0.681	0.977
750	0.550	0.709	0.995
375	0.521	0.658	0.928
187	0.558	0.649	0.937
93	0.584	0.727	1.027

It is interesting to note that as the graphs become visibly more structured, i.e. moving from Figure 5 to Figure 6, the FSV analysis becomes reasonably constant (below one decimal place). This is interesting because the similarities between Figures 6 and 7 are well defined and there is a high probability that they would be noted as such by most users. However, the similarity between Figures 5 and 6 are not so easy to see.

This observation is also reflected in the Grade-Spread. Excluding the 3000 point comparison, the grade is constant at 5 for the ADM, GDM and FDM for all comparisons except the GDM for 750 and 93 where it tips over to 6. Never-the-less a consistent performance.

For the Spread, the FDM is constant at 5 and the ADM and GDM both go from 4 (1500 sample) to 3 (93 sample). These results reflect the effect of reducing the data density on the visual interpretation, increasing the probability for consistency between users.

So far, the tests have only shown that the FSV method reflects the likely interpretation of the results by expert users because this data is highly structured and, therefore, relatively easy to identify visual changes to the structure of the data. The more demanding task, in these circumstances, is to take a simple structure, which will barely change visually and analyze this with FSV.

III.3. SINUSOIDS

In this final test, two sinusoids were compared after differences were introduced between them. These differences were changing the amplitude so one was 10% of the amplitude of the other and secondly, one was 90% of the amplitude of the other; the final test was to introduce a phase shift between the two curves.

III.3.1. 10% Relative Amplitude

The two curves, one at peak amplitude of 10 V and the other with peak amplitude of 1 V were compared over one period with a range of data points from 50 to 800. The comparison of these curves is illustrated in Figure 8. The summary values for the ADM, FDM and GDM are listed in Table VI.

Clearly, there is a consistency in all the figures. The slight variations in the GDM arise through the point-by-point nature of the summation and are illustrated in the confidence histogram in Figure 9.

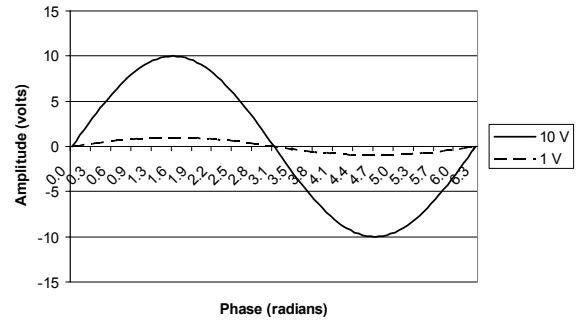


Figure 8. Two sinusoids of very different amplitude.

Table VI. FSV summary values for various data densities for a 10 V and 1 V sinusoid.

	ADM	FDM	GDM
No of Data points			
800	1.091	1.318	1.803
400	1.091	1.318	1.802
200	1.091	1.318	1.811
100	1.091	1.318	1.823
50	1.091	1.318	1.831

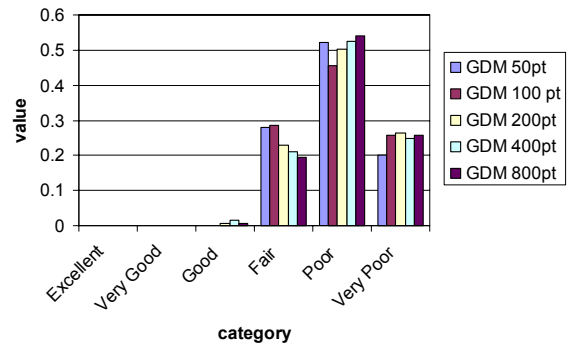


Figure 9. GDM confidence histogram for two sine waves of 10 V and 1 V amplitude.

III.3.2. 90% Relative Amplitude

The same test as in section 3.3.1 was performed, but this time 10 V and 9 V amplitude sine waves were compared, as illustrated in Figure 10. Table VII lists the summary values.

Again, there is practically very little difference in the results, as illustrated with the GDM confidence histogram in Figure 11

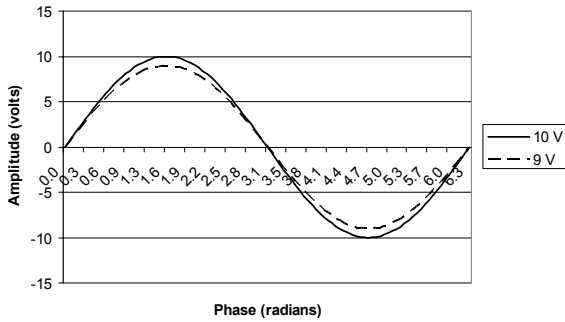


Figure 10. Two sinusoids of similar amplitude.

Table VII. FSV summary values for various data densities for a 10 V and 9 V sinusoid.

	ADM	FDM	GDM
No of Data points			
800	0.071	0.127	0.156
400	0.07	0.102	0.132
200	0.07	0.086	0.118
100	0.07	0.085	0.117
50	0.07	0.085	0.118

The greatest difference that can be seen from this figure is that there has been some shifting between Excellent and Very Good for the 800 point data. This is probably because of the proportion of the GDM at approximately 0.1, i.e. the boundary between the two categories.

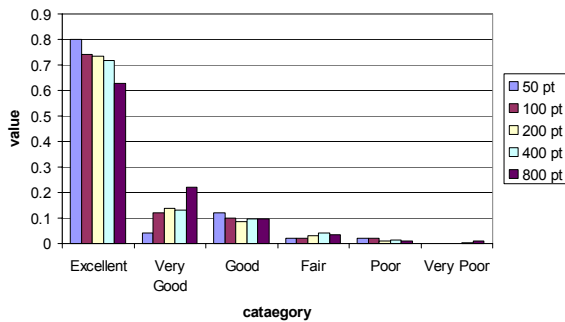


Figure 11. GDM Confidence histogram for two sine waves of 10 V and 9 V amplitude.

III.3.3. Phase Difference

The last of the sinusoidal tests involved taking two similar sinusoids and adding in a one radian phase shift. To add additional difficulty in the tests, the comparison was made over two cycles of the original data with data densities ranging from 10000 points to 20 points. In the case of 20 points, i.e. 10 data points per cycle, the curves clearly depart from smooth sinusoids. The 20 data point curve is shown in Figure 12 and the 100 data point curve, for comparison, is shown in Figure 13.

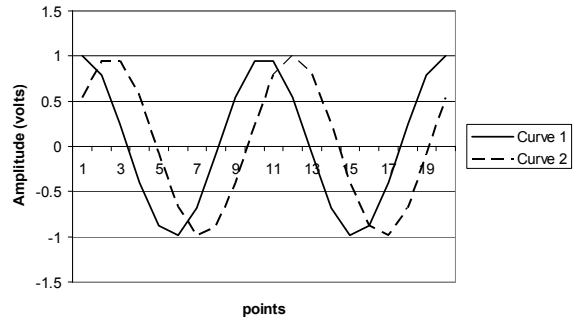


Figure 12. Two poorly defined sinusoids, each with 10 samples per cycle.

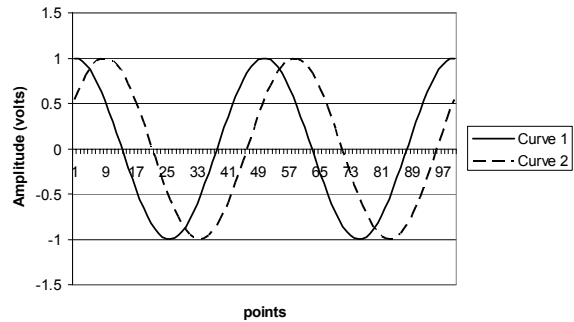


Figure 13. Two well defined sinusoids.

The comparison of the Difference Measure results is given in Table VIII.

Table VIII. FSV summary values for various data densities for two offset sinusoids.

	ADM	FDM	GDM
No of Data points			
10000	0.673	0.894	1.074
1000	0.674	0.689	1.063
100	0.674	0.722	1.094
20	0.712	0.844	1.206

Figure 14 shows the effect of changing the data densities on the GDM.

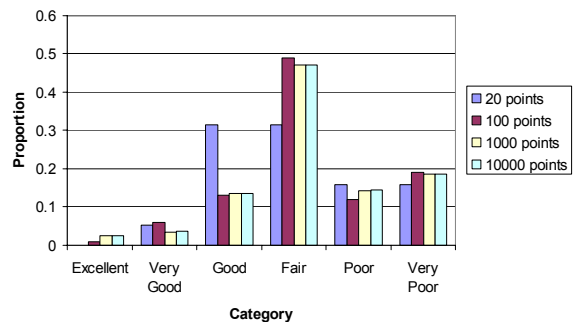


Figure 14. GDM for two offset sinusoids as a function of data density.

Figure 14 shows how consistently the FSV method assesses the comparison of these two data sets.

IV. CONCLUSIONS

This paper has considered the effects of varying data density on the results of FSV analysis of varying data sets.

The FSV method is a promising approach to the formal and quantifiable comparison of data for tasks such as computational electromagnetic (CEM) validation, experimental repeatability and assessment of the amount of change when models are manipulated. However, as part of the validation of FSV itself, its robustness to changes in input data needs to be assessed. This paper has done this with three different, typical data sets, ranging from the structurally trivial (sinusoids) to the structurally highly complex.

The main conclusion that that can be drawn from the results is that FSV is robust in that it does not change the output values appreciably when the input data density changes, providing the data remains visually unchanged. This was clearly seen with the sinusoidal data where the overall levels of agreement did not change substantially once the data density was past the point where it appeared smooth and continuous.

The important general recommendation from this work is that there should be consistency in the number of points used to represent the data and that number should be chosen because of the way in which the data is represented. That is, it is important to choose the correct number of points to represent the data to be compared so that the visual representation is precisely that which needs to be compared. It was clear with the first two examples in this paper that the effective data to be compared could be changed considerably depending on whether more or fewer points were displayed. Clearly, this factor has more of an impact on the assessment of the quality of a comparison than anything else. Perhaps a standard question during validation should be “why has the data been displayed with this level of data density?”

ACKNOWLEDGMENT

The authors are indebted to Professor Charles Bunting (Oklahoma State Univ.) for suggesting this line of investigation and to V. Rajamani (Oklahoma State Univ.), Dr. B. Archambeault (IBM) for the numerous discussions during the research for this paper and Mr. F. Campitelli (*UAq EMC Lab.*) for performing part of the calculations.

REFERENCES

- [1] AJM Martin, *Quantitative data validation (automated visual evaluations)*, PhD Thesis, De Montfort University, UK, 1999.
- [2] AP. Duffy, AJM. Martin, A. Orlandi, G. Antonini, TM. Benson, and MS. Woolfson, “Feature Selective Validation (FSV) for validation of computational electromagnetics (CEM). Part I – The FSV method,” *Submitted to IEEE Transactions on EMC*.
- [3] A. Orlandi, AP. Duffy, B. Archambeault, G. Antonini, D. Coleby, and S. Connor, “Feature Selective Validation (FSV) for validation of computational electromagnetics (CEM). Part II – Assessment of FSV performance,” *Submitted to IEEE Transactions on EMC*.
- [4] G.C. Bishop “Gravitational field maps and navigational errors,” *Proceedings of the 2000 International Symposium on Underwater Technology*, 2000, p 149-54.
- [5] B. Morse, W. Liu, and L Otis, “Empirical analysis of computational and accuracy tradeoffs using compactly supported radial basis functions for surface reconstruction,” *Proceedings - Shape Modeling International SMI 2004*, p. 358-361.
- [6] A. Orlandi, G. Antonini, C. Ritota, and A. Duffy, “Enhancing Feature Selective Validation (FSV) interpretation of EMC/SI results with Grade-Spread”.
- [7] A free, stand-alone, FSV application is available from http://ing.univaq.it/uqemc/public_html/.
- [8] FSV web page at <http://www.eng.cse.dmu.ac.uk/FSVweb>.



Alistair P Duffy (M'93–SM'04) was born in Ripon, UK, in 1966. He obtained a First Class BEng(Hons) degree from University College, Cardiff, in 1988 in Electrical and Electronic Engineering, and the MEng degree the following year. He joined Nottingham University in

1990 receiving a PhD in 1993 for his work on experimental validation of numerical modeling. He also holds an MBA.

He is currently Reader in Electromagnetics and Head of the Division of Engineering at De Montfort University, Leicester, UK and has particular research interests in CEM Validation, communications cabling and technology management. He has published over 100 papers in journals and international symposia.

Dr Duffy is a Fellow of the Institution of Engineering and Technology (IET) and a member of the Chartered Management Institute (CMI). He is active in the IEEE standards activity on the validation of CEM. He is a member of the International Compumag society and the Applied Computational Electromagnetics Society.



Antonio Orlandi (M'90-SM'97) was born in Milan, Italy in 1963. He received the Laurea degree in Electrical Engineering from the University of Rome "La Sapienza", Italy, in 1988.

He was with the Department of Electrical Engineering, University of Rome "La Sapienza" from

1988 to 1990. Since 1990 he has been with the Department of Electrical Engineering of the University of L'Aquila where he is currently Full Professor at the *UAq EMC Laboratory*. Author of more than 100 technical papers he has published in the field of electromagnetic compatibility in lightning protection systems and power drive systems. Current research interests are in the field of numerical methods and modeling techniques to approach signal/power integrity, EMC/EMI issues in high speed digital systems. Dr. Orlandi received the IEEE TRANSACTIONS ON ELECTROMAGNETIC COMPATIBILITY Best Paper Award in 1997, the IEEE EMC SOCIETY TECHNICAL ACHIEVEMENT AWARD in 2003, the IBM SHARED UNIVERSITY RESEARCH AWARD (2004, 2005) and the CST UNIVERSITY AWARD in 2004. He is member of the Education, TC-9 Computational Electromagnetics and TC-10 Signal Integrity Committees of the IEEE EMC Society, Chairman of the "EMC INNOVATION" Technical Committee of the International Zurich Symposium and Technical Exhibition on EMC. From 1996 to 2000 has been Associate Editor of the IEEE TRANSACTIONS ON ELECTROMAGNETIC COMPATIBILITY and now serves as Associate Editor of the IEEE TRANSACTIONS ON MOBILE COMPUTING.

To-Average or Not-to-Average in FDTD Modeling of Dielectric Interfaces

Cynthia Furse, Craig Waterman, and Lance Griffiths

Electrical & Computer Engineering Dept, University of Utah, 50 S Central Campus Dr Rm 3280, Salt Lake City, UT 84112,

Abstract — Accurate Finite Difference Time Domain (FDTD) modeling of localized electromagnetic sources such as cellular telephones near the human body requires very precise modeling of the location of these devices. This paper discusses the effective location of near field sources when dielectric interface cells are made up of either averaged or unaveraged dielectric properties. It is shown that either method can accurately define the proximity between source and dielectric, but that the effective location differs by half an FDTD cell in the two methods.

I. INTRODUCTION

As Finite Difference Time Domain (FDTD) modeling of the human body and other complex dielectric systems becomes main stream [1], [2], many researchers have passionately defined a preference for either averaging or not averaging dielectric materials at boundaries. This paper discusses this issue from the point of view of very near field modeling, where the precise location of a source such as an antenna near the human head is critical to the accuracy of the results. This modeling issue has potentially significant implications in cellular telephone evaluation and the ongoing debate about if power deposition from cell phones is or is not higher in children than in adults [3]. Little or no difference between power absorbed from cellular telephones in adult and child head models is seen if the antenna is modeled an equal distance from the outer surface of both head models [4]. However, if the phone is modeled as being physically closer to the child's head due to the thinner ear of the child, significantly higher power is observed in the child than adult model [5]. This is not surprising, since the fields decrease rapidly (as $1/\text{distance}^3$) very near the antenna, and small changes in the proximity of the phone can result in large changes in power deposition. In addition to the effect of considering or not considering the size of the ear, averaging or not averaging the dielectric properties at the outer surface of the head effectively moves the boundary half a cell, with potentially similar results. When evaluating near field effects such as the power deposition of a cell phone in a human head, it is critical to model the proximity of the source accurately. This requires an understanding of how the choice of averaging or not averaging FDTD dielectric boundaries

affects the effective proximity of the source, which is the topic of this paper.

Several different methods have been used for averaging electrical properties at boundaries of dissimilar media. When a layer of dielectric is thinner than one FDTD cell, averaging is one method of accounting for the thin layer [6]-[10]. Averaging has also been used for boundaries in an effort to reduce unwanted effects from discontinuity of the charge at the boundary [11]-[14]. Interpolation of the fields rather than the model has been proposed as an alternative to averaging [15]. Averaging at the air-dielectric interface of microstrip circuits and antennas has been used routinely [16], [17]. In [18] it was found that averaging was not needed for buried layered structures with no conductor, but that it was helpful when a conductor rested on the air-dielectric interface. Three different types of averaging are used (arithmetic, geometric, and harmonic), and their relative accuracy has been shown to be dependent on the cell size [9], [13]. All of these papers were focused on the effect of the dielectric discontinuity on the model of the dielectric object where the distance between the boundary and source is large enough that a variation of half of an FDTD cell would be negligible. When models of antennas near a dielectric object are considered, the ability of averaging to improve the model is found to be minor, especially when compared to variation in the source location of the antenna [19]. It was also commented in [20] on the effect that averaging can have on displacing the boundary by half a cell.

This paper discusses the effect of averaging on the effective location of a source or boundary and demonstrates that either an averaged and non-averaged dielectric boundary can be used to model the source and boundary in their proper locations. This paper demonstrates the effect of averaging or not averaging the dielectric boundary by considering the phase of the reflection coefficient in front of the boundary. This derivation could have been done analytically as in [2], Section 3.6.8, and the same conclusion could have been drawn.

II. NEAR-FIELD FDTD MODELING

The analysis of modeling the proximity of a source to a dielectric object will be limited in this paper to one dimension in order to precisely demonstrate the effect of

averaging, although the conclusion is easily generalized to 2D and 3D simulations. The one-dimensional TE FDTD grid is shown in Figure 1 for unaveraged cases (a) and (c) and averaged case (b). The locations of two different materials, 1 and 2, in the model are indicated as well as the average of materials 1 and 2 in the center of (b). The location of the physical boundary of each model is indicated by the arrow, as will be shown in the results section.

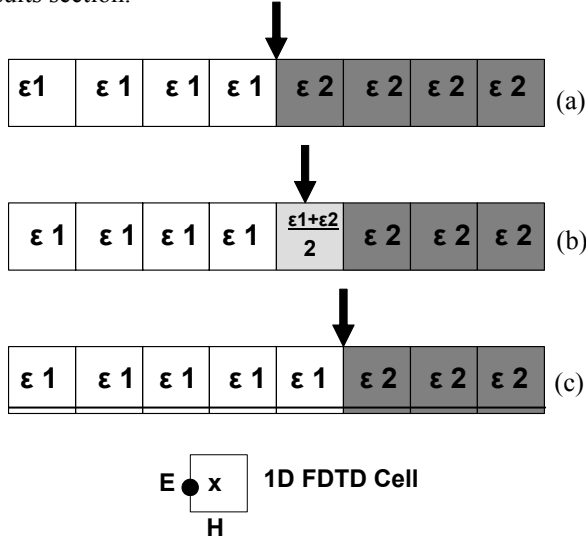


Fig. 1. FDTD model of a dielectric interface; (a) and (c) are unaveraged models, (b) is an averaged model. The location of the physical boundary that each model represents is shown with the arrow. The location of the fields in the 1D FDTD cell are shown as well. The two materials modeled were air ($\epsilon_{r1} = 1$) and "water" ($\epsilon_{r2} = 40.0$). Both materials are lossless.

Maxwell's differential equations in the time domain are

$$\nabla \times \bar{\mathbf{E}} = -\mu \frac{\partial \bar{\mathbf{H}}}{\partial t} \quad (1)$$

$$\nabla \times \bar{\mathbf{H}} = \sigma \bar{\mathbf{E}} + \epsilon \frac{\partial \bar{\mathbf{E}}}{\partial t} \quad (2)$$

They are simplified to two 1D scalar Maxwell's curl equations:

$$\frac{\partial E_y}{\partial t} = \frac{-1}{\epsilon} \left(\frac{\partial H_z}{\partial x} + \sigma E_y \right) \quad (3)$$

$$\frac{\partial H_z}{\partial t} = \frac{-1}{\mu} \left(\frac{\partial E_y}{\partial x} \right) \quad (4)$$

where ϵ in (3) is defined either as averaged (Figure 1b) or unaveraged (Figures 1a and 1c) for cells at the

boundary. For simplicity, $\sigma = 0$ in these test cases. In the non-averaged cases, (a) or (c), ϵ is ϵ_1 or ϵ_2 , depending on the cell. In the averaged case (b), the value of ϵ is ϵ_1 or ϵ_2 on either side of the boundary and the average value of the two materials $(\epsilon_2 + \epsilon_1)/2$ for the boundary cell. It should be noted that this averaged model is the same as modeling a 1-cell thick layer of $(\epsilon_2 + \epsilon_1)/2$ dielectric material sandwiched between two different dielectrics (ϵ_1 and ϵ_2), the boundaries of which would be where the arrows are shown in Figures 1a and c. This is not the most accurate way of modeling a thin layer, however, and is not recommended for applications where the thin layer is expected to have a significant effect on the performance of the system.

To find the phase of the reflection coefficient, the discrete Fourier transform (DFT) of the electric field in every cell was calculated at 1 MHz. This provided the total electric field, E^t . The DFT at each test cell was calculated for each of the three boundary arrangements, and it was also calculated with no dielectric boundary (i.e., with air in all of the cells). The latter gave the DFT of the incident wave alone (E^i), including any effective errors from numerical dispersion. The reflection coefficient at each point can be calculated using

$$\Gamma_\ell = \frac{E^t - E^i}{E^i} \quad (5)$$

where E^t and E^i are the DFTs of the total and incident wave, respectively. Analytical values for the test points were calculated using

$$\Gamma_\ell = |\Gamma| e^{j2\beta\ell}$$

where ℓ is the distance from the center cell (where the arrow is shown in Figure 1a) to the test point and

$$|\Gamma| = \frac{\sqrt{\epsilon_{r1}} - \sqrt{\epsilon_{r2}}}{\sqrt{\epsilon_{r1}} + \sqrt{\epsilon_{r2}}} \quad (6)$$

III. RESULTS

Figure 2 shows a comparison of the phase as a function of distance from the boundary (where the arrow is in Figure 1b) for all three models along with the analytical solution. The uppermost and lowermost lines were produced by the unaveraged models (a) and (c), respectively. The middle line was produced by (b). The analytical value for a boundary at the location of the arrow in Figure 1b is also give. Since the line for the averaged model is halfway between lines for the unaveraged model, we can see that averaging has the effect of shifting the boundary one half-cell away from the source. When the analytical value is calculated at

the location of the arrows shown in Figures 1a and 1c, the match with those curves is as good as that shown here for Figure 1b. The only difference between the averaged and unaveraged models is the phase of the reflection coefficient (which is indicative of the effective location of the dielectric boundary). All three models can properly model the location of the boundary and will give the same phase as the analytical solution if the location of the boundary is taken to be wherever their respective arrows indicate.

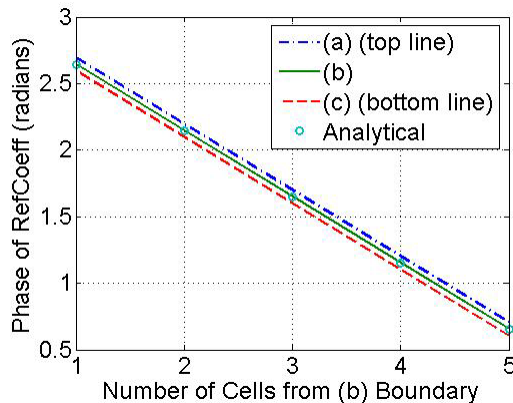


Fig. 2. Phase of reflection coefficient as a function of normalized distance from the (b) boundary (where arrow is seen in Figure 1b). Phase is shown for unaveraged (a and c) and averaged (b) FDTD models. The analytical solution is shown for a boundary where the arrow is shown in Figure 1b. When the analytical solution is calculated relative to the (a) or (c) boundaries (where the arrows are located in Figs. 1a and 1c), it lines up precisely with those lines, instead. This provides proof that both averaged and unaveraged models can be used to accurately model boundaries in FDTD, but that changing the averaging scheme changes the effective location of the boundary.

IV. CONCLUSIONS

Near field FDTD simulations such as models of a cell phone near the human head depend significantly on the proximity of the antenna feedpoint to the head. Properly modeling this requires precise attention to the distance between the source and model, which varies by half a cell depending on if the electrical properties on the boundary are averaged or not. In this paper it was shown that both averaged and unaveraged models can be used with equal accuracy, as long as the model takes into account the location of the boundaries for each case, shown as arrows in Figure 1.

ACKNOWLEDGEMENTS

The authors would like to acknowledge the coding ideas and contributions from Benjamin Yang, Steven Smith, Jeff Spiegel, Darin Patch, Guillermo Oviedo Vela, Aaron Chen, Rodney Earl, Scott Adamson, and Kuncheng Zheng. This paper was initially started as a project in ECE 6340 Numerical Techniques for Electromagnetics and was expanded from there.

REFERENCES

- [1] K.S. Yee, "Numerical solution of initial boundary value problems involving Maxwell's equations in isotropic media," *IEEE Transactions on Antennas and Propagation*, 14 (3), March 1966, pp. 302-307.
- [2] A. Taflove and S. Hagness, *Computational Electro-dynamics: The Finite-Difference Time-Domain Method*, 3 ed., Boston, MA, Artech House, 2005.
- [3] J.C. Lin, "Cellular telephones and children," *IEEE Antennas and Propagation Magazine*, 44 (5), October 2002, pp. 142-145.
- [4] F. Schonborn, M. Burkhardt, and N. Kuster, "Differences in energy absorption between heads of adults and children in the near field of sources," *Health Physics*, 74, 1998, pp. 160-168.
- [5] O.P. Gandhi, G. Lazzi, and C.M. Furse, "Electromagnetic absorption in the human head and neck for mobile telephones at 835 and 1900 MHz," *IEEE Trans. Microwave Theory and Techniques*, MTT-48, 2000, pp. 1118-1126.
- [6] J.G. Maloney, and G.S. Smith, "A comparison of methods for modeling electrically thin dielectric and conducting sheets in the finite-difference time-domain (FDTD) method," *IEEE Trans. Antennas and Propagation*, 41 (5), May 1993, pp. 690-694.
- [7] G. Marrocco, M. Sabbadini, and F. Bardati, "FDTD improvement by dielectric subgrid resolution," *IEEE Trans. Microwave Theory and Techniques*, 46 (12), December 1998, pp. 2166-2169.
- [8] M. Cheluch-Marcysiak, and W.K. Gwarek, "Higher-order modeling of media interfaces for enhanced FDTD analysis of microwave circuits," in *Proc. European Microwave Conf.*, Cannes, France, 1994.
- [9] T. Hirono, et al., "The second-order condition for the dielectric interface orthogonal to the Yee-lattice axis in the FDTD scheme," *IEEE Microwave and Guided Wave Letters*, 10 (9), September 2000, pp. 359-361.
- [10] W.K. Gwarek, "Analysis of an arbitrarily-shaped planar circuit – a time domain approach," *IEEE*

- Trans. Microwave Theory and Techniques*, 33, October 1985, pp. 1067-1072.
- [11] A. Taflove, *Advances in Computational Electrodynamics: The Finite-Difference Time-Domain Method*. Norwood, MA: Artech House, 1998.
- [12] P. Wesseling, *An Introduction to Multigrid Methods*. New York: Wiley, 1992.
- [13] K.-P. Hwang, and A.C. Cangellaris, "Effective permittivities for second-order accurate FDTD equations at dielectric interfaces," *IEEE Microwave and Wireless Components Letters*, 11 (4), April 2001, pp. 158-160.
- [14] E. Luo, and H. O. Kreiss, "Pseudospectral vs. finite difference methods for initial value problems with discontinuous coefficients," *SIAM J. Sci. Comput.*, 20, 1999, pp. 148-163.
- [15] J. Nadobny, et al., "A high-resolution interpolation at arbitrary interfaces for the FDTD method," *IEEE Trans. Microwave Theory and Techniques*, 46 (11), November 1998, pp. 1759-1766.
- [16] X. Zhang, and K.K. Mei, "Time-domain finite difference approach to the calculation of the frequency-dependent characteristics of microstrip discontinuities," *IEEE Trans. Microwave Theory and Techniques*, 36(12), December 1988, pp. 1775-1787.
- [17] C.J. Railton, and J.P. McGeehan, "Analysis of microstrip with rectangular and trapezoidal conductor cross sections," *IEEE Trans. Microwave Theory and Techniques*, 38 (8), August 1990, pp. 1017-1022.
- [18] A. Reineix, and B. Jecko, "Analysis of microstrip patch antennas using finite difference time domain method," *IEEE Trans. Antennas and Propagation*, 37 (11), November 1989, pp. 1361-1369.
- [19] K.S. Nikita, et al., "A study of uncertainties in modeling antenna performance and power absorption of a cellular phone user," *IEEE Trans. Microwave Theory and Techniques*, 48 (12), December 2000, pp. 2676-2685.
- [20] D. Popovic, and M. Okoniewski, "Effective permittivity at the interface of dispersive dielectrics in FDTD," *IEEE Microwave and Wireless Components Letters*, 13 (7), July 2001, pp. 265-267.



Dr. Cynthia Furse, Associate Professor; Electrical & Computer Engineering Department. Dr. Furse received her B.S. in electrical engineering with a mathematics minor in 1985, M.S. degree in electrical engineering in 1988, and her Ph.D. in electrical engineering from the University of Utah in 1994. She is currently an associate professor at the University of Utah and has taught electromagnetics, wireless communication, computational electromagnetics, microwave engineering, antenna design, and introductory electrical engineering. Dr. Furse works to interest young students, particularly women and minorities in engineering and routinely volunteers in Utah's K-12 schools as an engineering mentor, science educator, and engineering career guidance counselor and is active with the Society of Women Engineers, Junior Engineering State, Expanding your Horizons, School-to-Careers, MESA, Girl Scouts and Boy Scouts. Dr. Furse was the Professor of the Year in the College of Engineering at Utah State University for the year 2000. She is the Director of the Center of Excellence for Smart Sensors, an active, funded research program including electromagnetics for biology and remote sensing.



Dr. Lance Griffiths. Dr. Griffiths received his B.S. in electrical engineering with a computer science minor in 1999, and an M.S. degree in electrical engineering in 2002, from Utah State University. He received the Ph.D. in electrical engineering from the University of Utah in 2005. He is currently an RF design/systems engineer at L-3 Communications in Salt Lake City, Utah. Previously he worked at Trans-Lux Sports in Logan, Utah as a production engineer. He was presented with the Outstanding Teaching Assistant Award from the College of Engineering at the University of Utah in 2005. He is also a member of Who's Who Among Students in American Colleges and Universities, and is a volunteer for the Boy Scouts of America. His current research interests include numerical methods in electromagnetics, broad band antenna design, and random design and analysis.

2006 INSTITUTIONAL MEMBERS

AUSTRALIAN DEFENCE LIBRARY
Northcott Drive
Campbell, A.C.T. 2600 AUSTRALIA

BEIJING BOOK COMPANY, INC
701 E Lindon Ave.
Linden, NJ 07036-2495

BRITISH LIBRARY
Boston SPA, Wetherby
West Yorkshire, UK LS23 7BQ

DARMSTADT U. OF TECHNOLOGY
Schlossgartenstrasse 8
Darmstadt, Hessen
GERMANY D-64289

DARTMOUTH COLL-FELDBERG LIB
6193 Murdough Center
Hanover, NH 03755-3560

DEFENCE RESEARCH ESTAB. LIB.
3701 Carling Avenue
Ottawa, ON, K1A 0Z4 CANADA

DLR-STANDORTBIBLIOTEK
Muenchnerstrasse 20
Wessling, Germany 82234

DPS/LIBRARY (EABV)
Alion Science & Technology
185 Admiral Cochrane Drive
Annapolis, MD 214017307

DSTO-DSTORL EDINBURGH
Jets AU/33851-99, PO Box 562
Milsons Point, NSW
AUSTRALIA 1565

DTIC-OCP/LIBRARY
8725 John J. Kingman Rd. Ste 0944
Ft. Belvoir, VA 22060-6218

ELLEDIEMME SRL
Via Baccina 30
Roma, Italy 00184

ELSEVIER
Bibliographic Databases
PO Box 2227
Amsterdam, Netherlands 1000 CE

ENGINEERING INFORMATION, INC
PO Box 543
Amsterdam, Netherlands 1000 Am

ETSE TELECOMUNICACION
Biblioteca, Campus Lagoas
Vigo, 36200 SPAIN

FGAN-FHR
Neuenahrerstrasse 20
Wachtberg, Germany 53343

FLORIDA INTERNATIONAL UNIV.
ECE Dept./EAS-3983
10555 W. Flagler St
Miami, FL 33174

GEORGIA TECH LIBRARY
225 North Avenue, NW
Atlanta, GA 30332-0001

HRL LABS, RESEARCH LIBRARY
3011 Malibu Canyon
Malibu, CA 90265

IEE INSPEC/Acquisitions Section
Michael Faraday House
6 Hills Way
Stevenage, Herts UK SG1 2AY

IND CANTABRIA
PO Box 830470
Birmingham, AL 35283

INSTITUTE FOR SCIENTIFIC INFO.
Publication Processing Dept.
3501 Market St.
Philadelphia, PA 19104-3302

LIBRARY of CONGRESS
Reg. Of Copyrights
Attn: 40T Deposits
Washington DC, 20559

LINDA HALL LIBRARY
5109 Cherry Street
Kansas City, MO 64110-2498

MISSISSIPPI STATE UNIV LIBRARY
PO Box 9570
Mississippi State, MS 39762

MIT LINCOLN LABORATORY
Periodicals Library
244 Wood Street
Lexington, MA 02420

NA KANSAI KINOKUNNA CO.
Attn: M. MIYOSHI
PO Box 36 (NDLA KANSAI)
Hongo, Tokyo, JAPAN 113-8688

NATL. CTR. FOR HIGH-
PERFORMANCE COMPUTING LIB.
PO Box 117-00930
Taipei City, Taiwan (ROC) 10699

NATL. GROUND INTELL. CENTER
2055 Boulders Road
Charlottesville, VA 22911-8318

NAVAL POSTGRADUATE SCHOOL
Attn:J. Rozdal/411 Dyer Rd./ Rm 111
Monterey, CA 93943-5101

NAVAL RESEARCH LABORATORY
C. Office, 4555 Overlook Avenue, SW
Washington, DC 20375

OHIO STATE UNIVERSITY
1320 Kinnear Road
Columbus, OH 43212

OVIEDO LIBRARY
PO BOX 830679
Birmingham, AL 35283

PAIKNAM ACAD. INFO CTR LIB.
Hanyang U/17 Haengdang-Dong
Seongdong-ki, Seoul, S Korea 133-
791

PENN STATE UNIVERSITY
126 Paterno Library
University Park, PA 16802-1808

PHILIPS RESEARCH LAB
Cross Oak Lane, Stella Cox, Salfords
Red Hill, UK RH1 5HA

RENTON TECH LIBRARY/BOEING
PO BOX 3707
SEATTLE, WA 98124-2207

SOUTHWEST RESEARCH INST.
6220 Culebra Road
San Antonio, TX 78238

SWEDISH DEFENCE RES.
AGENCY (FOI)
PO Box 1165
Linkoping, Sweden S-58111

SWETS INFORMATION SERVICES
160 Ninth Avenue, Suite A
Runnemed, NJ 08078

SYRACUSE UNIVERSITY
EECS, 121 Link Hall
Syracuse, NY 13244

TECHNISCHE UNIV. DELFT
Mekelweg 4, Delft, Holland, 2628 CD
NETHERLANDS

TIB & UNIV. BIB. HANNOVER
DE/5100/G1/0001
Welfengarten 1B
Hannover, GERMANY 30167

TOKYO KOKA UNIVERSITY
1404-1 Katakura-Cho
Hachioji, Tokyo, JAPAN 192-0914

UNIV OF CENTRAL FLORIDA LIB.
4000 Central Florida Boulevard
Orlando, FL 32816-8005

UNIV OF COLORADO LIBRARY
Campus Box 184
Boulder, CO 80309-0184

UNIVERSITY OF MISSISSIPPI
John Davis Williams Library
PO Box 1848
University, MS 38677-1848

UNIV OF MISSOURI-ROLLA LIB.
1870 Miner Circle
Rolla, MO 65409-0001

USAE ENG. RES. & DEV. CENTER
Attn: Library/Journals
72 Lyme Road
Hanover, NH 03755-1290

USP POLI
Av: Elmira Martins Moreira, 455
Jacarei, Sao Paulo, Brazil 12306-730

ACES COPYRIGHT FORM

This form is intended for original, previously unpublished manuscripts submitted to ACES periodicals and conference publications. The signed form, appropriately completed, MUST ACCOMPANY any paper in order to be published by ACES. PLEASE READ REVERSE SIDE OF THIS FORM FOR FURTHER DETAILS.

TITLE OF PAPER:

RETURN FORM TO:

Dr. Atef Z. Elsherbeni
University of Mississippi
Dept. of Electrical Engineering
Anderson Hall Box 13
University, MS 38677 USA

AUTHORS(S)

PUBLICATION TITLE/DATE:

PART A - COPYRIGHT TRANSFER FORM

(NOTE: Company or other forms may not be substituted for this form. U.S. Government employees whose work is not subject to copyright may so certify by signing Part B below. Authors whose work is subject to Crown Copyright may sign Part C overleaf).

The undersigned, desiring to publish the above paper in a publication of ACES, hereby transfer their copyrights in the above paper to The Applied Computational Electromagnetics Society (ACES). The undersigned hereby represents and warrants that the paper is original and that he/she is the author of the paper or otherwise has the power and authority to make and execute this assignment.

Returned Rights: In return for these rights, ACES hereby grants to the above authors, and the employers for whom the work was performed, royalty-free permission to:

1. Retain all proprietary rights other than copyright, such as patent rights.
2. Reuse all or portions of the above paper in other works.

3. Reproduce, or have reproduced, the above paper for the author's personal use or for internal company use provided that (a) the source and ACES copyright are indicated, (b) the copies are not used in a way that implies ACES endorsement of a product or service of an employer, and (c) the copies per se are not offered for sale.

4. Make limited distribution of all or portions of the above paper prior to publication.

5. In the case of work performed under U.S. Government contract, ACES grants the U.S. Government royalty-free permission to reproduce all or portions of the above paper, and to authorize others to do so, for U.S. Government purposes only.

ACES Obligations: In exercising its rights under copyright, ACES will make all reasonable efforts to act in the interests of the authors and employers as well as in its own interest. In particular, ACES REQUIRES that:

1. The consent of the first-named author be sought as a condition in granting re-publication permission to others.
2. The consent of the undersigned employer be obtained as a condition in granting permission to others to reuse all or portions of the paper for promotion or marketing purposes.

In the event the above paper is not accepted and published by ACES or is withdrawn by the author(s) before acceptance by ACES, this agreement becomes null and void.

AUTHORIZED SIGNATURE

TITLE (IF NOT AUTHOR)

EMPLOYER FOR WHOM WORK WAS PERFORMED

DATE FORM SIGNED

Part B - U.S. GOVERNMENT EMPLOYEE CERTIFICATION

(NOTE: if your work was performed under Government contract but you are not a Government employee, sign transfer form above and see item 5 under Returned Rights).

This certifies that all authors of the above paper are employees of the U.S. Government and performed this work as part of their employment and that the paper is therefor not subject to U.S. copyright protection.

AUTHORIZED SIGNATURE

TITLE (IF NOT AUTHOR)

NAME OF GOVERNMENT ORGANIZATION

DATE FORM SIGNED

PART C - CROWN COPYRIGHT

(NOTE: ACES recognizes and will honor Crown Copyright as it does U.S. Copyright. It is understood that, in asserting Crown Copyright, ACES in no way diminishes its rights as publisher. Sign only if ALL authors are subject to Crown Copyright).

This certifies that all authors of the above Paper are subject to Crown Copyright. (Appropriate documentation and instructions regarding form of Crown Copyright notice may be attached).

AUTHORIZED SIGNATURE

TITLE OF SIGNEE

NAME OF GOVERNMENT BRANCH

DATE FORM SIGNED

Information to Authors

ACES POLICY

ACES distributes its technical publications throughout the world, and it may be necessary to translate and abstract its publications, and articles contained therein, for inclusion in various compendiums and similar publications, etc. When an article is submitted for publication by ACES, acceptance of the article implies that ACES has the rights to do all of the things it normally does with such an article.

In connection with its publishing activities, it is the policy of ACES to own the copyrights in its technical publications, and to the contributions contained therein, in order to protect the interests of ACES, its authors and their employers, and at the same time to facilitate the appropriate re-use of this material by others.

The new United States copyright law requires that the transfer of copyrights in each contribution from the author to ACES be confirmed in writing. It is therefore necessary that you execute either Part A-Copyright Transfer Form or Part B-U.S. Government Employee Certification or Part C-Crown Copyright on this sheet and return it to the Managing Editor (or person who supplied this sheet) as promptly as possible.

CLEARANCE OF PAPERS

ACES must of necessity assume that materials presented at its meetings or submitted to its publications is properly available for general dissemination to the audiences these activities are organized to serve. It is the responsibility of the authors, not ACES, to determine whether disclosure of their material requires the prior consent of other parties and if so, to obtain it. Furthermore, ACES must assume that, if an author uses within his/her article previously published and/or copyrighted material that permission has been obtained for such use and that any required credit lines, copyright notices, etc. are duly noted.

AUTHOR/COMPANY RIGHTS

If you are employed and you prepared your paper as a part of your job, the rights to your paper initially rest with your employer. In that case, when you sign the copyright form, we assume you are authorized to do so by your employer and that your employer has consented to all of the terms and conditions of this form. If not, it should be signed by someone so authorized.

NOTE RE RETURNED RIGHTS: Just as ACES now requires a signed copyright transfer form in order to do "business as usual", it is the intent of this form to return rights to the author and employer so that they too may do "business as usual". If further clarification is required, please contact: The Managing Editor, R. W. Adler, Naval Postgraduate School, Code EC/AB, Monterey, CA, 93943, USA (831)656-2352.

Please note that, although authors are permitted to re-use all or portions of their ACES copyrighted material in other works, this does not include granting third party requests for reprinting, republishing, or other types of re-use.

JOINT AUTHORSHIP

For jointly authored papers, only one signature is required, but we assume all authors have been advised and have consented to the terms of this form.

U.S. GOVERNMENT EMPLOYEES

Authors who are U.S. Government employees are not required to sign the Copyright Transfer Form (Part A), but any co-authors outside the Government are.

Part B of the form is to be used instead of Part A only if all authors are U.S. Government employees and prepared the paper as part of their job.

NOTE RE GOVERNMENT CONTRACT WORK: Authors whose work was performed under a U.S. Government contract but who are not Government employees are required so sign Part A-Copyright Transfer Form. However, item 5 of the form returns reproduction rights to the U. S. Government when required, even though ACES copyright policy is in effect with respect to the reuse of material by the general public.

January 2002

INFORMATION FOR AUTHORS

PUBLICATION CRITERIA

Each paper is required to manifest some relation to applied computational electromagnetics. **Papers may address general issues in applied computational electromagnetics, or they may focus on specific applications, techniques, codes, or computational issues.** While the following list is not exhaustive, each paper will generally relate to at least one of these areas:

- 1. Code validation.** This is done using internal checks or experimental, analytical or other computational data. Measured data of potential utility to code validation efforts will also be considered for publication.
- 2. Code performance analysis.** This usually involves identification of numerical accuracy or other limitations, solution convergence, numerical and physical modeling error, and parameter tradeoffs. However, it is also permissible to address issues such as ease-of-use, set-up time, run time, special outputs, or other special features.
- 3. Computational studies of basic physics.** This involves using a code, algorithm, or computational technique to simulate reality in such a way that better, or new physical insight or understanding, is achieved.
- 4. New computational techniques,** or new applications for existing computational techniques or codes.
- 5. “Tricks of the trade”** in selecting and applying codes and techniques.
- 6. New codes, algorithms, code enhancement, and code fixes.** This category is self-explanatory, but includes significant changes to existing codes, such as applicability extensions, algorithm optimization, problem correction, limitation removal, or other performance improvement. **Note: Code (or algorithm) capability descriptions are not acceptable, unless they contain sufficient technical material to justify consideration.**
- 7. Code input/output issues.** This normally involves innovations in input (such as input geometry standardization, automatic mesh generation, or computer-aided design) or in output (whether it be tabular, graphical, statistical, Fourier-transformed, or otherwise signal-processed). Material dealing with input/output database management, output interpretation, or other input/output issues will also be considered for publication.
- 8. Computer hardware issues.** This is the category for analysis of hardware capabilities and limitations of various types of electromagnetics computational requirements. Vector and parallel computational techniques and implementation are of particular interest.

Applications of interest include, but are not limited to, antennas (and their electromagnetic environments), networks, static fields, radar cross section, shielding, radiation hazards, biological effects, electromagnetic pulse (EMP), electromagnetic interference (EMI), electromagnetic compatibility (EMC), power transmission, charge transport, dielectric, magnetic and nonlinear materials, microwave components, MEMS technology, MMIC technology, remote sensing and geometrical and physical optics, radar and communications systems, fiber optics, plasmas, particle accelerators, generators and motors, electromagnetic wave propagation, non-destructive evaluation, eddy currents, and inverse scattering.

Techniques of interest include frequency-domain and time-domain techniques, integral equation and differential equation techniques, diffraction theories, physical optics, moment methods, finite differences and finite element techniques, modal expansions, perturbation methods, and hybrid methods. This list is not exhaustive.

A unique feature of the Journal is the publication of unsuccessful efforts in applied computational electromagnetics. Publication of such material provides a means to discuss problem areas in electromagnetic modeling. Material representing an unsuccessful application or negative results in computational electromagnetics will be considered for publication only if a reasonable expectation of success (and a reasonable effort) are reflected. Moreover, such material must represent a problem area of potential interest to the ACES membership.

Where possible and appropriate, authors are required to provide statements of quantitative accuracy for measured and/or computed data. This issue is discussed in “Accuracy & Publication: Requiring, quantitative accuracy statements to accompany data,” by E. K. Miller, *ACES Newsletter*, Vol. 9, No. 3, pp. 23-29, 1994, ISBN 1056-9170.

EDITORIAL REVIEW

In order to ensure an appropriate level of quality control, papers are peer reviewed. They are reviewed both for technical correctness and for adherence to the listed guidelines regarding information content.

JOURNAL CAMERA-READY SUBMISSION DATES

March issue	deadline 8 January
July issue	deadline 20 May
November issue	deadline 20 September

Uploading an acceptable camera-ready article after the deadlines will result in a delay in publishing this article.

STYLE FOR CAMERA-READY COPY

The ACES Journal is flexible, within reason, in regard to style. However, certain requirements are in effect:

1. The paper title should NOT be placed on a separate page. The title, author(s), abstract, and (space permitting) beginning of the paper itself should all be on the first page. The title, author(s), and author affiliations should be centered (center-justified) on the first page.
2. An abstract is REQUIRED. The abstract should be a brief summary of the work described in the paper. It should state the computer codes, computational techniques, and applications discussed in the paper (as applicable) and should otherwise be usable by technical abstracting and indexing services.
3. Either British English or American English spellings may be used, provided that each word is spelled consistently throughout the paper.
4. Any commonly-accepted format for referencing is permitted, provided that internal consistency of format is maintained. As a guideline for authors who have no other preference, we recommend that references be given by author(s) name and year in the body of the paper (with alphabetical listing of all references at the end of the paper). Titles of Journals, monographs, and similar publications should be in italic font or should be underlined. Titles of papers or articles should be in quotation marks.
5. Internal consistency shall also be maintained for other elements of style, such as equation numbering. As a guideline for authors who have no other preference, we suggest that equation numbers be placed in parentheses at the right column margin.
6. The intent and meaning of all text must be clear. For authors who are NOT masters of the English language, the ACES Editorial Staff will provide assistance with grammar (subject to clarity of intent and meaning).
7. Unused space should be minimized. Sections and subsections should not normally begin on a new page.

PAPER FORMAT

The preferred format for initial submission and camera-ready manuscripts is 12 point Times Roman font, single line spacing and double column format, similar to that used here, with top, bottom, left, and right 1 inch margins. Manuscripts should be prepared on standard 8.5x11 inch paper.

Only camera-ready electronic files are accepted for publication. The term “**camera-ready**” means that the material is neat, legible, and reproducible. Full details can be found on ACES site, Journal section.

ACES reserves the right to edit any uploaded material, however, this is not generally done. It is the author(s)

responsibility to provide acceptable camera-ready pdf files. Incompatible or incomplete pdf files will not be processed, and authors will be requested to re-upload a revised acceptable version.

SUBMITTAL PROCEDURE

All submissions should be uploaded to ACES server through ACES web site (<http://aces.ee.olemiss.edu>) by using the upload button, journal section. Only pdf files are accepted for submission. The file size should not be larger than 5MB, otherwise permission from the Editor-in-Chief should be obtained first. The Editor-in-Chief will acknowledge the electronic submission after the upload process is successfully completed.

COPYRIGHTS AND RELEASES

Each primary author must sign a copyright form and obtain a release from his/her organization vesting the copyright with ACES. Copyright forms are available at ACES, web site (<http://aces.ee.olemiss.edu>). To shorten the review process time, the executed copyright form should be forwarded to the Editor-in-Chief immediately after the completion of the upload (electronic submission) process. Both the author and his/her organization are allowed to use the copyrighted material freely for their own private purposes.

Permission is granted to quote short passages and reproduce figures and tables from and ACES Journal issue provided the source is cited. Copies of ACES Journal articles may be made in accordance with usage permitted by Sections 107 or 108 of the U.S. Copyright Law. This consent does not extend to other kinds of copying, such as for general distribution, for advertising or promotional purposes, for creating new collective works, or for resale. The reproduction of multiple copies and the use of articles or extracts for commercial purposes require the consent of the author and specific permission from ACES. Institutional members are allowed to copy any ACES Journal issue for their internal distribution only.

PUBLICATION CHARGES

ACES members are allowed 12 printed pages per paper without charge; non-members are allowed 8 printed pages per paper without charge. Mandatory page charges of \$75 a page apply to all pages in excess of 12 for members or 8 for non-members. Voluntary page charges are requested for the free (12 or 8) pages, but are NOT mandatory or required for publication. A priority courtesy guideline, which favors members, applies to paper backlogs. Authors are entitled to 15 free reprints of their articles and must request these from the Managing Editor. Additional reprints are available to authors, and reprints available to non-authors, for a nominal fee.

ACES Journal is abstracted in INSPEC, in Engineering Index, and in DTIC.